USED FUEL DISPOSITION CAMPAIGN

Used Nuclear Fuel Loading and Structural Performance Under Normal Conditions of Transport – Supporting Material Properties and Modeling Inputs

Fuel Cycle Research & Development

Prepared for

U.S. Department of Energy

Used Fuel Disposition Campaign

March 16, 2013

FCRD-UFD-2013-000123

Disclaimer

This information was prepared as an account of work sponsored by an agency of the U.S. Government. Neither the U.S. Government nor any agency thereof, nor any of their employees, makes any warranty, expressed or implied, or assumes any legal liability or responsibility for the accuracy, completeness, or usefulness, of any information, apparatus, product, or process disclosed or represents that its use would not infringe privately owned rights. References herein to any specific commercial product, process, or service by trade name, trade mark, manufacturer, or otherwise, does not necessarily constitute or imply its endorsement, recommendation, or favoring by the U.S. Government or any agency thereof. The views and opinions of the authors expressed herein do not necessarily state or reflect those of the U.S. Government or any agency thereof.

EXECUTIVE SUMMARY

This document contains a compilation of structural material properties for each of the materials necessary to support modeling and simulation initiatives identified in *Used Nuclear Fuel Loading and Structural Performance Under Normal Conditions of Transport - Draft Modeling, Simulation and Experimental Integration RD&D Plan (Adkins 2013).* This compilation effort is focused on using existing models for properties rather than developing new property models because of the limited funding and schedule. This document contains the relevant material properties necessary to model and simulate the transportation of a generic transport package containing 32 pressurized water reactor 17x17 fuel assemblies under normal conditions of transport (NCT). These material properties represent the current best-estimate values for the properties in question and should be used for the initial modeling of the scenarios related to the NCT as well as for the separate shaker table tests performed on a surrogate assembly as outlined in the RD&D Plan. The conditions experienced by the fuel assemblies in-reactor are very challenging and the combination of fuel burnup, damage from fast neutron flux, and long service operation under high temperature (280°C-350°C for cladding and assembly hardware) and high internal fuel rod and external pressure (15.5 MPa) water, leads to large changes in the material properties of the fuel, cladding, and other assembly components.

The material properties correlations included in this document represent a best-estimate fit to unirradiated and irradiated data. The cladding properties in particular have been successfully used in the Pacific Northwest National Laboratory/U.S. Nuclear Regulatory Commission fuel performance codes, FRAPCON-3 (Geelhood et al. 2010a) and FRAPTRAN (Geelhood et al. 2010b) to model in-reactor behavior and transient performance, respectively.

It is acknowledged that there is variation in the data, particularly from irradiated sample data. Additionally, it is not fully known what the impact of long-term storage at 100°C-400°C is on these materials. In order to address these uncertainties, standard deviations and uncertainty distributions are included with the appropriate material properties models. Also, an attempt is made to quantify the potential impact of long-term storage on these properties.

This material properties document consists of the following sections:

- Spent fuel conditions
- Cladding properties
- Fuel properties
- Grid properties
- Cask material properties
- Material properties for a surrogate shaker table assembly

The largest uncertainty exists on the material properties for the irradiated components, particularly the fuel and the cladding. Best-estimate models for the fuel and the cladding that have been provided have been successfully used as part of the Pacific Northwest National Laboratory/U.S. Nuclear Regulatory Commission fuel performance codes. Areas of particular uncertainty have been identified, and these areas will be targeted for sensitivity studies in order to determine if these large uncertainties have significant impact on the response of the fuel rod, and generic cask, canister, and basket components under NCT. If any area is found to have significant impact during application, it will identify a need for further testing. However, in the meantime, these properties are expected to give reasonable value to the modelers for their initial modeling activities in support of the RD&D Plan.

ACKNOWLEDGMENTS

The authors, Ken Geelhood and Carl Beyer (Pacific Northwest National Laboratory), would like to thank Harold Adkins and Brian Koeppel (Pacific Northwest National Laboratory) for their significant contributions to this report.

The authors would also like to thank Colleen Winters, Cornelia Brim, Steven Matsumoto, and Susan Tackett, Pacific Northwest National Laboratory technical communications specialists, for editing assistance.

CONTENTS

1. INTRODUCTION 1
  1.1 Purpose and Scope 1
  1.2 Report Contents and Organization 2

2. SPENT FUEL CONDITIONS 5
  2.1 Burnup 7
  2.2 Fast Neutron Fluence 7
  2.3 Corrosion and Hydriding 8
    2.3.1 Corrosion 8
    2.3.2 Metal Consumed 9
    2.3.3 Hydride Formation 10
    2.3.4 Excess Hydrogen 11
  2.4 Level of In-Reactor Wear and Fretting 13
  2.5 Example Values 14

3. CLADDING PROPERTIES 19
  3.1 Elastic Modulus 20
    3.1.1 Model 21
    3.1.2 Data Comparison 22
    3.1.3 Uncertainty 23
  3.2 Yield Stress 25
    3.2.1 Strength Coefficient, K 25
    3.2.2 Strain Hardening Exponent, n 26
    3.2.3 Strain Rate Exponent, m 26
    3.2.4 Data Comparison 27
    3.2.5 Uncertainty 29
  3.3 Ultimate Tensile Strength 31
    3.3.1 Model 31
    3.3.2 Data Comparison 31
    3.3.3 Uncertainty 33
  3.4 Uniform Elongation and Total Elongation 36
    3.4.1 Model 36
    3.4.2 Data Comparison 38
    3.4.3 Uncertainty 39
  3.5 Fracture Toughness 40
    3.5.1 Model 41
    3.5.2 Data Comparison 41
    3.5.3 Uncertainty 42
  3.6 Fatigue 43

4. FUEL PROPERTIES 45
  4.1 Elastic Modulus 45
    4.1.1 Model 45

4.1.2 Data Comparison 46
4.1.3 Uncertainty 48
4.2 Fracture Strength 49
4.2.1 Model 49
4.2.2 Data Comparison 50
4.2.3 Uncertainty 51
4.3 Fuel/Clad Bonding Layer 51
4.3.1 Boiling Water Reactors 52
4.3.2 Pressurized Water Reactors 53
4.3.3 Summary 55

5. **GRID MATERIAL PROPERTIES** 57
5.1 Zircaloy Grids 58
5.2 Inconel 718 Grids 60
5.2.1 Elastic and Bulk Moduli 60
5.2.2 Yield Stress 61
5.2.3 Ultimate Tensile Strength 62
5.2.4 Total Elongation 63
5.2.5 Density 64

6. **STORAGE AND TRANSPORT COMPONENT MATERIAL PROPERTIES** 65
6.1 Baseline Package 65
6.2 Elastic Modulus 66
6.2.1 304 Stainless Steel 66
6.2.2 316 Stainless Steel 67
6.2.3 XM-19 69
6.2.4 Boral™ and Aluminum 1100 71
6.3 Yield Stress 72
6.3.1 304 Stainless 72
6.3.2 316 Stainless 73
6.3.3 XM-19 74
6.3.4 Boral™ and Aluminum 1100 75
6.4 Ultimate Tensile Stress 76
6.4.1 304 Stainless Steel 76
6.4.2 316 Stainless Steel 77
6.4.3 XM-19 78
6.4.4 Boral™ and Aluminum 1100 79
6.5 Total Elongation 80
6.5.1 304 Stainless Steel 80
6.5.2 316 Stainless Steel 81
6.5.3 XM-19 82
6.6 Density 83
6.6.1 304 Stainless Steel 83
6.6.2 316 Stainless Steel 83
6.6.3 XM-19 84
6.6.4 Boral™ and Aluminum 1100 84

7. **SURROGATE ASSEMBLY MATERIAL PROPERTIES** 85

8. **CONCLUSIONS** 87

9. **REFERENCES** 89

FIGURES

Figure 2.1. Reference Fuel Assembly for This Study (Westinghouse 17x17 type fuel assembly) 5
Figure 2.2. General Trend in Corrosion Thickness for Zircaloy-4 and ZIRLO™ under PWR Conditions vs. Burnup (Kesterson et al. 2006.) 9
Figure 2.3. Typical Morphology of Hydrides in PWR CWSRA Cladding (Nagase 2011) 11
Figure 3.1. Zircaloy-4 Cladding Tubes 19
Figure 3.2. Sample True Stress vs. True Strain Curve Using New Model 20
Figure 3.3. Predicted vs. Measured Elastic Modulus for Unirradiated Data 23
Figure 3.4. Distribution of Uncertainty for Elastic Modulus for Unirradiated Data 24
Figure 3.5. Predicted vs. Measured Yield Stress for Irradiated and Unirradiated Data 27
Figure 3.6. Predicted vs. Measured Yield Stress for Irradiated Data 28
Figure 3.7. Predicted Minus Measured Yield Stress Data vs. Fast Fluence for Irradiated and Unirradiated Data 28
Figure 3.8. Distribution on Uncertainty for Yield Stress for Unirradiated and Irradiated Data 29
Figure 3.9. Distribution on Uncertainty for Yield Stress for Unirradiated Data 30
Figure 3.10. Distribution on Uncertainty for Yield Stress for Irradiated Data 30
Figure 3.11. Change in Yield Stress with Increasing Fast Neutron Fluence at 315°C 31
Figure 3.12. Predicted vs. Measured Ultimate Tensile Strength for Irradiated and Unirradiated Data 32
Figure 3.13. Predicted Minus Measured Ultimate Tensile Strength Data vs. Fast Fluence for Irradiated and Unirradiated Data 33
Figure 3.14. Distribution on Uncertainty for Ultimate Tensile Strength for Unirradiated and Irradiated Data 34
Figure 3.15. Distribution on Uncertainty for Ultimate Tensile Strength for Unirradiated Data 34
Figure 3.16. Predicted Minus Measured Ultimate Tensile Strength Data vs. Fast Fluence for Irradiated Data 35
Figure 3.17. Change in Ultimate Tensile Strength with Increasing Fast Neutron Fluence at 315°C 36
Figure 3.18. Hydrogen Concentration vs. Fast Neutron Fluence for the Data in the PNNL Database (293K≤T≤755K) 38
Figure 3.19. Predicted Minus Measured Uniform Elongation vs. Excess Hydrogen for Irradiated Data 39
Figure 3.20. Distribution on Uncertainty for Uniform Elongation for Irradiated Data 40
Figure 3.21. Predicted vs. Measured Fracture Toughness Data 42
Figure 3.22. Distribution on Uncertainty for Fracture Toughness Data 42
Figure 3.23. O'Donnell Fatigue-Design Curve for Irradiated Zircaloy from Room Temperature to 600°F (316°C) 43
Figure 4.1. UO_2 Fuel Pellets 45
Figure 4.2. Predicted vs. Measured Elastic Modulus for Unirradiated Data 46
Figure 4.3. Predicted vs. Measured Elastic Modulus for SimFuel and Irradiated Data 47

Figure 4.4. Predicted vs. Measured Elastic Modulus for Unirradiated, SimFuel, and Irradiated Data 48
Figure 4.5. Distribution on Uncertainty for Elastic Modulus for Unirradiated Fuel Data.......... 49
Figure 4.6. Distribution on Uncertainty for Elastic Modulus for Irradiated Data 49
Figure 4.7. Fracture Strength Model in MATPRO and Data Used in Model Development 50
Figure 4.8. Micrograph Taken from Kim 2010 of Fuel-Cladding Bond Region at Mid-axial Position in a PWR Fuel Rod at 53 GWd/MTU Burnup.......... 52
Figure 4.9. Relationship between Extent of Fuel-Cladding Bonding Layer and Rod Power and Burnup for a BWR Fuel Rod (Taken from Nogita and Une 1997) 53
Figure 5.1. Assembly Grid Spacers 57
Figure 5.2. Typical Grid with Springs and Dimples to Retain the Fuel Rods 58
Figure 5.3. Corrosion Thickness in ZIRLO Grid Straps and Guide Tubes at Different Axial Locations in an Assembly with Approximately 54 GWd/MTU Average Burnup.......... 59
Figure 5.4. Hydrogen Concentrations in ZIRLO Grid Straps and Guide Tubes at Different Axial Locations in an Assembly with Approximately 54 GWd/MTU Average Burnup 60
Figure 5.5. Elastic and Bulk Moduli for Inconel 718 61
Figure 5.6. Yield Stress for Inconel 718 Sheet That Has Been Cold Rolled and Cold Rolled and Annealed.......... 62
Figure 5.7. Ultimate Tensile Strength for Inconel 718 Sheet That Has Been Cold Rolled and Cold Rolled and Annealed 63
Figure 5.8. Total Elongation for Inconel 718 64
Figure 6.1. Baseline Package for Analysis is the HOLTEC Dual-Purpose MPC-32 Canister 65
Figure 6.2. Elastic Modulus for 304 Stainless Steel 67
Figure 6.3. Poisson’s Ratio for 304 Stainless Steel 67
Figure 6.4. Elastic Modulus for 316 Stainless Steel 68
Figure 6.5. Poisson’s Ratio for 316 Stainless Steel 69
Figure 6.6. Elastic Modulus for XM-19 Stainless Steel 70
Figure 6.7. Poisson’s Ratio for XM-19 Stainless Steel 71
Figure 6.8. Elastic Modulus for Aluminum 1100 72
Figure 6.9. Yield Stress for 304 Stainless Steel.......... 73
Figure 6.10. Yield Stress for 316 Stainless Steel.......... 74
Figure 6.11. Yield Stress for XM-19 Stainless Steel 75
Figure 6.12. Yield Stress for Aluminum 1100.......... 76
Figure 6.13. Ultimate Tensile Strength for 304 Stainless Steel 77
Figure 6.14. Ultimate Tensile Strength for 316 Stainless Steel 78
Figure 6.15. Ultimate Tensile Strength for XM-19 Stainless Steel 79
Figure 6.16. Ultimate Tensile Strength for Aluminum 1100.......... 80
Figure 6.17. Total Elongation for 304 Stainless Steel 81
Figure 6.18. Total Elongation for 316 Stainless Steel 82
Figure 6.19. Total Elongation for XM-19 Stainless Steel 83
Figure 7.1. Lead Rod within Copper Tube for Surrogate Assembly 85

TABLES

Table 2.1. PWR 17x17 Fuel Assembly Parameters 6
Table 2.2. PWR 17x17 Fuel Assembly Materials 6
Table 2.3. PWR 17x17 Fuel Rod Materials 6
Table 2.4. Properties Provided for Cladding 10
Table 2.5. Typical Conditions for Peak Fuel Rod from PWR Westinghouse 17x17 Fuel Assembly Discharged at Assembly Average Burnup of 30 GWd/MTU. 15
Table 2.6. Typical Conditions for Peak Fuel Rod from PWR Westinghouse 17x17 Fuel Assembly Discharged at Assembly Average Burnup of 40 GWd/MTU. 16
Table 2.7. Typical Conditions for Peak Fuel Rod from PWR Westinghouse 17x17 Fuel Assembly Discharged at Assembly Average Burnup of 50 GWd/MTU. 17
Table 2.8. Typical Conditions for Peak Fuel Rod from PWR Westinghouse 17x17 Fuel Assembly Discharged at Assembly Average Burnup of 55 GWd/MTU. 18
Table 7.1. Room Temperature Material Properties for Alloy 12200 Copper Tubing and Lead Bar Stock used for the Surrogate Fuel Assembly 85

ACRONYMS

BWR	boiling water reactor
CWSRA	cold worked stress relief annealed
DBTT	ductile-to-brittle-transition temperature
DOE	U.S. Department of Energy
DPA	displacements per atom
E	Elastic Modulus
GBC	generic burnup cask
GTRF	grid-to-rod fretting
GWd	gigawatt-day
IFM	intermediate flow mixing
K	strength coefficient
m	strain rate exponent
MPU	multipurpose canister
MTU	metric tons (Tonnes) of uranium
n	strain hardening exponent
NCT	normal conditions of transportation
NRC	U.S. Nuclear Regulatory Commission
ORNL	Oak Ridge National Laboratory
PCMI	pellet cladding mechanical interaction
PNNL	Pacific Northwest National Laboratory
PWR	pressurized water reactor
ρ	density
RXA	recrystallized annealed
TE	total elongation
UE	uniform elongation
UNF	used nuclear fuel
UTS	ultimate tensile strength
YS	yield stress

USED FUEL DISPOSITION CAMPAIGN
Used Nuclear Fuel Loading and Structural Performance Under Normal Conditions of Transport – Supporting Material Properties and Modeling Inputs

1. INTRODUCTION

A literature review, as part of execution of *Used Nuclear Fuel Loading and Structural Performance Under Normal Conditions of Transport - Draft Modeling, Simulation and Experimental Integration RD&D Plan (Adkins 2013)*, has been performed to identify material properties relevant to moderate- to high-burnup used nuclear fuel, as well as associated storage and transport components, to establish a credible database to feed into modeling and simulation tools for determining the specific mechanical performance characteristics for cladding and fuel assembly. Because of the limited funding and schedule, this effort has concentrated on using existing models for properties rather than developing new property models. Applicable data and information as well as inputs yielded in support of the RD&D Plan have been documented in this report. Also, specific recommendations based on the available information have been documented, and guidance regarding implementation in future modeling and simulation evaluation work performed under this, as well as possible future programs, have been provided. Data gaps in supporting information and boundary conditions that may exist have been identified. In order to determine the importance of these data gaps and properties with large uncertainty sensitivity, analyses will be performed. These analyses will determine if the gaps and uncertainties are important to the outcome of the assembly response to normal conditions of transportation (NCT). This will significantly reduce the amount of funding required.

1.1 Purpose and Scope

The primary focus of the material properties in this document is on pressurized water reactor (PWR) 17×17 type of fuel configuration for reasons identified in the RD&D Plan (Adkins 2013). The assembly average burnup values of the spent fuel considered range from 30 to 58 GWd/MTU. The properties are applicable to fuel and fuel cladding as well as degraded fuel assembly components such as spacer grids, intermediate fluid mixers, and control components. Material properties should span the range from room temperature to 400°C.

Understanding performance characteristics of used nuclear fuel (UNF) under loadings stemming from drying, storage, transfer, and NCT and establishing cumulative effects are viewed to be critical to maintaining safety bases and determining fuel condition for retrievability purposes. However, the integration of supporting information and all possible loading influences is viewed to be somewhat optimistic given the period of performance allocated for execution of the RD&D Plan. As such, limited work will be performed for the collection of information pertaining to any configurations other than transport, and an initial fuel material condition/state will be assumed, based on the best information available to date.

1.2 Report Contents and Organization

Section 2 describes the condition of the spent fuel. This section includes a description of the reference fuel assembly, discussion on fuel and cladding condition terms such as fuel burnup, cladding fast neutron fluence, cladding corrosion and hydriding, and the level of expected wear and fretting. To assist modelers in defining the initial conditions of fuel rods that have been discharged at various burnups, this section also includes tables of typical values of condition for rods at various burnup levels that have been produced. The expected axial variation in these parameters is shown at one-foot intervals. These parameters, along with the specific component temperatures will be used as inputs to the material property models given in the document.

Section 3 describes the cladding properties that will be necessary for modeling the fuel assemblies. Most of these models come from FRAPCON-3 (Geelhood et al. 2010a) or MATPRO (Siefken et al. 2001). Comparisons of model predictions to data are provided for both irradiated and unirradiated data. As appropriate, the calculated uncertainty and the distribution on that uncertainty are provided. Discussion on the applicability of these models to conditions following more than 20 years in dry cask storage will also be discussed. A fatigue-based failure curve is presented in this section as the most promising failure mechanism for fuel rods under NCT. The data used to develop this curve are not completely prototypic of those expected of spent fuel rods following more than 20 years in dry cask storage. For example, the stress state of the fatigue data and hydrogen level/distribution used to develop the fatigue curve are different from high-burnup used fuel during normal transportation. As initial stress intensities and expected stress cycles are calculated from the modeling task, this fatigue curve may be used to assess the potential for failure. If this curve shows operation far below the failure limit then that will provide adequate demonstration that the rods will not fail. If the modeling results show operation near this failure curve then further experimental work should be performed to produce a more prototypic failure curve.

Section 4 describes the fuel properties that will be necessary for modeling the fuel assemblies. Most of these models come from MATPRO as FRAPCON and FRAPTRAN (Geelhood et al. 2010b) do not consider the impact of the strength of the pellet because it is much greater than that of the cladding. Comparisons of model predictions to data are provided for both irradiated and unirradiated data. As appropriate, the calculated uncertainty and the distribution on that uncertainty are provided.

Section 5 provides the material properties for grid spacers, which are made of Zircaloy-4 or Inconel-718. This section includes discussion on how the Zircaloy-4 cladding properties may be used for Zircaloy-4 grids. The microstructure and texture of drawn tubes is very similar to that of cold rolled sheet. Typically the properties of these are assumed to be the same. For example, the expected fast neutron fluence, corrosion thickness, and hydrogen content for Zircaloy-4 grids will be given. For Inconel-718, the basic mechanical properties as a function of temperature will be provided for unirradiated sheet. The properties of Inconel-718 will likely change with irradiation, but no data are currently available for irradiated Inconel-718.

Section 6 provides the material properties for the generic basket and canister (GBC). This GBC holds 32 assemblies and has been selected as the reference canister for this study. It is assumed that the basket, basket support structures, and the multi-purpose canister (MPC) shell are all made of high-tensile XM-19 stainless steel. Many canisters have neutron poison plates consisting of aluminum alloy, Al-1100 and Boral™. This section provides properties for these materials as a function of temperature.

Section 7 provides material properties for materials that will be used in a surrogate assembly. Plans are under way to assemble a surrogate fuel assembly, replacing the Zircaloy-4 cladding tubes with copper tubing (Alloy 12200) and replacing the UO_2 fuel with lead bar stock. This surrogate assembly will be instrumented with accelerometers and tested under simulated NCT on a shaker table. Modeling will be performed to provide some validation of the modeling approach by comparing the results to the data from the instrumented surrogate assembly. To assist in this modeling activity, properties for all these materials are given.

Section 8 provides general conclusions from this report, and references are provided in Section 9.

2. SPENT FUEL CONDITIONS

The spent fuel assembly that will be considered for the first analysis is a 17x17 PWR assembly for a Westinghouse reactor. A picture of this assembly is shown in Figure 2.1 (Enusa 2013). This assembly is made of many components which are described in Table 2.1, Table 2.2, and Table 2.3.

Advanced cladding alloys, M5™, ZIRLO™, and Optimized ZIRLO™ are in use in most PWRs in the United States. However, this analysis will focus on the assemblies with Zircaloy-4 cold-work stress-relief anneal (CWSRA) cladding as it represents a majority of those assemblies currently in dry cask storage.

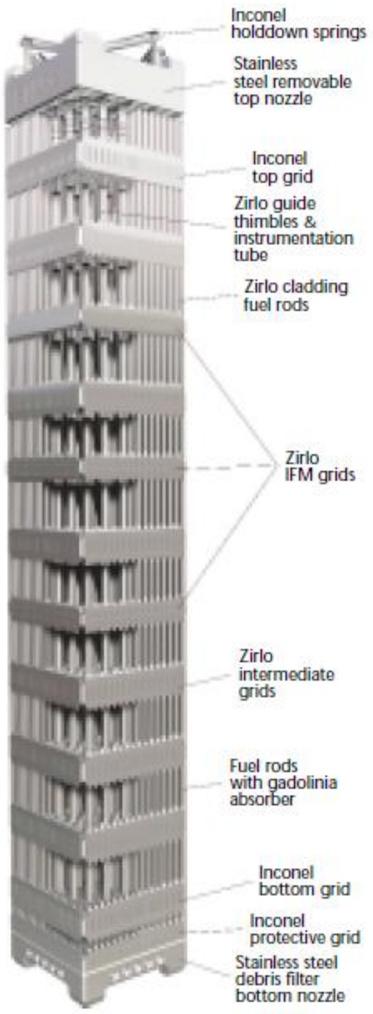
Inconel holddown springs
Stainless steel removable top nozzle
Inconel top grid
Zirlo guide thimbles & instrumentation tube
Zirlo cladding fuel rods
Zirlo IFM grids
Zirlo intermediate grids
Fuel rods with gadolinia absorber
Inconel bottom grid
Inconel protective grid
Stainless steel debris filter bottom nozzle

Figure 2.1. Reference Fuel Assembly for This Study (Westinghouse 17x17 type fuel assembly)

Table 2.1. PWR 17x17 Fuel Assembly Parameters

Array	17x17
Number of fuel rods	264
Number of guide rods	24
Number of instrumentation tubes	1
Number of grids (without IFM)	9
Number of IFM grids	3

IFM = intermediate flow mixing

Table 2.2. PWR 17x17 Fuel Assembly Materials

End Grids	Inconel-718
Intermediate grids	Zircaloy-4 or Inconel-718
IFM grid	Zircaloy-4
Protective grid (band and projections)	Inconel-718
Upper nozzle	Stainless Steel
Lower nozzle	Stainless Steel
Spring	Inconel-718
Thimble tube	Zircaloy-4
Instrumentation tube	Zircaloy-4

IFM = intermediate flow mixing

Table 2.3. PWR 17x17 Fuel Rod Materials

Pellet composition	UO_2
Neutron poison pellet composition	UO_2-Gd_2O_3
Cladding material	Zircaloy-4
Spring material	Stainless Steel
Plug material	Zircaloy-4

2.1 Burnup

Burnup is a convenient unit of the time that fuel has been in the reactor and the power level to which it has been exposed. Burnup is the integral of the fuel power as a function of time.

Burnup is presented in several different units. The most common is GWd/MTU. Other units are atom% burnup, which is the percent of uranium atoms that have fissioned and fissions/cm^3. The burnup units and their conversions are shown below.

GWd/MTU x 1 → MWd/kgU

GWd/MTU x 1000 → MWd/MTU

GWd/MTU x 0.88 → GWd/MTUO2

GWd/MTU x 0.1066 → atom% burnup

GWd/MTU x(ρ g/cm^3) x 2.747x1013 → fissions/cm^3

Different quantities are considered when discussing fuel burnup. The first is assembly average burnup, which is the average burnup of all the rods in a given fuel assembly. However, the burnup in each rod in an assembly is not the same for all rods. When individual rods are examined, the rod-average burnup is considered. Typically the ratio between the rod-average burnup for the peak rod in an assembly and the assembly average burnup is between 1.05 and 1.09. Within any given fuel rod, the burnup is not constant axially, but rather has some variation. When individual pellets are examined, the pellet burnup is considered. Typically the ratio between the peak pellet burnup and the rod-average burnup is 1.07 to 1.13. This ratio is higher at beginning of life and reduces through life in an attempt to burn the fuel rods as uniformly as possible.

2.2 Fast Neutron Fluence

When discussing the cladding, it is possible to use burnup of the fuel near the cladding as a metric for exposure; however, this is not a particularly precise metric of cladding exposure. In zirconium alloy cladding, fast neutrons damage the metal matrix. Fast neutrons are typically those with energy greater than 1 MeV, although some consider those neutrons greater than 0.1 MeV to be fast neutrons. The fast neutron flux is proportional to the fuel rod power, and therefore the fast neutron fluence (total number of fast neutrons to pass through a given area) is proportional to the burnup.

For a PWR with 17x17 fuel, the ratio between fast neutron flux and burnup is 1 GWd/MTU =$1.67\text{x}10^{24}$ n/m^2.

Typically, fast neutron flux is reported in units of n/m^2/s or n/cm^2/s, where 1 n/cm^2/s = 104 n/m^2/s and fast neutron fluence is reported in units of n/m^2 or n/cm^2, where 1 n/cm^2 = 104 n/m^2. Damage from fast neutrons may also be reported in terms of displacements per atom (DPA). The conversion between fast neutron fluence and DPA is dependent both on the material being irradiated and the neutron spectrum. For zirconium under PWR conditions, the ratio between DPA and fast neutron flux is 1 DPA = 4.5 x 1024 n/m^2 (Adamson and Cox 2005.)

2.3 Corrosion and Hydriding

As irradiation progresses in a PWR, the zirconium in the cladding slowly reacts with the water to form zirconium oxide according to the following equation.

$$Zr + 2H_2O \rightarrow ZrO_2 + 2H_2$$

The formation of this oxide is relatively slow, on the order of 10-15 μm per year, however, the oxide layer that builds up on the cladding affects the fuel rods in two ways. The first is that the fuel will operate at a slightly higher temperature because the zirconium oxide insulates the fuel more than the original zirconium. The second is that the metal in the cladding will thin as it is consumed by the oxide. Because the oxide layer offers very little strength, the cladding tubes are effectively thinned, which increases the stress within the cladding.

The equation above shows that hydrogen will be released from the reaction of zirconium with water. Much of this hydrogen is dissolved in the reactor coolant that maintains a hydrogen overpressure. However, some fraction of the released hydrogen is absorbed into the zirconium alloy cladding. For PWR applications, this absorbed fraction has been observed to be a constant value. By using this constant value it is possible to predict the amount of hydrogen in a cladding sample with a known oxide thickness.

Hydrogen affects cladding performance in that for high enough hydrogen concentrations, brittle zirconium hydride platelets will precipitate out in the cladding. These brittle hydrides reduce the ductility of the overall cladding tube and can provide easy paths for crack propagation.

2.3.1 Corrosion

The rate of in-reactor corrosion of zirconium is controlled by the water temperature and the heat flux across the cladding. Because of this, the corrosion layer thickness on a specific area of fuel cladding is dependent on both the axial elevation (water temperature increases with increasing height in the core) and the rod power history.

General trends in Zircloy-4 and ZIRLO™ oxide thickness with burnup can be seen in Figure 2.2. However, a fuel performance code, such a FRAPCON-3.4 is best suited for predicting the corrosion layer thickness for a specific rod as a function of burnup. Some corrosion thickness predictions are shown later in Section 2.5 for a sample PWR 17x17 rod.

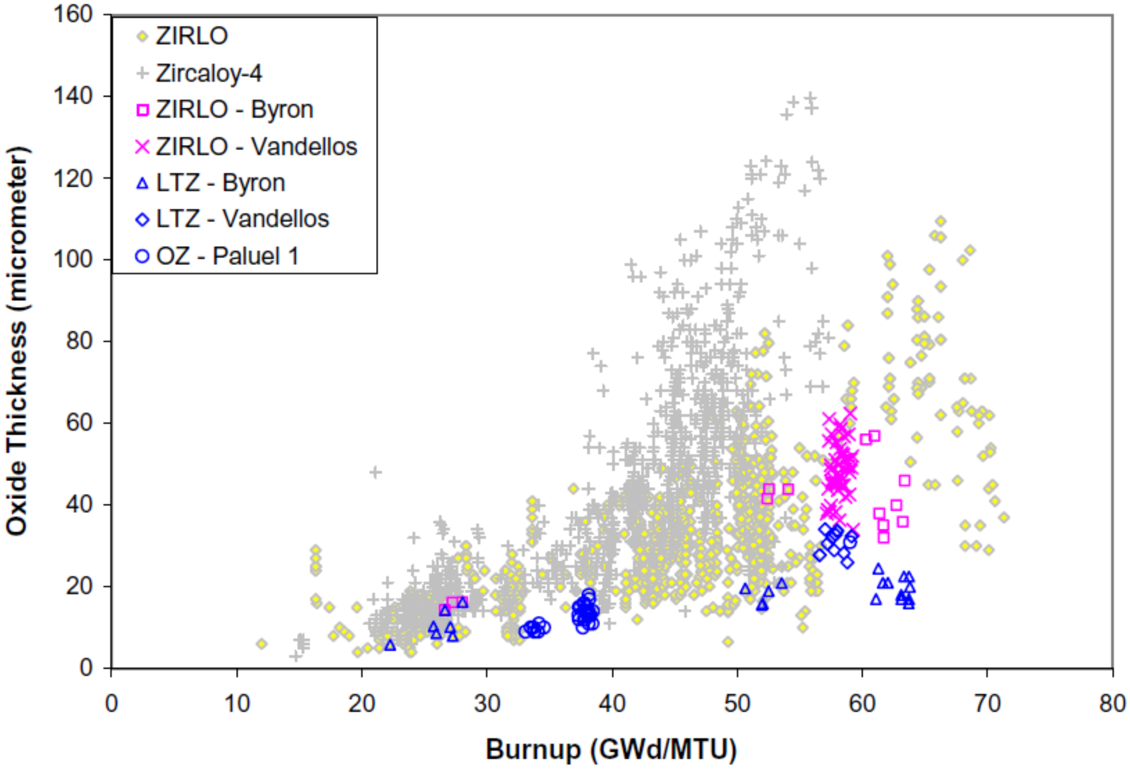

Figure 2.2. General Trend in Corrosion Thickness for Zircaloy-4 and ZIRLO™ under PWR Conditions vs. Burnup (Kesterson et al. 2006.)

The classic zirconium-based PWR fuel cladding is Zircaloy-4 CWSRA. However, in the past 10-15 years advanced alloys have been introduced by the fuel vendors. The main reason for the cladding alloy development has been to reduce the corrosion reaction with water relative to Zircaloy-4. The new alloys that have been introduced in the United States are ZIRLO™, Optimized ZIRLO™, and M5™. All of these alloys have lower corrosion rates than Zircaloy-4 at equivalent operating conditions.

2.3.2 Metal Consumed

The density of zirconium oxide is lower than the density of zirconium. Because of this, the thickness of the oxide layer will be greater than the thickness of metal consumed. The Pilling-Bedworth ratio is the ratio of the oxide thickness to the thickness of metal that was consumed. For zirconium alloy cladding, the Pilling-Bedworth ratio is 1.56. This means that in a stress calculation for cladding tubes, the thickness of the cladding used should be calculate according to the following equation.

$$t_{eff} = t_{nom} - \frac{\delta}{1.56}$$

where:

t_{eff} = effective cladding thickness (m)

t_{nom}= nominal cladding thickness (m)

δ = oxide layer thickness (m)

The oxide layer is quite brittle and may contain cracks and therefore should not be assumed to bear any load under stress conditions.

2.3.3 Hydride Formation

The metal-water reaction described in Section 2.3 results in free hydrogen. For PWR applications, it has been observed that a constant fraction of this free hydrogen is picked up by the cladding. Table 2.4 shows the most recent calculation of hydrogen pickup fractions for U.S. PWR cladding alloys (Geelhood and Beyer 2011). Also shown is the expected standard deviation in predicted hydrogen content that is expected based on these pickup fractions. It is recommended that the relative error in percent deviation be used for uncertainty analyses. Recent data (Billone et al. 2013, Billone et al. 2012) show that there is a 95-ppm axial variation in the level of circumferentially averaged hydrogen found in high burnup ZIRLO™ and Zircaloy-4 cladding over a 76-mm length. This observation fits well with the calculated uncertainties shown in Table 2.4.

Table 2.4. Properties Provided for Cladding

Alloy	Pickup Fraction	Standard Deviation
Zircaloy-4	15.3%	94 ppm / 23%
ZIRLO™	17.3%	110 ppm / 23%
M5™	10%	23 ppm / 29%

The recent data also showed a large circumferential variation of hydrogen within each ring. Measurement taken from quarter-sections of the individual rings (Billone et al. 2013, Billone et al. 2012) showed circumferential variation in hydrogen content with standard error of 35 to 310 wppm (approximately 6% to 36% relative standard error) relative to the mean values between 518 to 720 wppm for ZIRLO™ and 122-189 wppm (approximately 30% relative standard error) relative to mean values of 533 to 701 wppm for Zircaloy-4. Although these circumferential variations are large and are greater than the expected variation of the ring average hydrogen content, these variations are implicitly included in the models that use hydrogen as an input because only hydrogen measurements from full rings were used in the model development. It is expected that these full rings used in model development had similar circumferential variation.

2.3.4 Excess Hydrogen

Zirconium has a low solubility for hydrogen within the matrix. Therefore, as more hydrogen comes into the cladding and the level exceeds the solubility level, hydrogen begins to precipitate out of the matrix as zirconium hydride. These hydrides are quite brittle and can reduce the ductility of the overall cladding tube and provide easy paths for crack propagation.

The final heat treatment of Zircaloy-4 and ZIRLO™ is a CWSRA that leaves the cladding in the cold worked condition. Because of the grain structure and texture in a CWSRA cladding tube, the zirconium hydride precipitates out primarily in the circumferential direction. Additionally, because of the in-reactor temperature gradient, they also precipitate on the outer diameter of the cladding leading to the formation of a dense hydride rim. Figure 2.3 shows the typical morphology of hydrides in PWR CWSRA cladding.

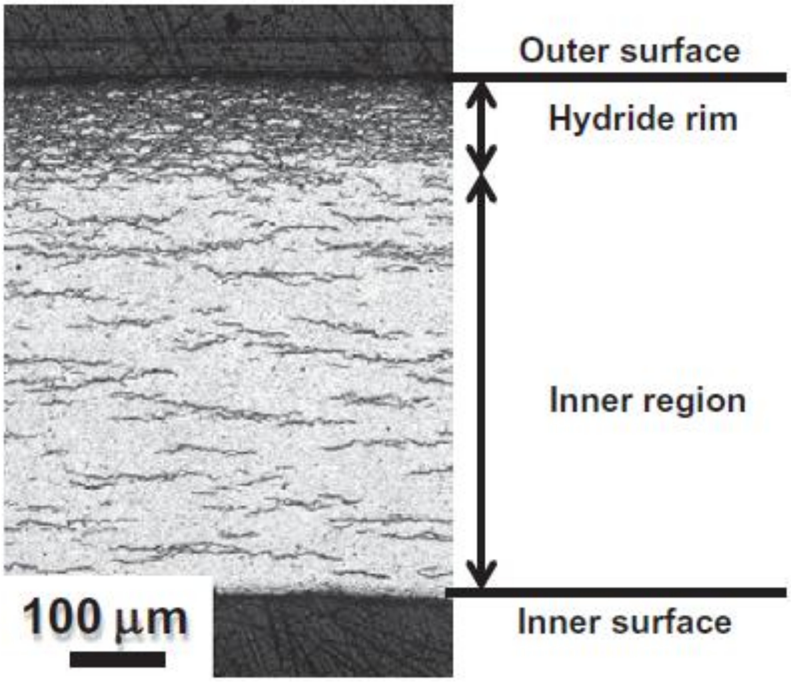

Figure 2.3. Typical Morphology of Hydrides in PWR CWSRA Cladding (Nagase 2011)

The dense hydride rim observed in PWRs is very important in fuel-failure scenarios because it has been shown to be sensitive to cracking at low stresses in the elastic deformation region. The depth of the hydride region and crack length have been found to be critical in determining whether the crack arrests or proceeds through the more ductile (lower hydrogen levels) of the cladding wall below the rim, resulting in through-wall failure. A rough rule of thumb on rim thickness to average hydrogen level at any given circumferential location is that 80 µm of oxide results in a rim of about 80- to 100-µm thickness. This rule of thumb does not apply to rim thickness at locations where the oxide has spalled off, or at locations where the cladding temperature is low, such as at pellet-pellet interfaces or under the spacer grids.

Garde et al. (2009) provided hydride distributions in high burnup PWR ZIRLO (CWSRA) cladding (rod average burnup 68 GWd/MTU) both radially across the cladding wall, at mid-pellet and at pellet-pellet interfaces, see table 1 of Garde et al. (2009). The hydrogen content varies considerably in the radial direction across the cladding wall with the outer rim of the wall having a factor of 5 to 25 higher density of hydrides than the inner portion of the wall thickness. The average of hydrogen content in the cladding wall at the pellet-pellet interface (~ 1/8 inch length) was approximately 50% greater than at the mid-pellet. Because hydride density at the outer rim of the cladding appears to control crack propagation, crack propagation is more likely at the location of pellet-pellet interfaces (location of peak stresses for PCMI and also peak stresses due to bending during transportation. Hour-glassing of the fuel pellet is also known to be greater at pellet-pellet interfaces, which results in ridging of the cladding that can also increase the local stresses at these ridge locations.

The final heat treatment of M5™ is a recrystallization anneal (RXA) that leaves the cladding in a fully recrystallized condition. Because of the grain structure and texture in an RXA cladding tube, the zirconium hydride precipitates out randomly in both radial and circumferential orientations. Radial hydrides are more detrimental than circumferential hydrides because they allow radial cracks to propagate more readily through a brittle hydride. Fortunately, M5™ is fairly resistant to corrosion and has a low hydrogen pickup so that even at high burnup, M5™ cladding tubes do not typically show a large level of hydrogen. At high burnup, M5™ typically has 15-20 μm of oxide and 80-110 ppm of hydrogen compared to Zircaloy-4 with 80-100 μm of oxide and 550-700 ppm of hydrogen.

The reduction in cladding ductility and reduction in fracture toughness have been found to correlate well with the level of excess hydrogen, or hydrogen above the solubility level. This is the hydrogen that will be precipitated out as zirconium hydride. The excess hydrogen, H_{ex}, can be found by calculating the hydrogen solubility limit at the cladding temperature and subtracting the solubility limit from the total hydrogen in the cladding (H_{ex} not less than zero).

$$H_{Ex} = H_{Tot} - H_{sol}$$

The solubility of hydrogen in zirconium is predicted using the Kearns' solubility model given by:

$$H_{sol} = 1.2 \times 10^{5} \exp\left(\frac{-8550}{1.985887 \cdot T}\right)$$

where:

H_{Ex} = excess hydrogen, wt. ppm

T_{tot} = total hydrogen predicted using the pickup fraction, wt. ppm

H_{sol} = hydrogen solubility, wt. ppm

T = temperature, K

As stated before, hydride orientation in a PWR fuel rod with CWSRA cladding is nearly always in the circumferential direction on discharge from the reactor. Both ZIRLO and Zircaloy-4 cladding materials are CWSRA while M5 cladding is RXA, which results in a more random orientation of hydrides. These circumferential hydrides can be reoriented in the radial direction if a temperature high enough to place enough of the hydrogen back in solution (> 250°C, 32 ppm in solution) and then cool the cladding down under a tensile hoop stress (75 to 80 MPa) starts to initiate for cold-work stress-relief annealed cladding (Daum et al. 2005). The degree of orientation depends on initial temperature from cooling and cooling rate (Aomi et al. 2008). If sufficient radial hydrides (in terms of amount and length) are present, they can result in brittle fracture at hoop stresses in the elastic region (less than yield strength) below the ductile-to-brittle transition temperature (DBTT). It will most likely take a hoop stress of at least 90 to 100 MPa to get sufficient radial hydrides to affect the cladding ductility. The temperature at which cooling takes place also has an effect on the amount of reorientation as well as hoop stress level as discussed by Aomi et al. 2008. For example, a slow cooling rate and high initial cooling temperature of 400°C may reduce the stress level for significant reorientation to as low as 90 to 95 MPa, a faster cooling rate or lower initial temperature will increase this stress level.

As noted earlier M5 cladding has a more random orientation of hydrides (includes radial hydrides) that can result in less ductile behavior than CWSRA cladding at equivalent hydrogen levels. In addition, RXA cladding has a lower tensile hoop stress level, about 40 to 60 MPa, that depends on temperature from cooling and cooling rate for the initiation of reorientation of hydrides in the radial direction (Aomi et al. 2008). Similar to CWSRA cladding, a stress level of at least 10 to 20 MPa higher than for the initiation of reorientation for RXA cladding will most likely be required to achieve sufficient radial hydrides to affect cladding ductility, but this will depend on initial cooling temperature and cooling rate (Aomi et al. 2008).

2.4 Level of In-Reactor Wear and Fretting

There are two basic types of grid fretting, grid-to-rod fretting (GTRF) and baffle jet fretting. Both of these are primarily present in PWRs and caused by flow-induced vibrations of the grid spacer springs against the fuel rod, creating wear that can penetrate the fuel rod cladding resulting in failure. The GTRF wear is different from baffle jet wear because the former results from spacer-spring relaxation creating a gap between the spacer spring and fuel rod, and cross flows from adjacent assemblies that may be different in design that results in the cross flow between the two assembly types. The number of assemblies with GTRF failures varied from 10 to 100 assemblies between 1990 to 2005, averaging approximately 60 assemblies per year (Kesterson and Sindelar 2013).

The baffle jet failures occurred in the 1980s and 1990s but there have been several plants that experienced this type of failure in early 2000s. From the mid-1990s to mid-2000s fretting failures made up greater than 50% of the observed failures in PWRs with anywhere from 20 to 90 fuel assemblies containing failed fuel rods per year were found during this time period. The majority of the more than 100 assemblies containing fuel rods with baffle jet failures in 2002 and

2003 came from just two plants. The number of assemblies with failed rods from fretting has decreased in recent years because of changes in the assembly design.

Analyses performed by fuel vendors usually assume normal fretting wear and fabrication flaws (not caught by examination) will be 10% of the minimum wall thickness.

If sensitivity studies are performed to examine the impact of in-reactor wear and fretting, this value of 10% of the minimum wall thickness should be used as a reasonable limit on fretting wear.

2.5 Example Values

The following tables (Table 2.5 through Table 2.8) show typical conditions at 1-ft intervals for the peak rod from assemblies discharged at 30, 40, 50, and 55 GWd/MTU assembly average burnup. These tables were developed with calculations from FRAPCON-3.4 (Geelhood et al. 2010a). No fuel cladding gap is predicted in moderate to high burnup fuel when cooled to room temperature. The contact pressure is removed, but there is no effective gap predicted beyond the sum of the fuel and cladding roughness (about 2.5 μm). The conditions shown in these tables are for the peak rod in the assembly. These conditions may conservatively be used for all the rods in an assembly. The oxide layer predicted should be assumed to be in place on the rod, but offer no load-carrying capability. The cladding should be thinned using the Pillings-Bedworth as discussed in Section 2.3.2**Error! Reference source not found.**.

Table 2.5. Typical Conditions for Peak Fuel Rod from PWR Westinghouse 17x17 Fuel Assembly Discharged at Assembly Average Burnup of 30 GWd/MTU.

				PWR Westinghouse 17x17 Fuel Assembly							
		Assembly Average Burnup			30	GWd/MTU	Cladding material: Zircaloy-4				
		Peak Rod Average Burnup			32.1	GWd/MTU	Peak Rod Fast Neutron Fluence			5.36E+25	n/m²
Upper Plenum	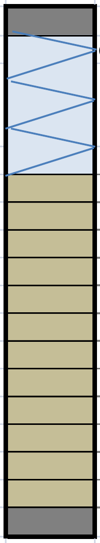	Gas Composition 99.0% He, 0.8% Xe, 0.2% Kr				Total void volume = 10.43 cm³			Total Gas = 1.7e-2 Moles		
		Local Burnup GWd/MTU	Local Fast Neutron Fluence n/m²	Corrosion layer Thickness µm	Metal Consumed µm	Hydrogen Concentration ppm	Excess Hydrogen @ 20°C ppm	Excess Hydrogen @ 100°C ppm	Excess Hydrogen @ 200°C ppm	Excess Hydrogen @ 300°C ppm	Excess Hydrogen @ 400°C ppm
node 12		24.5	4.11E+25	29.1	18.7	243	243	242	230	178	43
node 11		31.1	5.20E+25	33.8	21.7	281	281	280	268	216	81
node 10		34.1	5.71E+25	33.7	21.6	281	281	280	268	216	81
node 9		34.7	5.81E+25	27.8	17.8	232	232	231	219	167	32
node 8		34.7	5.81E+25	24.3	15.6	204	204	203	191	139	4
node 7		34.7	5.80E+25	19.5	12.5	166	166	165	153	101	0
node 6		34.6	5.79E+25	17.1	11	146	146	145	133	81	0
node 5		34.6	5.78E+25	13.7	8.8	119	119	118	106	54	0
node 4		34.5	5.78E+25	11	7.1	97	97	96	84	32	0
node 3		33.7	5.65E+25	7.8	5	72	72	71	59	7	0
node 2		29.8	4.99E+25	5.1	3.3	50	50	49	37	0	0
node 1		23.4	3.92E+25	2	1.3	26	26	25	13	0	0

Table 2.6. Typical Conditions for Peak Fuel Rod from PWR Westinghouse 17x17 Fuel Assembly Discharged at Assembly Average Burnup of 40 GWd/MTU.

PWR Westinghouse 17x17 Fuel Assembly

Assembly Average Burnup	40 GWd/MTU	Cladding material: Zircaloy-4	
Peak Rod Average Burnup	42.6 GWd/MTU	Peak Rod Fast Neutron Fluence	7.13E+25 n/m²

Upper Plenum

Gas Composition 96.0% He, 3.4% Xe, 0.6% Kr

Total void volume = 10.57 cm³

Total Gas = 1.7e-2 Moles

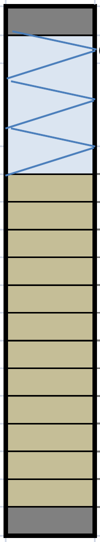

	Local Burnup GWd/MTU	Local Fast Neutron Fluence n/m²	Corrosion layer Thickness µm	Metal Consumed µm	Hydrogen Concentration ppm	Excess Hydrogen @ 20°C ppm	Excess Hydrogen @ 100°C ppm	Excess Hydrogen @ 200°C ppm	Excess Hydrogen @ 300°C ppm	Excess Hydrogen @ 400°C ppm
node 12	32.6	5.46E+25	42.5	27.2	353	353	352	340	288	153
node 11	41.3	6.92E+25	51.3	32.9	426	426	425	413	361	226
node 10	45.4	7.60E+25	51.8	33.2	430	430	429	417	365	230
node 9	46.1	7.72E+25	42.7	27.4	355	355	354	342	290	155
node 8	46.2	7.73E+25	36.9	23.7	307	307	306	294	242	107
node 7	46.1	7.71E+25	29.8	19.1	248	248	247	235	183	48
node 6	46	7.70E+25	25.7	16.5	215	215	214	202	150	15
node 5	45.9	7.69E+25	20.9	13.4	176	176	175	163	111	0
node 4	45.9	7.68E+25	17	10.9	145	145	144	132	80	0
node 3	44.8	7.51E+25	12.6	8.1	110	110	109	97	45	0
node 2	39.6	6.63E+25	8.6	5.5	78	78	77	65	13	0
node 1	31.1	5.21E+25	4.4	2.8	45	45	44	32	0	0

Table 2.7. Typical Conditions for Peak Fuel Rod from PWR Westinghouse 17x17 Fuel Assembly Discharged at Assembly Average Burnup of 50 GWd/MTU.

PWR Westinghouse 17x17 Fuel Assembly

		Assembly Average Burnup			50	GWd/MTU	Cladding material: Zircaloy-4				
		Peak Rod Average Burnup			53.7	GWd/MTU	Peak Rod Fast Neutron Fluence			8.99E+25	n/m²
Upper	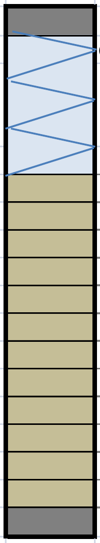	Gas Composition 88.2% He, 10.0% Xe, 1.8% Kr				Total void volume = 10.81 cm³			Total Gas = 1.9e-2 Moles		
Plenum		Local Burnup GWd/MTU	Local Fast Neutron Fluence n/m²	Corrosion layer Thickness µm	Metal Consumed µm	Hydrogen Concentration ppm	Excess Hydrogen @ 20°C ppm	Excess Hydrogen @ 100°C ppm	Excess Hydrogen @ 200°C ppm	Excess Hydrogen @ 300°C ppm	Excess Hydrogen @ 400°C ppm
node 12		41.2	6.89E+25	56.8	36.4	472	472	471	459	407	272
node 11		52.1	8.73E+25	71.2	45.6	593	593	592	580	528	393
node 10		57.3	9.58E+25	72.9	46.7	608	608	607	595	543	408
node 9		58.2	9.74E+25	59.8	38.3	497	497	496	484	432	297
node 8		58.2	9.75E+25	50.9	32.6	423	423	422	410	358	223
node 7		58.1	9.73E+25	41	26.3	341	341	340	328	276	141
node 6		58.1	9.72E+25	35.1	22.5	292	292	291	279	227	92
node 5		58	9.70E+25	28.6	18.3	239	239	238	226	174	39
node 4		57.9	9.69E+25	23.5	15.1	197	197	196	184	132	0
node 3		56.6	9.47E+25	17.9	11.5	152	152	151	139	87	0
node 2		49.9	8.36E+25	12.4	7.9	109	109	108	96	44	0
node 1		39.3	6.58E+25	7.1	4.6	66	66	65	53	1	0

Table 2.8. Typical Conditions for Peak Fuel Rod from PWR Westinghouse 17x17 Fuel Assembly Discharged at Assembly Average Burnup of 55 GWd/MTU.

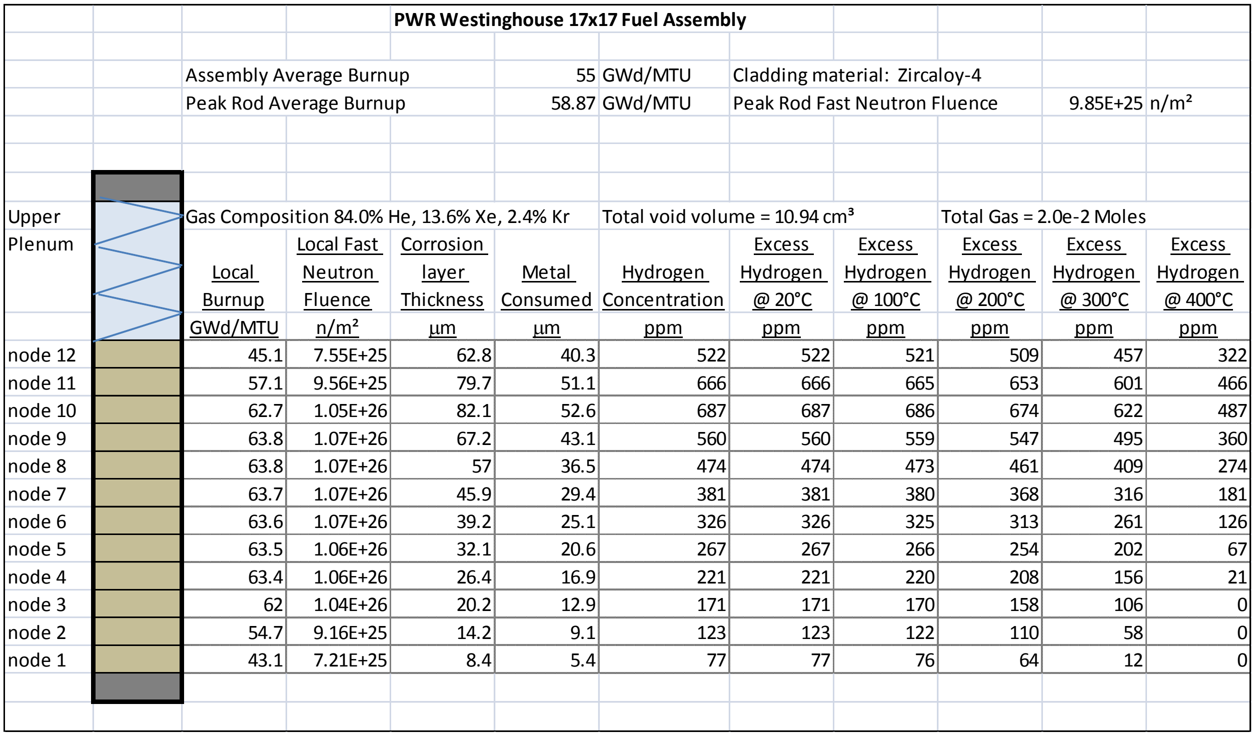

PWR Westinghouse 17x17 Fuel Assembly

Assembly Average Burnup 55 GWd/MTU Cladding material: Zircaloy-4
Peak Rod Average Burnup 58.87 GWd/MTU Peak Rod Fast Neutron Fluence 9.85E+25 n/m²

Upper Plenum
Gas Composition 84.0% He, 13.6% Xe, 2.4% Kr Total void volume = 10.94 cm³ Total Gas = 2.0e-2 Moles

	Local Burnup GWd/MTU	Local Fast Neutron Fluence n/m²	Corrosion layer Thickness µm	Metal Consumed µm	Hydrogen Concentration ppm	Excess Hydrogen @ 20°C ppm	Excess Hydrogen @ 100°C ppm	Excess Hydrogen @ 200°C ppm	Excess Hydrogen @ 300°C ppm	Excess Hydrogen @ 400°C ppm
node 12	45.1	7.55E+25	62.8	40.3	522	522	521	509	457	322
node 11	57.1	9.56E+25	79.7	51.1	666	666	665	653	601	466
node 10	62.7	1.05E+26	82.1	52.6	687	687	686	674	622	487
node 9	63.8	1.07E+26	67.2	43.1	560	560	559	547	495	360
node 8	63.8	1.07E+26	57	36.5	474	474	473	461	409	274
node 7	63.7	1.07E+26	45.9	29.4	381	381	380	368	316	181
node 6	63.6	1.07E+26	39.2	25.1	326	326	325	313	261	126
node 5	63.5	1.06E+26	32.1	20.6	267	267	266	254	202	67
node 4	63.4	1.06E+26	26.4	16.9	221	221	220	208	156	21
node 3	62	1.04E+26	20.2	12.9	171	171	170	158	106	0
node 2	54.7	9.16E+25	14.2	9.1	123	123	122	110	58	0
node 1	43.1	7.21E+25	8.4	5.4	77	77	76	64	12	0

3. CLADDING PROPERTIES

This section describes the cladding properties that will be necessary for modeling the fuel assemblies. Most of these models come from FRAPCON-3 (Geelhood et al. 2010a) or MATPRO (Siefken et al. 2001). Comparisons of model predictions to data are provided with irradiated data shown differently from unirradiated data. As appropriate, the calculated uncertainty and the distribution on that uncertainty are provided. The Zircaloy-4 cladding tubes are pictured in Figure 3.1.

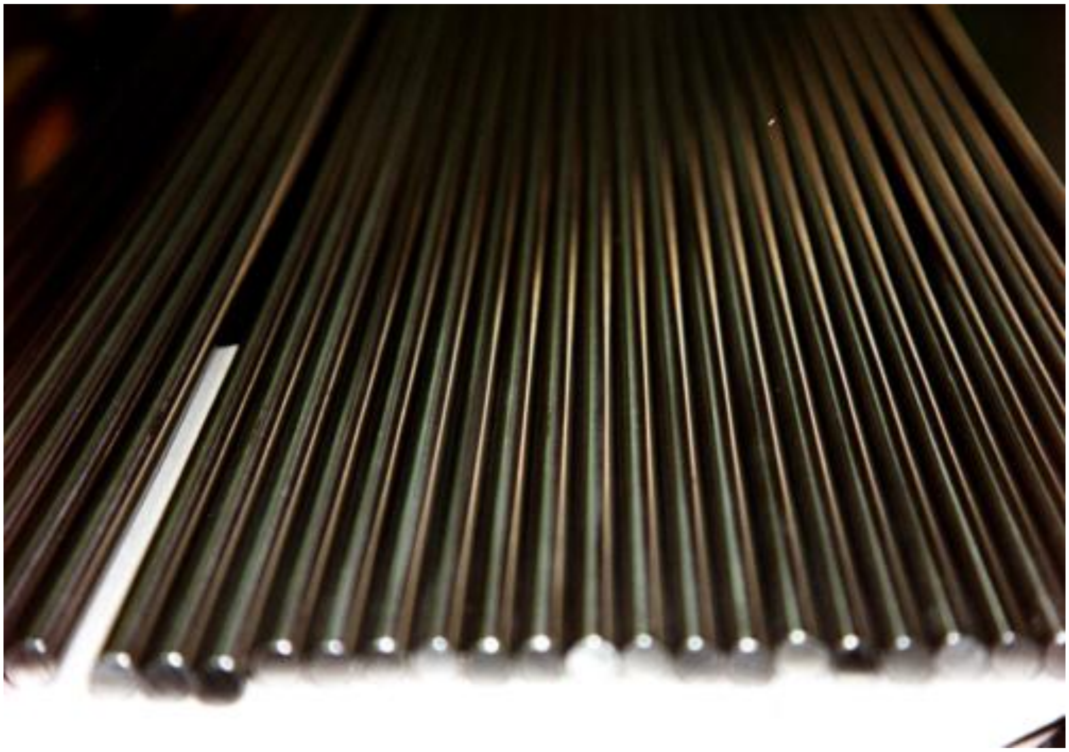

Figure 3.1. Zircaloy-4 Cladding Tubes

The stress-versus-strain behavior of Zircaloy-4 is described by two different correlations, depending on the stress. Before yield, Hooke's law is used to describe the elastic deformation of the Zircaloy according the equation below.

$$\sigma = \varepsilon \cdot E \qquad \text{Equation 1}$$

where:

σ = stress

ε = strain

E = elastic modulus

After yield, the power law is used to describe the plastic deformation of the Zircaloy.

$$\sigma = K \cdot \varepsilon^{n} \left(\frac{\dot{\varepsilon}}{10^{-3}} \right)^{m} \qquad \text{Equation 2}$$

where:

K = strength coefficient

n = strain hardening exponent

m = strain rate exponent

$\dot{\varepsilon}$ = strain rate, s-1

A sample true stress versus true strain curve can be seen in Figure 3.2. In this figure, the true stress strain behavior that is predicted by the model can be seen. The two parts, elastic and plastic, which make up this curve, as described above, can also be seen.

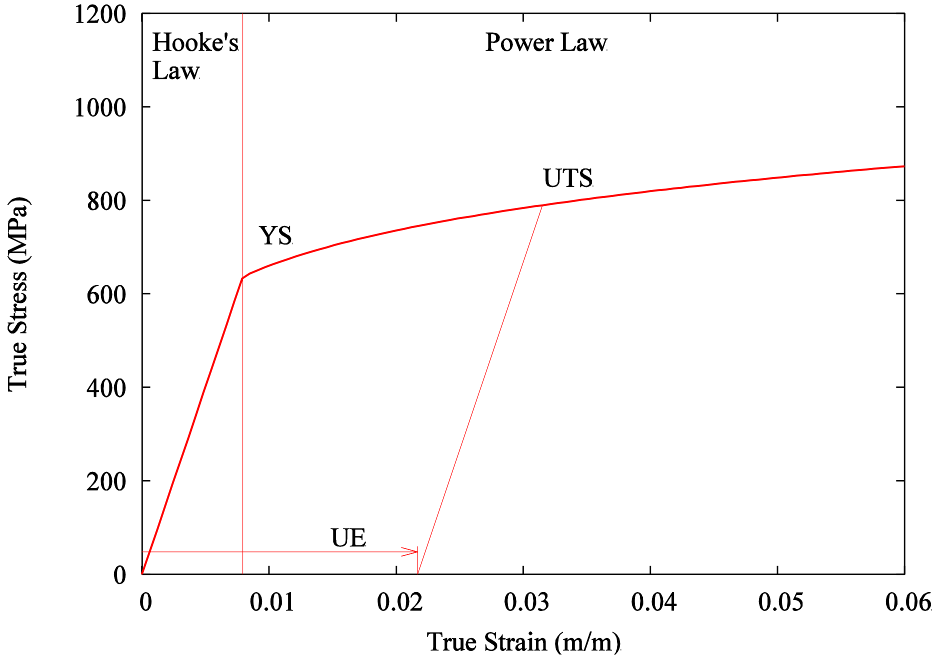

Figure 3.2. Sample True Stress vs. True Strain Curve Using New Model

3.1 Elastic Modulus

This section describes the model, data comparison, and uncertainty for elastic modulus.

3.1.1 Model

The model used in FRAPCON-3.4 and FRAPTRAN 1.4 for Elastic Modulus is given by:

$$E = (1.088 \times 10^{11} - 5.475 \times 10^{7} T + K_1 + K_2) / K_3$$

where:

E = Elastic modulus for Zircaloy-4 (Pa)

T = cladding temperature (K)

K_1 = modification to account for the effect of oxidation (Pa)

K_2 = modification to account for the effect of cold work (Pa)

K_3 = modification to account for the effect of fast neutron fluence (unit-less)

The terms used to modify the general equation are given by:

$$K_1 = (6.61 \times 10^{11} + 5.912 \times 10^{8} T)\, \Delta$$

$$K_2 = -2.6 x 10^{10} C$$

$$K_3 = 0.88 + 0.12 \exp\left(-\frac{\Phi}{10^{25}}\right)$$

where:

Δ = average oxygen concentration minus oxygen concentration of as-received cladding (kg oxygen/kg Zircaloy). Always use 0.0012 kg oxygen/kg Zircaloy

C = cold work (unit-less ratio of areas). Use 0.5 for Zircaloy-4 and ZIRLO™. Use 0.0 for M5™

Φ = fast neutron fluence (n/m2).

The model used in FRAPCON-3.4 and FRAPTRAN 1.4 for shear modulus is given by:

$$G = (4.04 \times 10^{10} - 2.168 \times 10^{7} T + K_1 + K_2) / K_3$$

where:

G = shear modulus for Zircaloy-4, ZIRLO™ and M5™ (Pa)

T = cladding temperature (K)

K_1 = modification to account for the effect of oxidation (Pa)

K_2 = modification to account for the effect of cold work (Pa)

K_3 = modification to account for the effect of fast neutron fluence (unit-less)

The terms used to modify the general equation are given by:

$$K_1 = (7.07 \times 10^{11} + 2.315 \times 10^{8} T)\Delta$$

$$K_2 = -0.867 \times 10^{10} C$$

$$K_3 = 0.88 + 0.12 \exp\left(-\frac{\Phi}{10^{25}}\right)$$

where:

Δ = average oxygen concentration minus oxygen concentration of as-received cladding (kg oxygen/kg Zircaloy). Always use 0.0012 kg oxygen/kg Zircaloy

C = cold work (unit-less ratio of areas). Use 0.5 for Zircaloy-4 and ZIRLO™. Use 0.0 for M5™

Φ = fast neutron fluence (n/m2).

3.1.2 Data Comparison

Figure 3.3 shows a plot of the predicted and measured Elastic modulus for Zircaloy-4 cladding and the corresponding 2-σ upper and lower bounds. These data were taken at various temperatures (Armstrong and Brown 1964, Bolmaro and Povolo 1988, Bunnell et al. 1977, Busby 1966, Fisher and Renken 1964, Mehan 1958, Mehan and Wiesinger 1961, Northwood et al. 1975, Padel and Groff 1976, Shober et al. 1957, Spasic et. al 1968, Whitmarsh 1962). Above 90 GPa the model under-predicts by about 10%. These data were taken at room temperature, which is not of interest for this application.

All of the data shown here are for unirradiated Zircaloy. The effect of irradiation was deduced from data from the Saxton Core II Fuel Performance Evaluation (Smalley 1971). The data shown below are primarily from RXA cladding, but include some CWSRA cladding. The effect of cold work was deduced from Bunnell's measurements of CWSRA cladding and RXA cladding (Bunnell et al.1977).

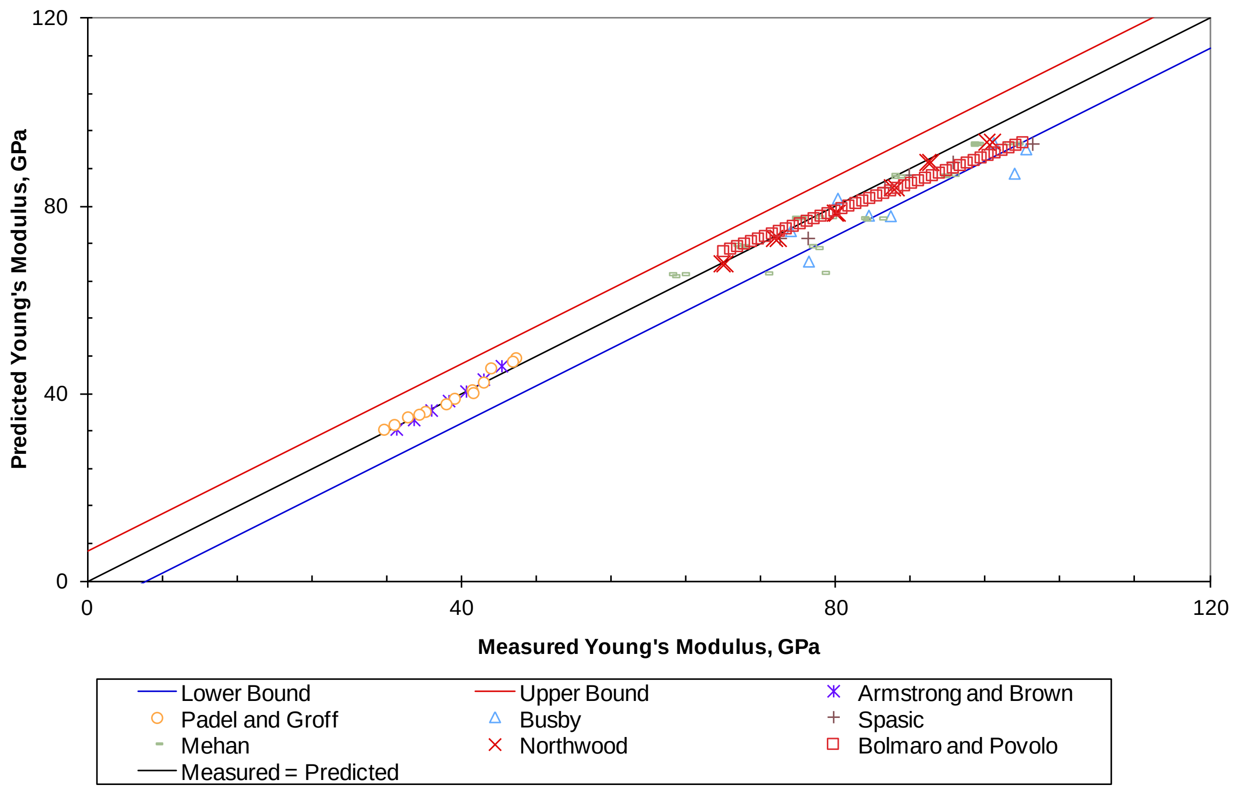

Figure 3.3. Predicted vs. Measured Elastic Modulus for Unirradiated Data

3.1.3 Uncertainty

The standard error of the correlation for Elastic modulus is 6.4 x 109 Pa.

The standard error of the correlation for shear modulus is 9 x 109 Pa.

The distribution of the uncertainties for the Elastic modulus data is shown in Figure 3.4.

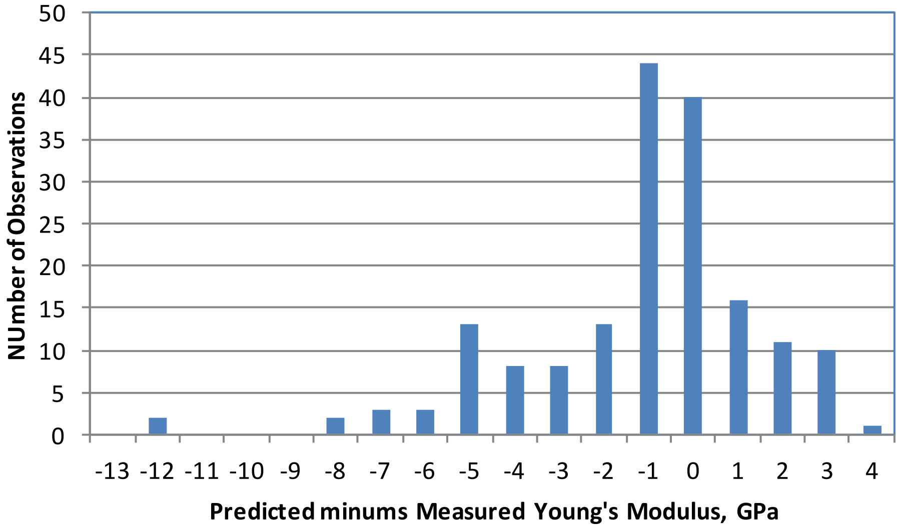

Figure 3.4. Distribution of Uncertainty for Elastic Modulus for Unirradiated Data

It has been noted that the data of these models are from cladding that was recently (approximately 6 months) removed from the reactor. The short term vacuum drying operation at temperatures up to 400°C is not expected to cause any changes, but the 20 or more years spent in dry cask storage at 100°C-400°C may result in annealing of irradiation damage or in grain growth. Some experimental data exist that show the microhardness of irradiated Zircaloy-4 CWSRA will increase by 20% following irradiation. Then it will decrease about 50% to 80% of this irradiation-induced hardness increase after being held at 330°C-420°C for 6000 hours (at 330°C) and 1200 hours (at 420°C) (Ito et al. 2004). The Zircaloy4 cladding tested by Ito et al (2004) had a fast fluence of 8 x 1025 n/m^2 with hydrogen levels between 40 to 220 wppm. Bourdiliou et al. (2010) have shown that holding irradiated (up to 4 cycles) Zircaloy4CWSRA cladding at 350°C for 3000 hours results in 86% annealing of the yield strength increase from irradiation. Bourdiliau et al. (2010) annealing data at 400°C and 420°C showed that the yield strength fell below the unirradiated yield strength by approximately 3% after 17,000 and 5,000 hours, respectively. The hydrogen content was not given for the Zircaloy4annealing samples. Bourdiliau et al. observed an increase in ductility (both uniform and total elongation). There was not a complete recovery to the unirradiated ductility. Bourdiliau et al. also presented annealing data for irradiated Zircaloy-1%Nb RXA cladding that demonstrated less annealing of the irradiation strength than for Zircaloy4CWSRA at equivalent annealing conditions at 400°C. It is not clear how the microhardness increase or yield strength relate to the elastic modulus. The elastic modulus is not a strong function of fluence (12% increase from the unirradiated condition to the highly irradiated condition) such that the maximum difference from annealing will be 12%.

3.2 Yield Stress

The yield stress, σ_y, is given as the non-zero intersection of Equations 1 and 2. The intersection of these equations is given in Equation 3.

$$\sigma_y = \left[\frac{K}{E^n} \left(\frac{\dot{\varepsilon}}{10^{-3}} \right)^m \right]^{\left(\frac{1}{1-n}\right)}$$ Equation 3

The elastic modulus, E, was described in Section 3.1. The strength coefficient, K; strain hardening exponent, n; and strain rate exponent, m, are shown in the sections below.

3.2.1 Strength Coefficient, K

The strength coefficient, K, is a function of temperature, fast neutron fluence, cold work, and alloy composition. The models for the strength coefficients of Zircaloy-2 and Zircaloy-4 are given below.

$$K = K(T) \cdot (1 + K(CW) + K(\Phi)) / K(Zry)$$

where:

K = strength coefficient, Pa

$$K(T) = 1.17628 \times 10^9 + 4.54859 \times 10^5 T - 3.28185 \times 10^3 T^2 + 1.72752 \cdot T^3$$ $T<750$K

$$K(T) = 2.522488 \times 10^6 \exp\left(\frac{2.8500027 \times 10^6}{T^2} \right)$$ 750K$<T<$1090K

$$K(T) = 1.841376039 \times 10^8 - 1.4345448 \times 10^5 T$$ 1090K$<T<$1255K

$$K(T) = 4.330 \times 10^7 - 6.685 \times 10^4 T + 3.7579 \times 10^1 T^2 - 7.33 \times 10^{-3} T^3$$ 1255K$<T<$2100K

$$K(CW) = 0.546 \cdot CW$$

$$K(\Phi) = (-0.1464 + 1.464 \times 10^{-25} \Phi) f(CW, T)$$ $\Phi<$ 0.1x1025 n/m^2

$$K(\Phi) = 2.928 \times 10^{-26} \Phi$$ 0.1x1025n/m^2$<\Phi<$ 2x1025 n/m^2

$$K(\Phi) = 0.53236 + 2.6618 \times 10^{-27} \Phi$$ 2x1025 n/m^2$<\Phi<$12x1025 n/m^2

$$f(CW, T) = 2.25 \exp(-20 \cdot CW) \cdot \min\left[1, \exp\left(\frac{T - 550}{10} \right) \right] + 1$$

K(Zry)=1 for Zircaloy-4

K(Zry)=1.305 for Zircaloy-2

T = temperature, K

CW= cold work, unit-less ratio of areas (valid from 0 to 0.75)

Φ = fast neutron fluence, n/m^2 (E>1MeV)

3.2.2 Strain Hardening Exponent, n

The strain hardening exponent, n, is a function of temperature, fast neutron fluence, and alloy composition. The models for the strain hardening exponents of Zircaloy-2 and Zircaloy-4 are given below.

$$n = n(T) \cdot n(\Phi) / n(Zry)$$

where:

n = strain hardening exponent

$n(T) = 0.11405$ T<419.4K

$n(T) = -9.490 \times 10^{-2} + 1.165 \times 10^{-3} T - 1.992 \times 10^{-6} T^2 + 9.588 \times 10^{-10} T^3$ 419.4K<T<1099.0772K

$n(T) = -0.22655119 + 2.5 \times 10^{-4} T$ 1099.0772K<T<1600K

$n(T) = 0.17344880$ T>1600K

$n(\Phi) = 1.321 + 0.48 \times 10^{-25} \Phi$ Φ< 0.1x1025 n/m^2

$n(\Phi) = 1.369 + 0.096 \times 10^{-25} \Phi$ 0.1x1025 n/m^2<Φ< 2x1025 n/m^2

$n(\Phi) = 1.5435 + 0.008727 \times 10^{-25} \Phi$ 2x1025 n/m^2<Φ<7.5x1025 n/m^2

$n(\Phi) = 1.608953$ Φ>7.5x1025 n/m^2

n(Zry) = 1 for Zircaloy-4

n(Zry) = 1.6 for Zircaloy-2

T = temperature, K

Φ = fast neutron fluence, n/m^2 (E>1MeV)

3.2.3 Strain Rate Exponent, m

The strain rate exponent, m, is given by a function of temperature only as described in the equation below.

$m = 0.015$ T<750K

$m = 7.458 \times 10^{-4} T - 0.544338$ 750K<T<800K

$m = 3.24124 \times 10^{-4} T - 0.20701$ T>800K where:

m = strain rate exponent

T = temperature, K

The impact of the strain rate exponent on yield stress is to increase the yield strength with increasing strain rate, but the effect is not large. For example, increasing the strain rate from $1x10^{-4}$/s to 1.0/s will increase the yield strength by about 15%.

3.2.4 Data Comparison

Figure 3.5 shows a plot of the predicted and measured yield stress for Zircaloy-4 cladding and some independent Zircaloy-4 and ZIRLO™ data (Adamson et al. 1986, Averty et al. 2003, Balfour 1982a, Balfour 1982b, Berat et al. 2000, Billone, 2002, Chun et al. 1987, Desquines et al. 2005, Dideon and Bain 1983, Garde 1986, Garde 1989, Garde et al. 1996, Hardy 1970, Kemper and Zimmerman 1957, Kubo et al. 2010, Lowry 1981, Mahmood et al. 1997, Newman 1986, Newman 1990, Pettersson et al. 1979, Smalley 1971, Smith 1983, Smith 1994, Van Swan et al. 1997, Williams et al. 1974, Wisner and Adamson 1998, Yagnik et al 2005). These data were taken at various temperatures and fast neutron fluence. Figure 3.6 shows only the irradiated data. Figure 3.7 shows these same data as predicted minus measured versus fast neutron fluence. The range of strengths relevant to temperatures for used fuel storage is 300-800 Mpa.

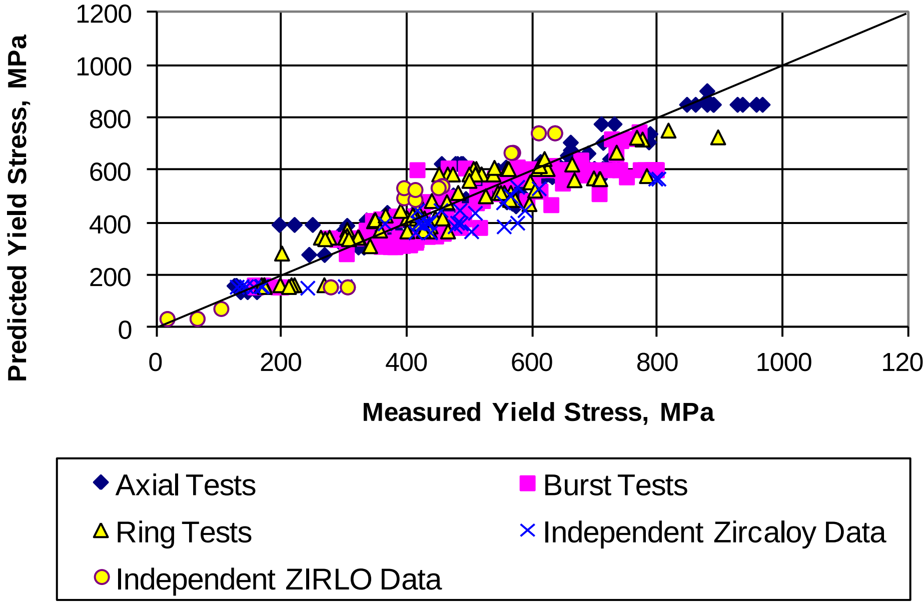

Figure 3.5. Predicted vs. Measured Yield Stress for Irradiated and Unirradiated Data

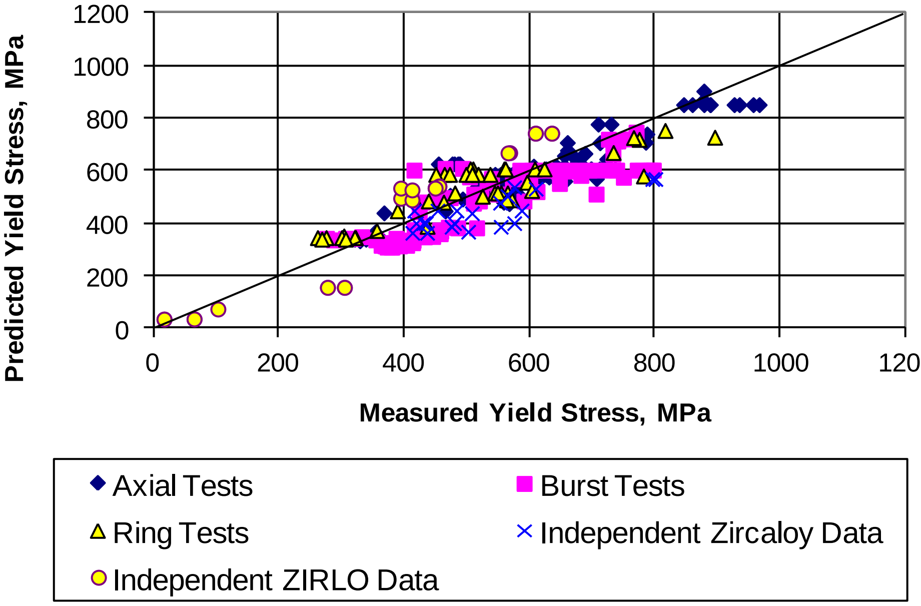

Figure 3.6. Predicted vs. Measured Yield Stress for Irradiated Data

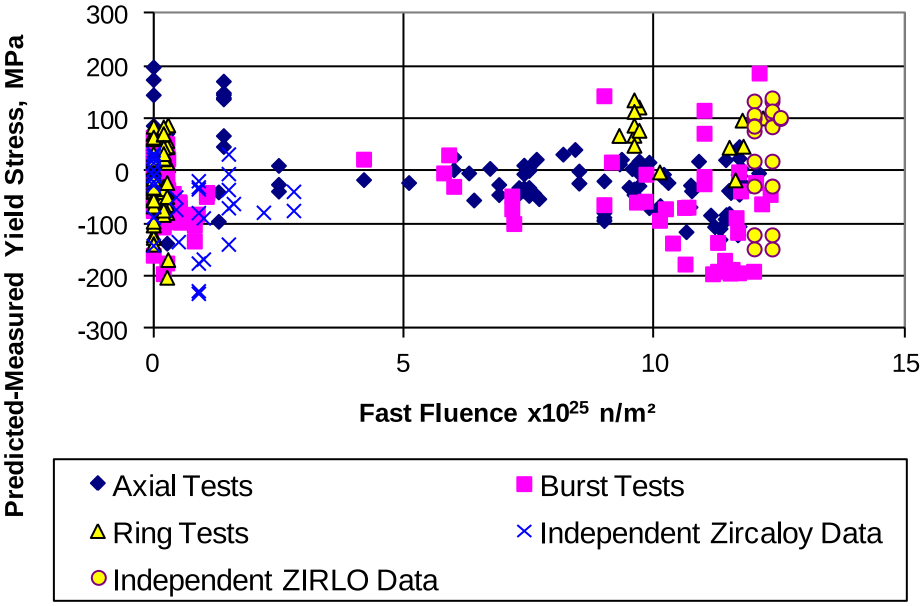

Figure 3.7. Predicted Minus Measured Yield Stress Data vs. Fast Fluence for Irradiated and Unirradiated Data

3.2.5 Uncertainty

The standard error of the yield stress correlation for the entire set of 432 irradiated and unirradiated data points is 65 MPa. The standard error of the yield stress correlation for only the 144 unirradiated data points is 53 MPa. The standard error of the yield stress correlation for only the 288 irradiated data points is 73 MPa. The distribution of the uncertainties for all the data, the unirradiated data, and the irradiated data are shown in Figure 3.8, Figure 3.9, and Figure 3.10, respectively. In Figure 3.10 there appears to be a small bias for under-prediction in the model. When all the data outside the temperature range of interest (150°C to 400°C) is eliminated, there is much less under-prediction observed.

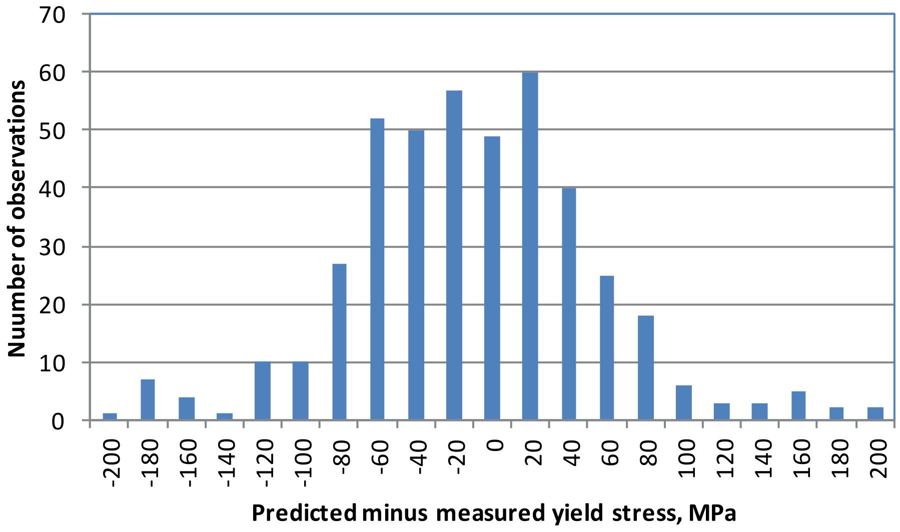

Figure 3.8. Distribution on Uncertainty for Yield Stress for Unirradiated and Irradiated Data

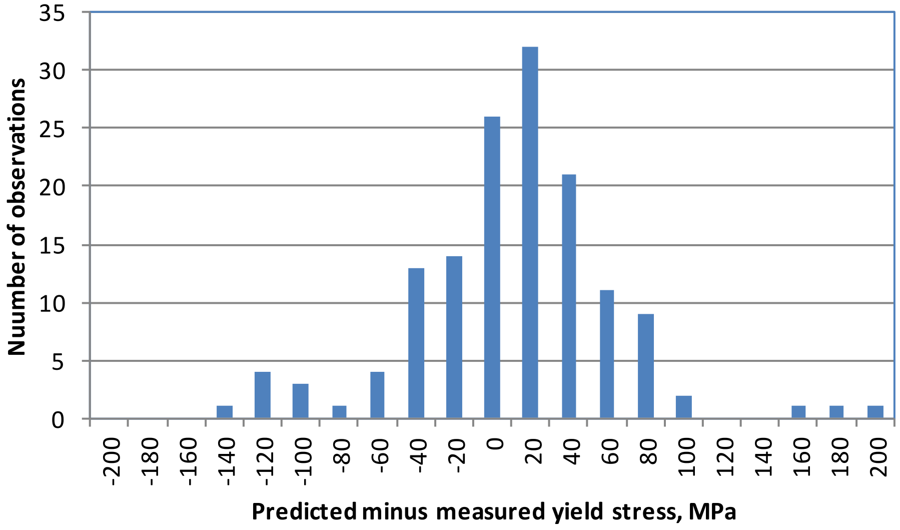

Figure 3.9. Distribution on Uncertainty for Yield Stress for Unirradiated Data

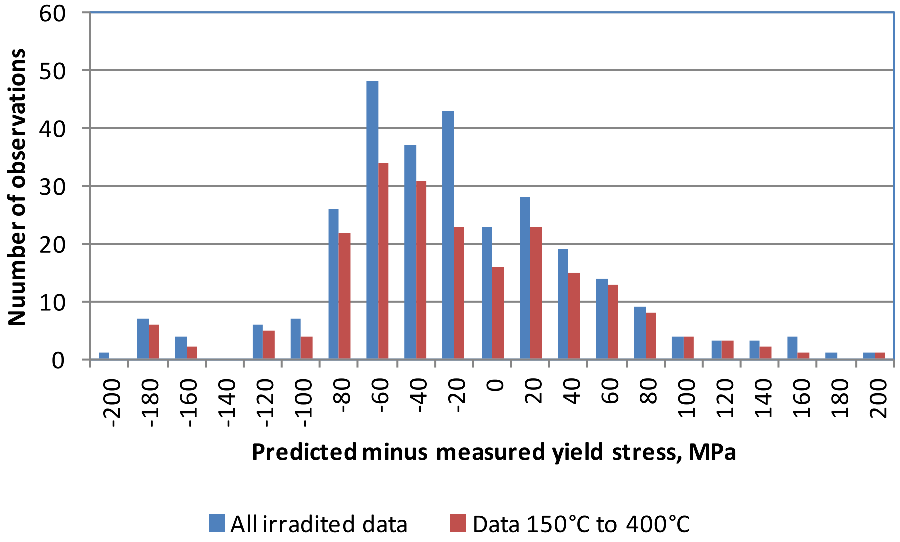

Figure 3.10. Distribution on Uncertainty for Yield Stress for Irradiated Data

It has been noted that the data on which these models are based is taken from cladding that was recently (approximately 6 months) removed from the reactor. The data from Ito et al. 2004 and Bourdiliau et al. 2010 suggests that significant annealing will not occur during cask drying. (See discussion in Section 3.1.3 on the annealing data of irradiated Zircaloy.) These data suggest that annealing is likely to occur in storage and that annealing will significantly decrease the yield and ultimate tensile strength to nearer those of unirradiated levels if cladding temperatures are at 330°C and above for time periods of a few months to more than a year. Some annealing may take place in the 300 to 330°C range if cladding is held in this range for several years, but there is only data at 330°C and above for time periods up to 2 years. Bourdiliau et al. has demonstrated a strong correlation between hardness in Zircaloy and yield stress. An example of the change in yield stress with fast fluence in Zircaloy-4 at 315°C is shown in Figure 3.11.

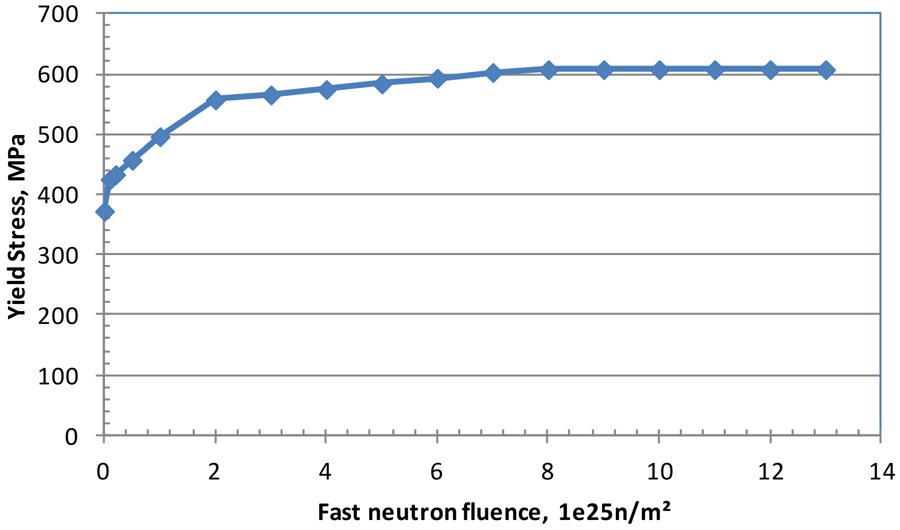

Figure 3.11. Change in Yield Stress with Increasing Fast Neutron Fluence at 315°C

3.3 Ultimate Tensile Strength

This section describes the model, data comparison, and uncertainty for ultimate tensile strength.

3.3.1 Model

The ultimate tensile strength can be approximated by the stress predicted by Equation 2, when the strain is the sum of the plastic strain at maximum load and the strain at yield, σ_y/E. The plastic strain at maximum load is typically referred to as uniform elongation (UE) by the fuel vendors.

$$\sigma_{UTS} = K \cdot \left(\frac{\sigma_y}{E} + UE \right)^n \left(\frac{\dot{\varepsilon}}{10^{-3}} \right)^m$$

3.3.2 Data Comparison

Figure 3.12 shows a plot of the predicted and measured ultimate tensile strength for Zircaloy-4 cladding and some independent Zircaloy-4 and ZIRLO™ data (Adamson et al. 1986, Averty et al. 2003, Balfour 1982a, Balfour 1982b, Berat et al. 2000, Billone, 2002, Chun et al. 1987, Desquines et al. 2005, Dideon and Bain 1983, Garde 1986, Garde 1989, Garde et al. 1996, Hardy

1970, Kemper and Zimmerman 1957, Kubo et al. 2010, Lowry 1981, Mahmood et al. 1997, Newman 1986, Newman 1990, Pettersson et al. 1979, Smalley 1971, Smith 1983, Smith 1994, Van Swan et al. 1997, Williams et al. 1974, Wisner and Adamson 1998, Yagnik et al 2005) (independent data not used for model development). These data were taken at various temperatures and fast neutron fluence. Figure 3.13 shows these same data as predicted minus measured versus fast neutron fluence.

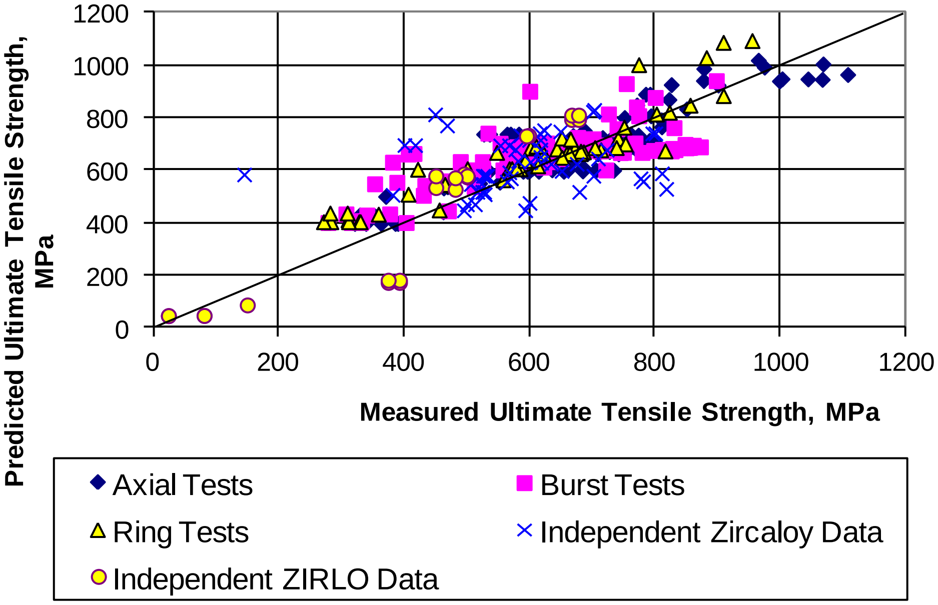

Figure 3.12. Predicted vs. Measured Ultimate Tensile Strength for Irradiated and Unirradiated Data

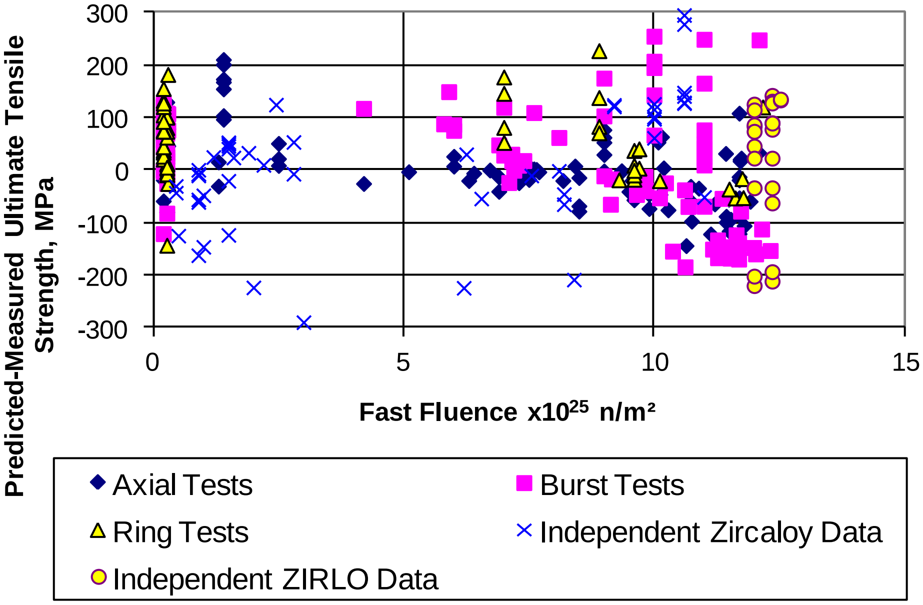

Figure 3.13. Predicted Minus Measured Ultimate Tensile Strength Data vs. Fast Fluence for Irradiated and Unirradiated Data

3.3.3 Uncertainty

The standard error of the ultimate tensile strength correlation for the entire set of 419 irradiated and unirradiated data points is 79 MPa. The standard error of the ultimate tensile strength correlation for only the 150 unirradiated data points is 57 MPa. The standard error of the ultimate tensile strength correlation for only the 269 irradiated data points is 90 MPa. The distribution of the uncertainties for all the data, the unirradiated data, and the irradiated data are shown in Figure 3.14, Figure 3.15, and Figure 3.16, respectively.

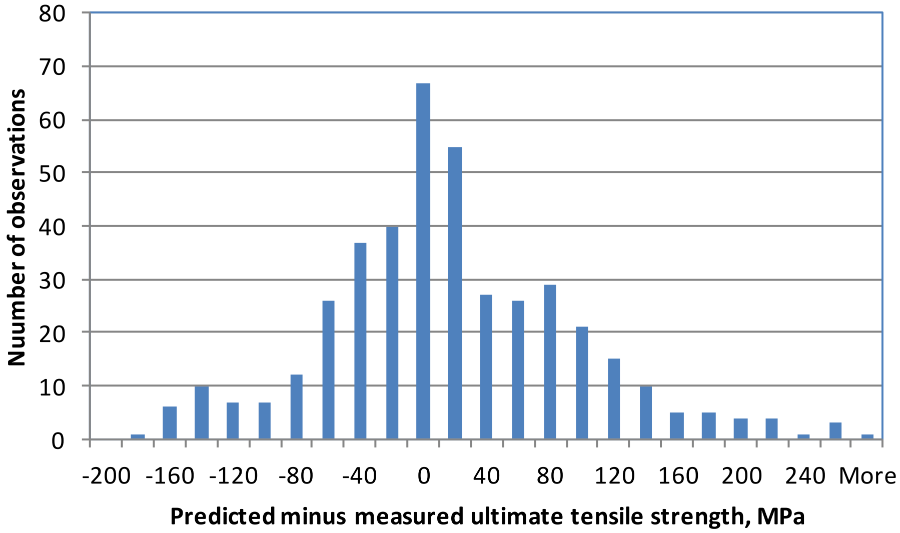

Figure 3.14. Distribution on Uncertainty for Ultimate Tensile Strength for Unirradiated and Irradiated Data

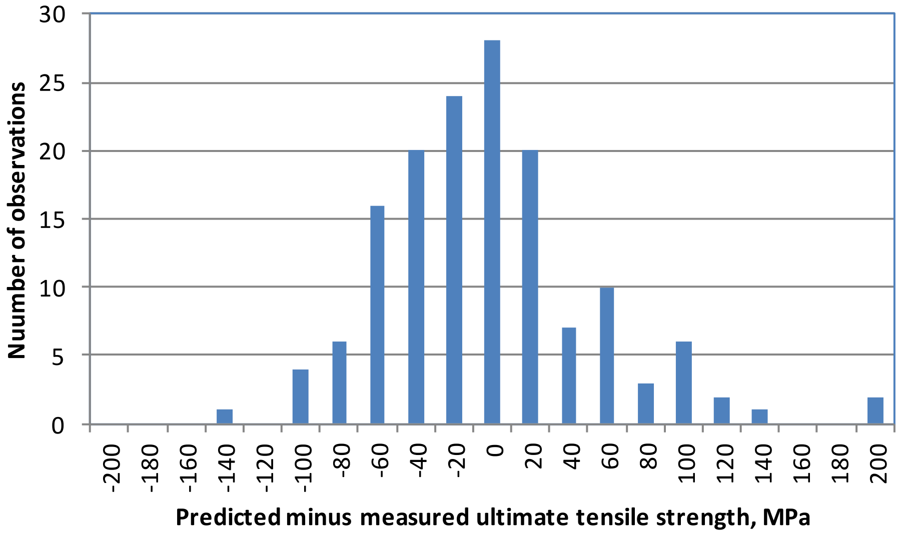

Figure 3.15. Distribution on Uncertainty for Ultimate Tensile Strength for Unirradiated Data

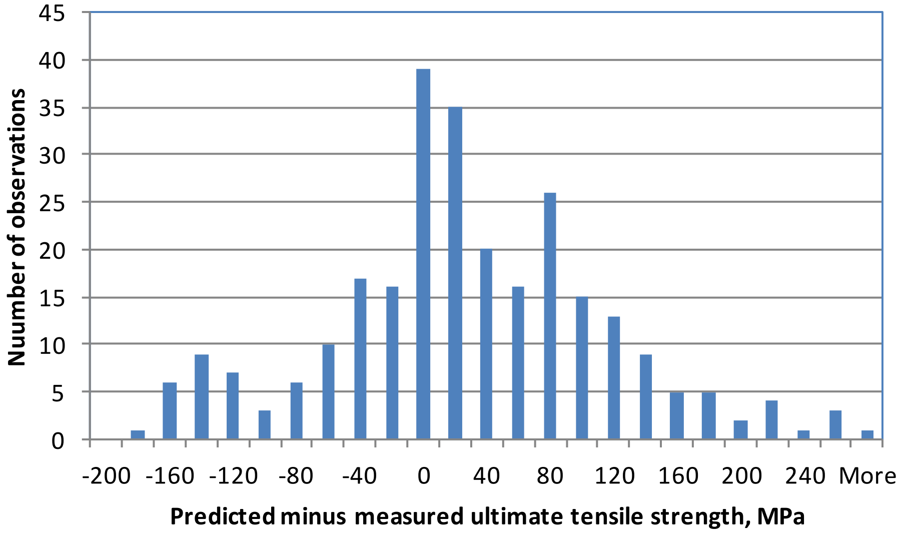

Figure 3.16. Predicted Minus Measured Ultimate Tensile Strength Data vs. Fast Fluence for Irradiated Data

It has been noted that the data of these models are from cladding that was recently (approximately 6 months) removed from the reactor without annealing. Bourdiliau et al. (2010) has demonstrated a strong correlation between the change in hardness and the change in ultimate tensile strength. An example of the change in ultimate tensile strength in Zircaloy-4 at 315°C is shown in Figure 3.17**Error! Reference source not found.**. The ultimate tensile strength is a strong function of fluence (63% increase from the unirradiated condition to the highly irradiated condition) and the increase with fluence begins to saturate at low values (50% increase has occurred by 2 x 1025 n/m^2). Annealing of the irradiation damage will result in a decrease in the ultimate tensile strength similar to the decrease in the yield stress.

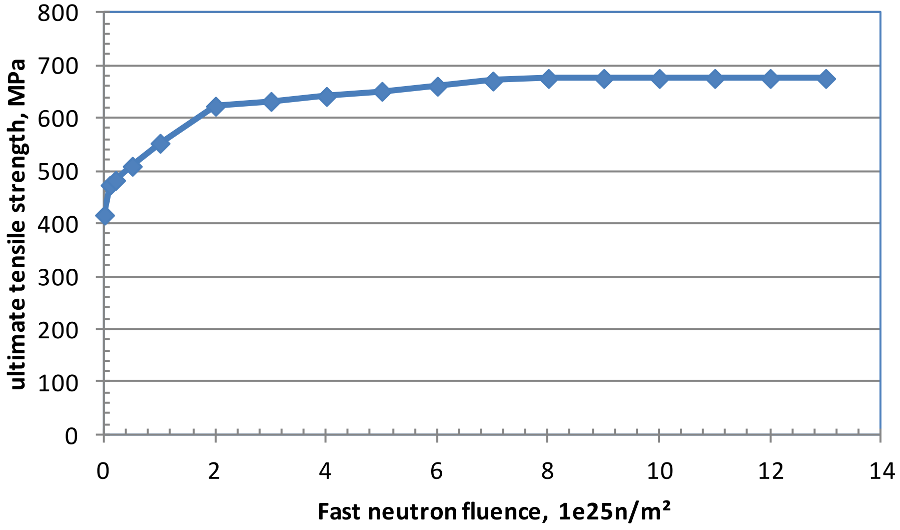

Figure 3.17. Change in Ultimate Tensile Strength with Increasing Fast Neutron Fluence at 315°C

3.4 Uniform Elongation and Total Elongation

This section describes the model, data comparison, and uncertainty for uniform elongation and total elongation.

3.4.1 Model

The model for uniform plastic elongation for irradiated Zircaloy is given below. This model can be used for unirradiated Zircaloy, but there is considerable scatter in the unirradiated data. It is noted that this model is based on irradiated Zircaloy cladding containing circumferential hydrides. This model was developed for predicting strain to failure for pellet-cladding mechanical interaction (PCMI) in-reactor that is a biaxial (axial and hoop) stress state. As a result the model was developed primarily based on burst test data where the axial-to-hoop stress ratio is ½. As will be shown in the comparison of the different mechanical tests, the stress state is important in determining uniform elongation. This model applies only to cladding with circumferential hydrides and does not apply to cladding with radial hydrides or significant hydride blisters or spalling.

$$UE = \min(UE_0, UE_{Hex})$$

where:

UE = uniform plastic elongation, %

UE_0= 2.2%

$$UE_{Hex} = A \cdot H_{ex}^{-p} \qquad H_{ex}>0$$

$$UE_{Hex} = UE_0 \qquad H_{ex}=0$$

$$A = 1211 \exp(-0.00927 \cdot T) \qquad T<700K$$

$$A = 1.840803 \qquad T>700K$$

$$p = 1.355231 - 0.001783 \cdot T \qquad T<700K$$

$$p = 0.107131 \qquad T>700K$$

$$H_{ex} = \max(0, H_{Tot} - H_{Sol})$$

$$H_{Sol} = 1.2 \times 10^5 \exp\left(\frac{-8550}{1.985887 \cdot T}\right)$$

HTot = total hydrogen in cladding, ppm

T = temperature, K

The excess hydrogen calculated above is found using the steady-state hydrogen solubility as discussed in Section 2.3.4. The maximum predicted strain allowed by this model is 2.2% as fixed by the term, UE_0. This term has been selected as an average value of uniform elongation from specimens with no excess hydrogen.

The model for uniform elongation is not a function of fast neutron fluence. However, as the data that were used in model development are taken from in-reactor cladding specimens, there is somewhat of a correlation between hydrogen concentration and fast neutron fluence. Presented in Figure 3.18 is the hydrogen concentration data as a function of fast neutron fluence for the data in the Pacific Northwest National Laboratory (PNNL) database (Adamson et al. 1986, Averty et al. 2003, Balfour 1982a, Balfour 1982b, Berat et al. 2000, Billone, 2002, Chun et al. 1987, Desquines et al. 2005, Dideon and Bain 1983, Garde 1986, Garde 1989, Garde et al. 1996, Hardy 1970, Kemper and Zimmerman 1957, Kubo et al. 2010, Lowry 1981, Mahmood et al. 1997, Newman 1986, Newman 1990, Pettersson et al. 1979, Smalley 1971, Smith 1983, Smith 1994, Van Swan et al. 1997, Williams et al. 1974, Wisner and Adamson 1998, Yagnik et al 2005). It can be seen that as fluence increases, hydrogen content tends to increase as well. The best fit to uniform elongation data was found as a function of hydrogen content rather than fast neutron fluence. It should be noted that not all data with high fluence will have high hydrogen and vice-versa, because some mechanical specimens are artificially hydrogen-charged without being irradiated and others may be from a test reactor with low temperatures and, therefore, low corrosion and hydrogen.

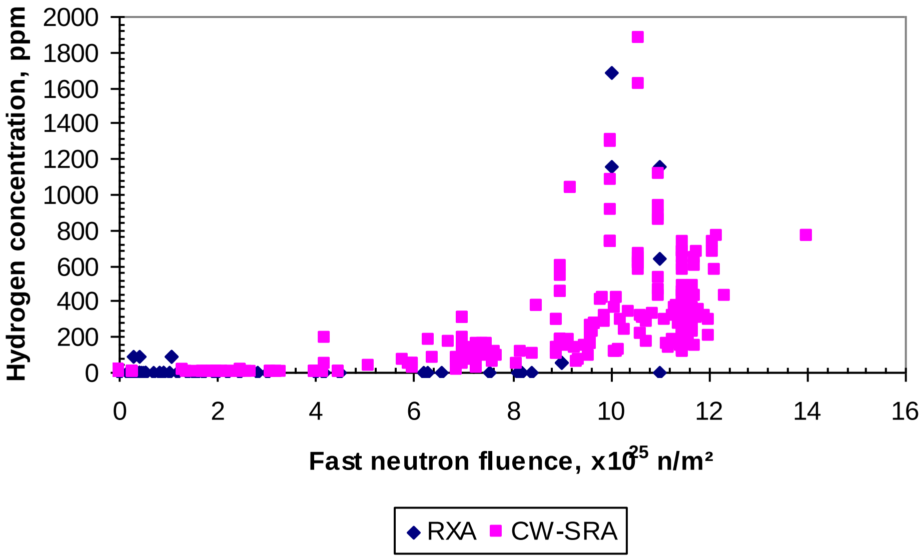

Figure 3.18. Hydrogen Concentration vs. Fast Neutron Fluence for the Data in the PNNL Database (293K≤T≤755K)

A correlation for total elongation has not been developed. It has been found that the level of scatter in the total elongation data is greater than the effect of temperature, hydrogen, or fast neutron fluence on total elongation. Additionally, PNNL has found that uniform elongation makes for a reasonable strain failure criteria for nuclear fuel rods under conditions of pellet-cladding mechanical interaction (biaxial stress state). If the modeling results predict strain beyond the uniform elongation, the rod is assumed to have failed.

3.4.2 Data Comparison

Figure 3.19 shows a plot of the predicted minus measured uniform elongation versus excess hydrogen for Zircaloy-4 cladding and some independent ZIRLO™ data (not used for model development). These data were taken at various temperatures and fast neutron fluence. This figure demonstrates that the strains from ring tests (hoop stress) are typically greater than those from axial tension tests and biaxial burst tests. It is for this reason that ring test data were not used to develop this model. This illustrates that stress state is important when determining ductility. The axial tensile test data were used for model development because of their close agreement with the biaxial burst tests. The DBTT for Zircaloy cladding with hydrides has also shown to be stress-state dependent (Kubo et al. 2010). The stress state during transportation is much more complex (combination of axial, radial, hoop and shear stresses) than the biaxial state of PCMI such that for transportation events that experience plastic deformation, the cladding ductility could be different than for the biaxial stress state. This is also true for the DBTT for fuel cladding during transportation, i.e., the DBTT may be different than for a biaxial stress state. However, there are no ductility data for irradiated Zircaloy that simulates the stress state during transportation. The bend tests to be performed at Oak Ridge National Laboratory (ORNL) on irradiated cladding with the fuel in place will give information on the cladding ductility and stress levels at failure. Therefore, the uniform elongation data from biaxial testing represent the closest to the stress state during transportation.

It is also noted that annealing of the cladding may occur during dry storage, particularly, if temperatures are at or above 320°C. Bourdiliau et al. (2010) has demonstrated that there is significant recovery of both uniform and total elongation with this annealing but even though the cladding yield strength can be reduced to that of unirradiated cladding, the cladding ductility remains lower than in the unirradiated condition. Bourdiliau et al. (2010) did not mention the hydrogen levels in their Zircaloy4samples that were annealed, it was mentioned that they were irradiated up to four cycles but did not mention if they were cut from fuel cladding.

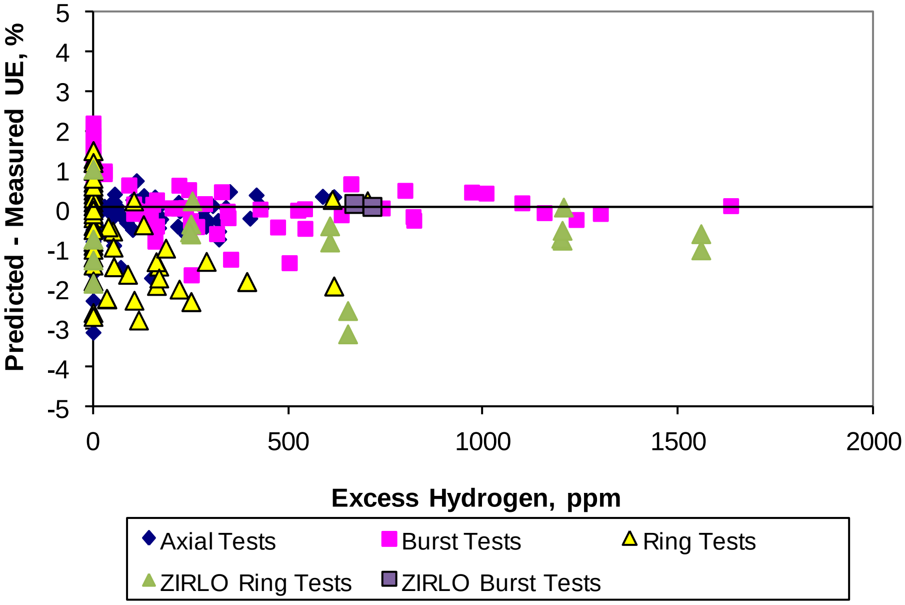

Figure 3.19. Predicted Minus Measured Uniform Elongation vs. Excess Hydrogen for Irradiated Data

3.4.3 Uncertainty

The standard error of the uniform elongation for the set of 236 irradiated cladding data is 0.9% strain because of the large uncertainty in samples with little irradiation. The distribution of the uncertainties for the irradiated data are shown in Figure 3.20**Error! Reference source not found.**. It should be emphasized that there may be some uncertainty because of the difference in the stress state between the biaxial test data used to development the model and the complex stress state for fuel cladding during transportation.

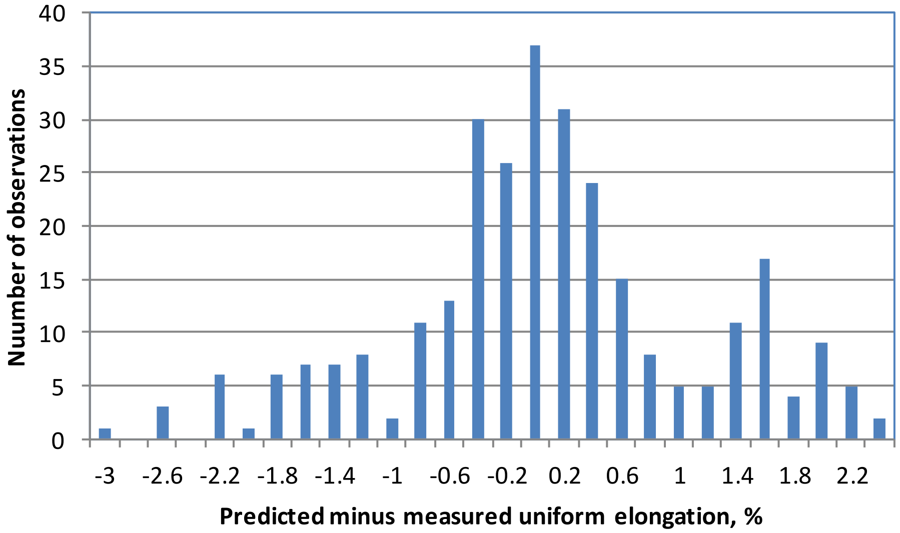

Figure 3.20. Distribution on Uncertainty for Uniform Elongation for Irradiated Data

3.5 Fracture Toughness

Fracture toughness data for Zircaloy-4 (Walker and Kass 1974, Kreyns et al. 1996, and Walker 1972) and Zircaloy-2 (Kreyns et al. 1996, Dubey et al. 1999, Huang and Mills 1993, Huang 1993, Attchison 1969, Coleman et al. 1989, Simpson and Chow 1987, Edsinger et al. 2000, Huang 1993 Mahmood et al. 1997) were collected from many sources and tabulated along with the corresponding test temperature, test method, crack orientation, fast neutron fluence, and average hydrogen concentration. These data were separated into four categories: Zircaloy-4 tested according to ASTM E399 (ASTM E399 1974), Zircaloy-2 tested according to ASTM E399, Zircaloy-2 tested according to ASTM E813 (ASTM E813 1989), and Zircaloy-2 tested by some other method. The data of the latter category is considered suspect and was not used in the model development. Since fracture toughness is an empirical measurement, it is important that the same empirical measurement technique is used for each data set. Note that fracture toughness may be stress-state-dependent similar to the ductility and DBTT data, and the tests described above do not simulate the complex cladding stress state during transportation.

It should be noted that all the Zircaloy-4 data and much of the Zircaloy-2 data came from rods that were uniformly charged with hydrogen either before or after irradiation. There was some Zircaloy-2 data that were as-measured hydrogen from in-reactor operation, but all these data were from Zircaloy-2 pressure tubes, which showed a relatively uniform distribution of hydrides. It is known that for high burnup fuel rods, the hydrogen concentration in the outer rim of the cladding tubes is much higher than in the inner part. This heavily hydrided rim may cause the fracture toughness to be lower than a similar cladding tube with the same average hydrogen content in a uniform concentration distribution. Fracture toughness tests need to be done on high burnup fuel rod cladding with the fuel in place. This simulates the stress state during transportation in order to determine the effect of a heavily hydrided rim. ORNL is preparing to perform these types of tests on high burnup cladding with the fuel in place. These data can be used to add a correction to this model for hydrogen distributions in high burnup cladding.

In contrast to the effects of hydrides decreasing fracture toughness, the annealing of irradiation defects during long-term storage above 320°C may increase the fracture toughness from the irradiated condition. This illustrates the need to perform sensitivity analyses using a range of fracture toughness values.

In this section, a fracture toughness model for cracks in the circumferential-longitudinal (CL) direction is presented based on irradiated and unirradiated data. This correlation may be used to determine if facture is likely because of impact loading that may be experienced under NCT. If the modeling and sensitivity analyses show that the impact loads are close to the values in this model, it may necessary to develop a more prototypic model based on the ORNL fracture tests.

Some success has been experienced in modeling the cladding as a composite material with a brittle (very low fracture toughness) hydride rim and a higher fracture toughness for the interior of the cladding wall below the rim to predict in-reactor failures because of PCMI (Udagawa et al. 2011). This modeling is fairly complex and not within the limited scope and funding of this effort.

3.5.1 Model

The final form of the fracture toughness model for Zircaloy with cracks in the CL direction is given below:

$$K_{IC} = (-5.8699 \cdot \ln(H^*) + 56.893)\left(1 + \frac{T-20}{250} \cdot 0.1\right)$$

where:

K_{IC} = Fracture toughness of Zircaloy in the CL direction, MPa-m1/2

H* = Excess hydrogen concentration = max(0.1,min(11517,C_H-H_{sol}))

C_H = Average hydrogen concentration, ppm wt. (if hydrogen is deuterium, use 0.5*C_H)

H_{sol} = Hydrogen solubility given by Kearns (1967)

= $1.2 \times 10^5 \exp\{-8550/[R(T+273.15)]\}$

R = gas constant = 1.99 kcal/(gmol – K)

T = temperature, °C

3.5.2 Data Comparison

Figure 3.21 shows a plot of the predicted versus measured fracture toughness for Zircaloy-4 cladding, Zircaloy-2 cladding and Zr-2.5Nb pressure tubes. These data were taken at various temperatures hydrogen levels, and fast neutron fluence. It can be seen that for high values of measured fracture toughness the model under-predicts the data. Above around 40 MPa-m$^{0.5}$ the K_{IC} value is not particularly relevant to irradiated cladding with hydrogen as the material is quite ductile and will fail by some other mechanism before failing by some other mechanism.

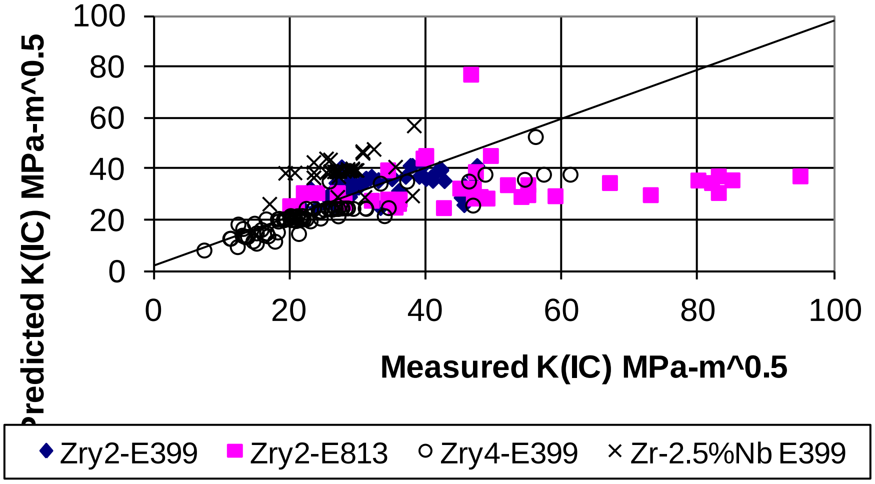

Figure 3.21. Predicted vs. Measured Fracture Toughness Data

3.5.3 Uncertainty

The standard error of this correlation is 12 MPa-m$^{0.5}$. The distribution of the uncertainties for the irradiated data is shown in Figure 3.22.

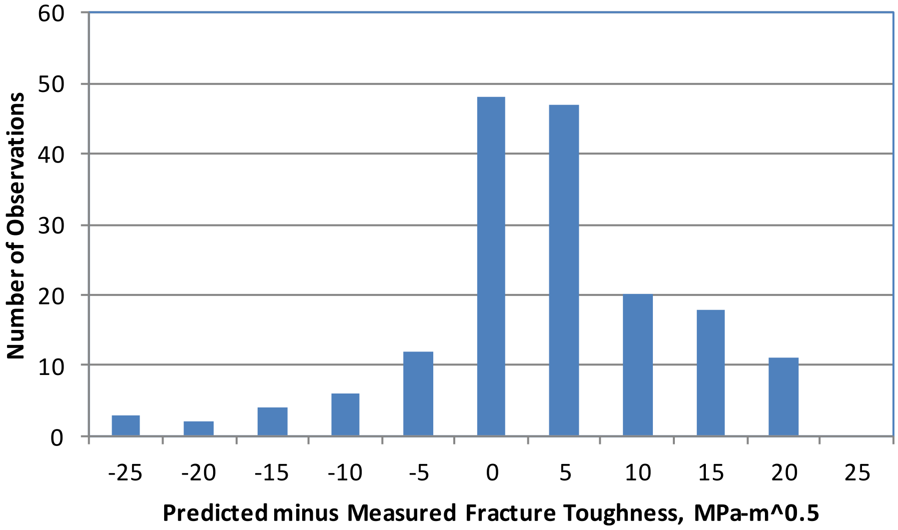

Figure 3.22. Distribution on Uncertainty for Fracture Toughness Data

3.6 Fatigue

Fatigue design basis curves have been developed by O'Donnell and Langer (1964) for irradiated Zircaloy components. Although other curves have been proposed, this curve has continually been selected by fuel vendors for their fatigue analysis of fuel rods in-reactor and has been approved by the U.S. Nuclear Regulatory Commission (NRC, Standard Review Plan Section 4.2). Figure 3.23 shows this curve which is applicable between room temperature and 600°F (326°C). Appropriate conservative safety factors were applied by the authors in the development of this curve. It should be noted that the fatigue tests of irradiated Zircaloy specimens used to derive these curves had very little hydrogen and no hydride rim. The conservatism in the fatigue curves may cover the effect of hydrides but this is unknown at this time. Therefore, the uncertainty in the fatigue curve in Figure 3.23 should be considered to be high.

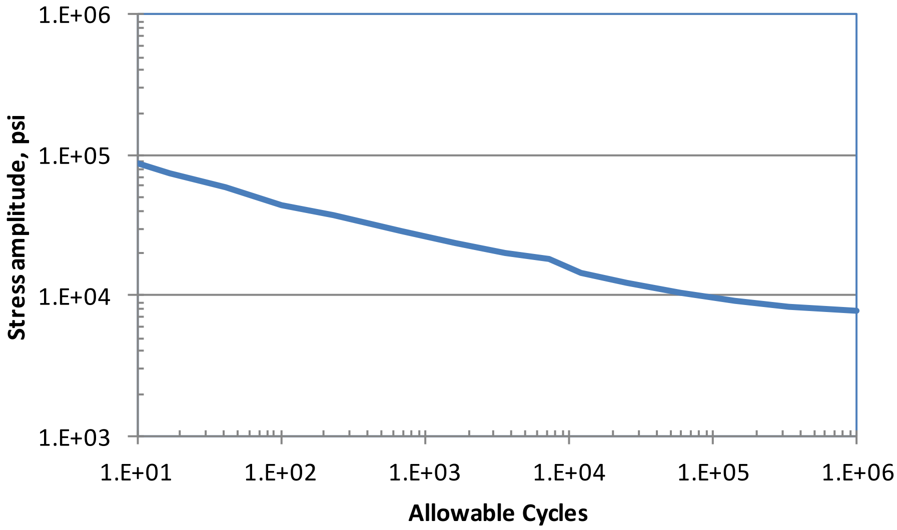

Figure 3.23. O'Donnell Fatigue-Design Curve for Irradiated Zircaloy from Room Temperature to 600°F (316°C)

This fatigue curve represents the most promising failure criterion for fuel rods under NCT. This is the curve that is most often used by the fuel vendors to perform their fatigue analysis for their in-reactor safety analyses. It is noted that although the data used to develop these fatigue limits are taken on irradiated samples under several different stress conditions, the samples are from plates rather than tubes, and there was no hydrogen in the samples, as would be expected in cladding tubes. However, it is expected that this fatigue curve will be generally representative of the behavior of cladding from spent fuel with low hydrogen levels. As initial stress intensities and expected stress cycles are calculated from the modeling task, this fatigue curve should be used to assess the potential for failure. If this modeling with sensitivity analyses shows stress cycling far from the fatigue failure limit in Figure 3.23 then the uncertainty in the fatigue limits will be of a lesser concern. In addition, fracture testing performed by ORNL under prototypic loading and frequencies that will provide adequate demonstration on the conservatism in Figure 3.23 and that the rods will not fail. If the modeling results show stress cycling near this failure curve then further experimental work should be performed to produce a more prototypic failure fatigue curve based on the ORNL testing of high burnup fuel rods.

4. FUEL PROPERTIES

This section describes the fuel properties that will be necessary for modeling the fuel assemblies. Sections are included describing models for the elastic modulus of the fuel and the fracture strength of the fuel. A section that describes the nature of the fuel/clad bonding layer is also included. Most of these models come from MATPRO as FRAPCON and FRAPTRAN and do not consider the impact of the strength of the pellet because it is much greater than that of the cladding. Comparisons of model predictions to data are provided with irradiated data shown separately from unirradiated data. As appropriate, the calculated uncertainty and the distribution on that uncertainty are provided. The UO_2 fuel pellets are pictured in the inset of Figure 4.1.

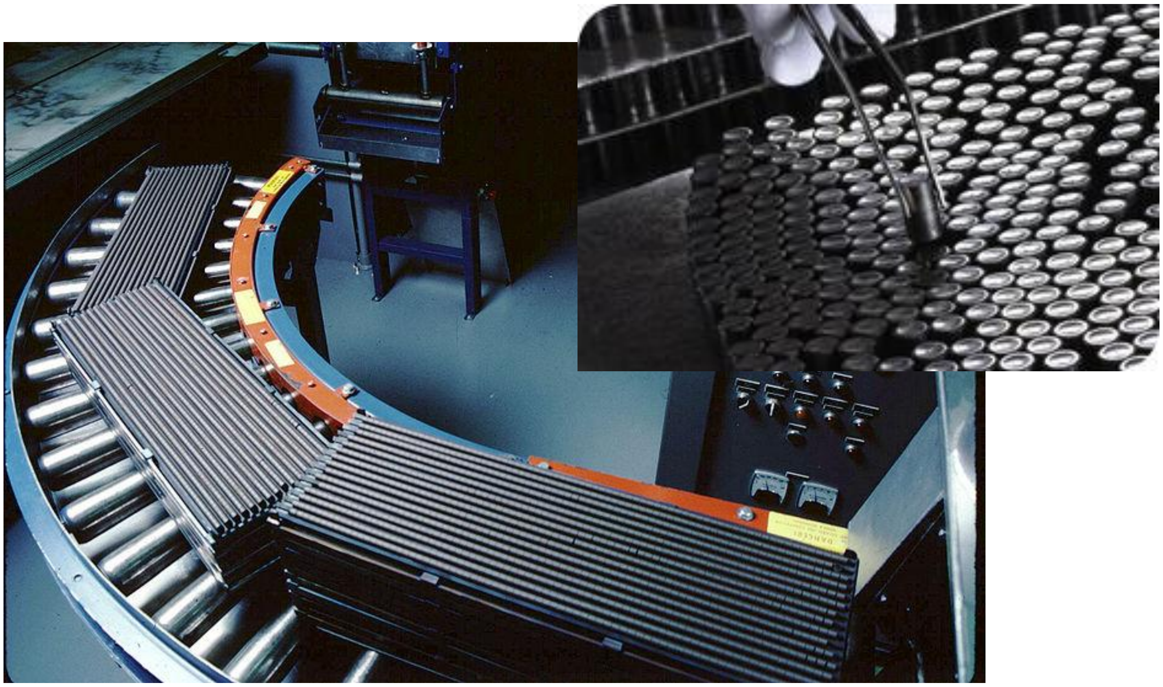

Figure 4.1. UO_2 Fuel Pellets

4.1 Elastic Modulus

4.1.1 Model

The model used in MATPRO for Elastic Modulus is given by:

$$E = 2.334 \times 10^{11}\left(1 - 2.752\left(1 - D\right)\right)\left(1 - 1.0915 \times 10^{-4} T\right)$$

where:

E = Elastic modulus for UO_2 fuel (Pa)

D = fuel density (fraction of theoretical density)

T = temperature (K)

Laux et al. (2012) presented data from both Simfuel and irradiated fuel that show the modulus goes down about 25% between 0 and 100 GWd/MTU. A linear regression using the value from MAPTRO at 0 GWd/MTU revealed a better fit if the modulus goes down 20% between 0 and 100 GWd/MTU for the Laux et al. (2012) data. Therefore, the equation from MATPRO shown above should be modified and the equation below should be used.

$$E = 2.334 \times 10^{11} \left(1 - 2.752\left(1 - D\right)\right)\left(1 - 1.0915 \times 10^{-4} T\right)\left(1 - 2.0 \times 10^{-3} Bu\right)$$

where

Bu = Burnup (GWd/MTU)

4.1.2 Data Comparison

Figure 4.2 shows a plot of the predicted and measured Elastic Modulus for unirradiated UO_2 fuel. These data were taken at various temperatures and densities. Figure 4.3 shows a plot of the predicted and measured Elastic modulus for SimFuel and irradiated UO_2 fuel. These data were taken at room temperature on pellets of approximately 95% theoretical density. The SimFuel data were not used for model development. Figure 4.4 shows a plot of all Elastic modulus data and the corresponding 2-σ upper and lower bounds.

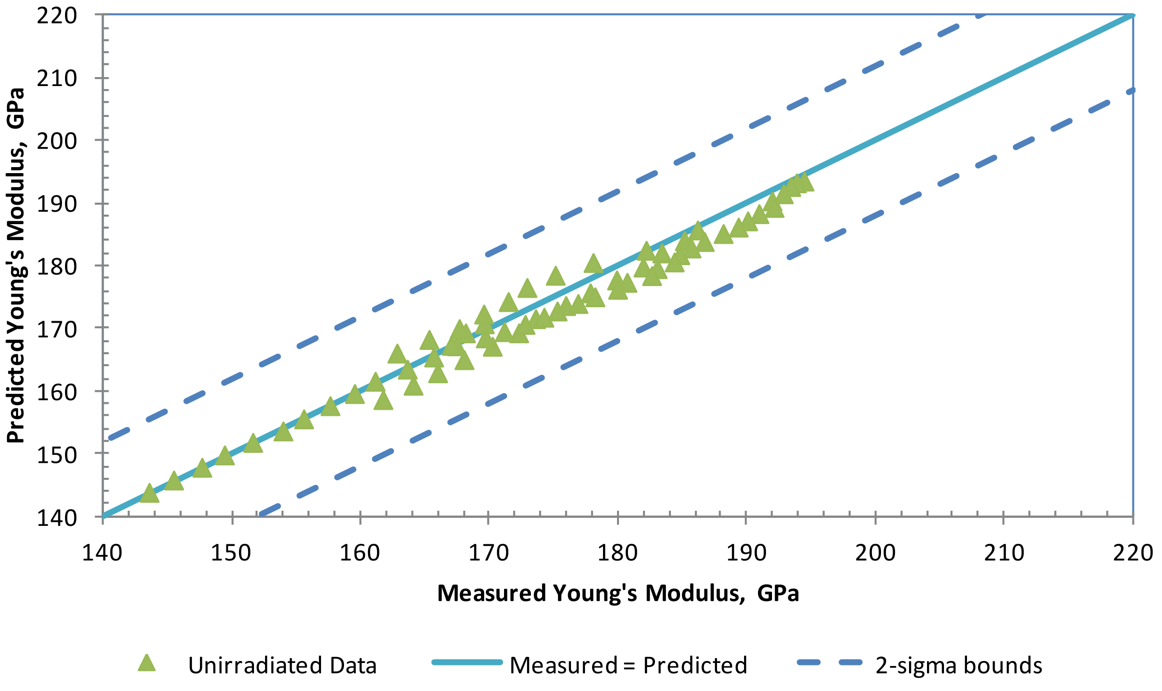

Figure 4.2. Predicted vs. Measured Elastic Modulus for Unirradiated Data

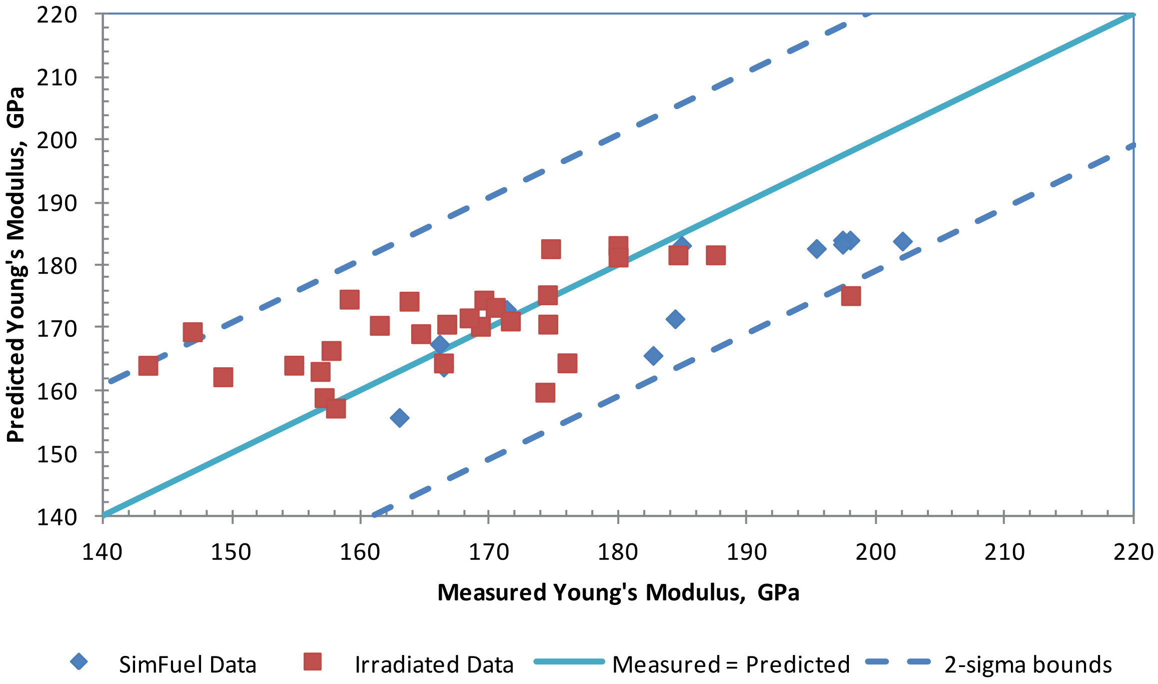

Figure 4.3. Predicted vs. Measured Elastic Modulus for SimFuel and Irradiated Data

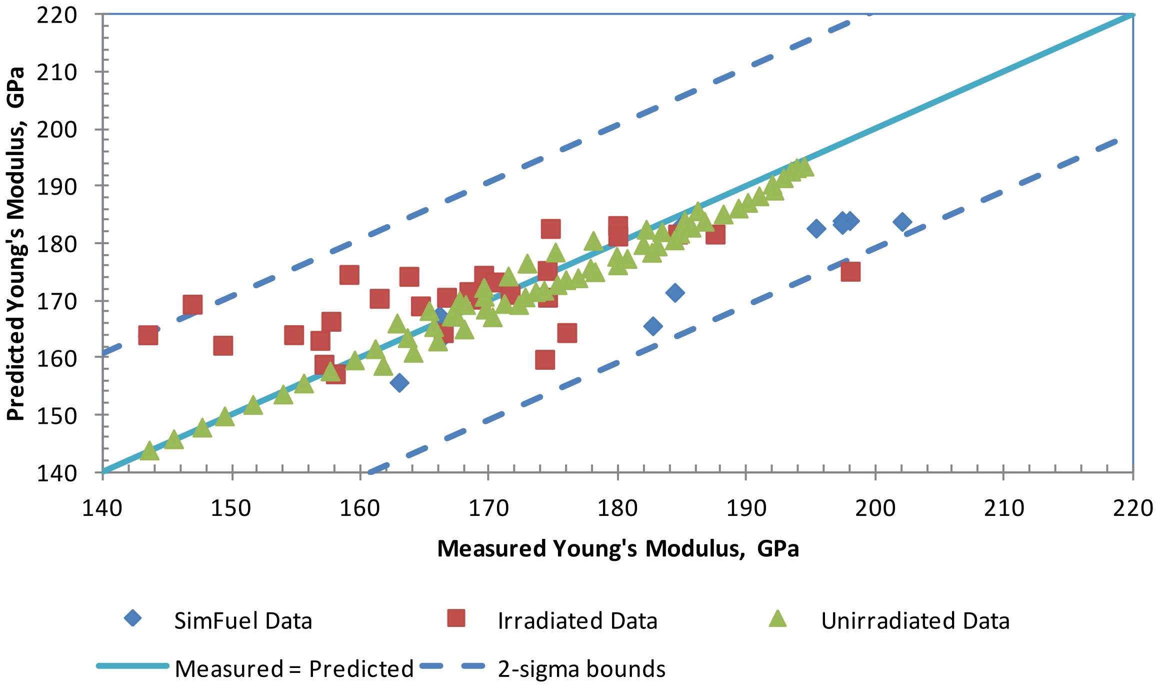

Figure 4.4. Predicted vs. Measured Elastic Modulus for Unirradiated, SimFuel, and Irradiated Data

4.1.3 Uncertainty

The standard error of the correlation for unirradiated UO_2 fuel is 6 $x10^9$ Pa.

The standard error of the correlation for irradiated UO_2 fuel is 10.5 $x10^9$ Pa.

An overall standard error for the correlation for irradiated UO_2 fuel should use the bounding value of 10.5 x 10^9 Pa. Figure 4.5 and Figure 4.6 show the distribution of the uncertainty for unirradiated and irradiated data.

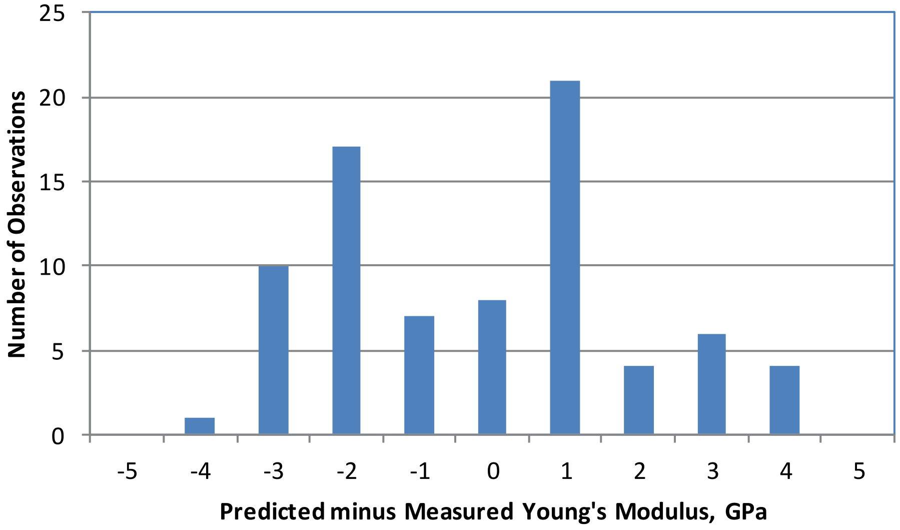

Figure 4.5. Distribution on Uncertainty for Elastic Modulus for Unirradiated Fuel Data

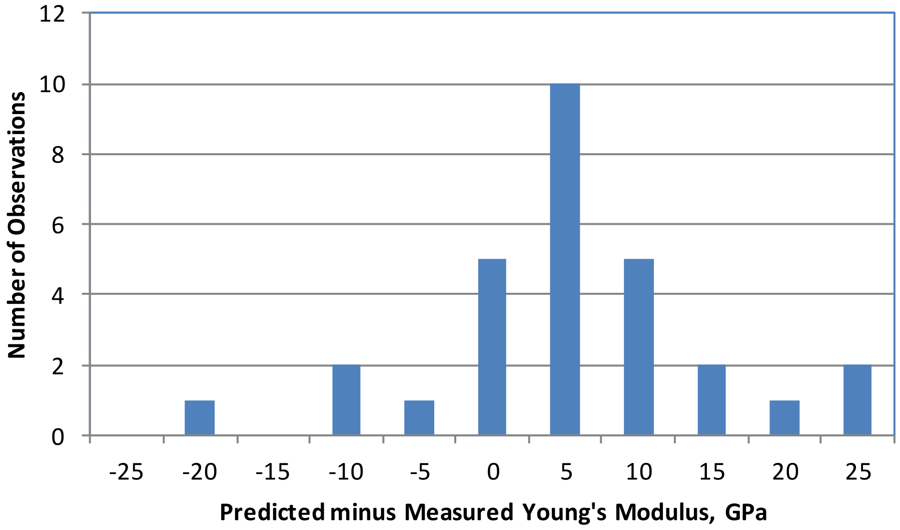

Figure 4.6. Distribution on Uncertainty for Elastic Modulus for Irradiated Data

4.2 Fracture Strength

4.2.1 Model

The model used in MATPRO for fracture strength is given by:

$$\sigma_F = 1.7 \times 10^8 \left(1 - 2.62\left(1 - D\right)\right)^{\frac{1}{2}} \exp\left(\frac{-1590}{8.314 \cdot T}\right)$$

where:

σ_F = fracture strength for UO_2 fuel (Pa)

D = fuel density (fraction of theoretical density)

T = temperature (K)

This model is valid up to 1000 K. Above 1000 K, the fracture strength evaluated at 1000 K should be used.

4.2.2 Data Comparison

Figure 4.7 shows a plot of the fracture strength model as a function of temperature for UO_2 fuel 95% theoretical density. Also shown in this figure are the unirradiated data used in the development of this correlation. The data have been adjusted to 95% theoretical density using the correlation above. It can be seen that there is significant scatter in these data. Also shown in this figure are the upper and lower 2-σ bounds for this model.

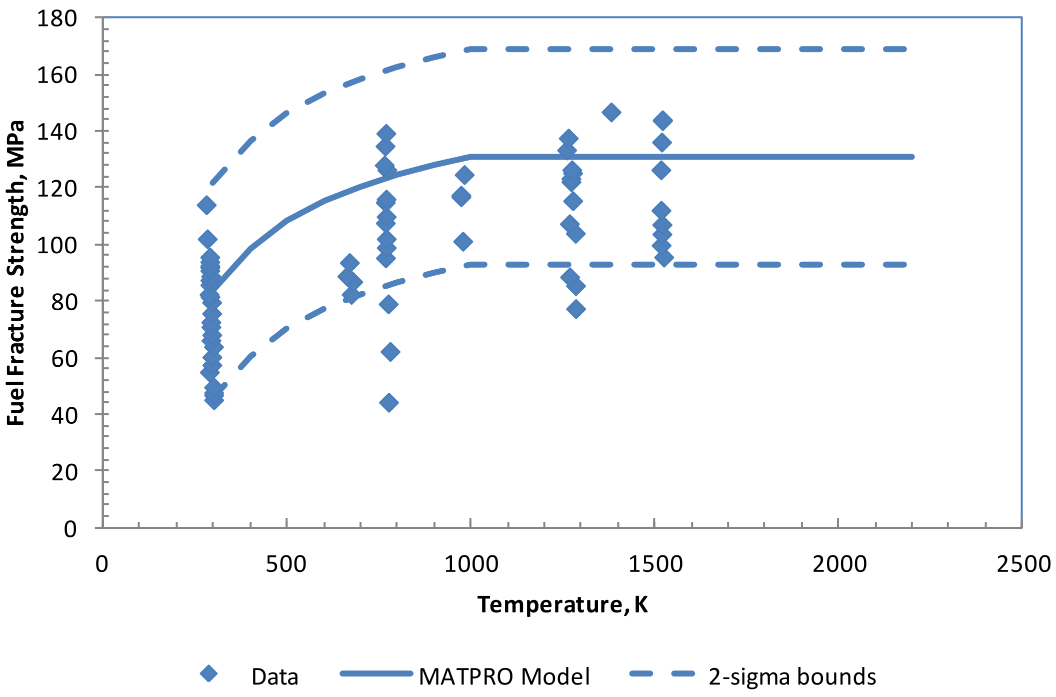

Figure 4.7. Fracture Strength Model in MATPRO and Data Used in Model Development

4.2.3 Uncertainty

The standard error of this correlation is 1.9×10^7 Pa.

It was not possible to create a distribution of the data uncertainty for this model. The data are only available in graphical form and there is significant overlap of the data points. This makes it difficult to accurately assess the distribution of the data uncertainty.

4.3 Fuel/Clad Bonding Layer

A fuel cladding bond between the cladding inner surface and pellet outer surface has been observed in several instances by examining cross sections of fuel rods irradiated at various power and burnup levels. This fuel cladding bond may have an impact on the mechanical response of the fuel rod during NCT. In high burnup fuel (>55 GWd/MTU) where bonding is present around the circumference of the fuel-cladding interface at the majority of the fuel rod length (bond not present at fuel rod ends) there is essentially no fuel clad gap during in-reactor operation. However, this is not completely the case for used fuel during storage and transportation because there will be circumferentially cracking in the rim region of the fuel that is just inward from the fuel-cladding bond. This narrow circumferential cracking in the fuel is because of cool down of the fuel from reactor operation, i.e., fuel is hotter than cladding during in-reactor operation such that difference in fuel and cladding expansion from hot to cold results in cracks.

An example of the narrow circumferential cracking (crack width less than 2 µm) near the fuel cladding bond is shown in a cross section micrograph in Figure 4.8 that is taken from Kim (2010). The micrograph was taken near a mid-axial location of a PWR fuel rod irradiated to 53 GWd/MTU. Note that there was complete bounding around the circumference of this rod. This circumferential cracking means that the fuel and cladding will not be as strongly connected as is the case during in-reactor operation, however, the fuel-cladding bond appears to be relatively fracture-resistant (compared to the fuel) because cracking results in the fuel and not the bond in the cooled fuel at discharge.

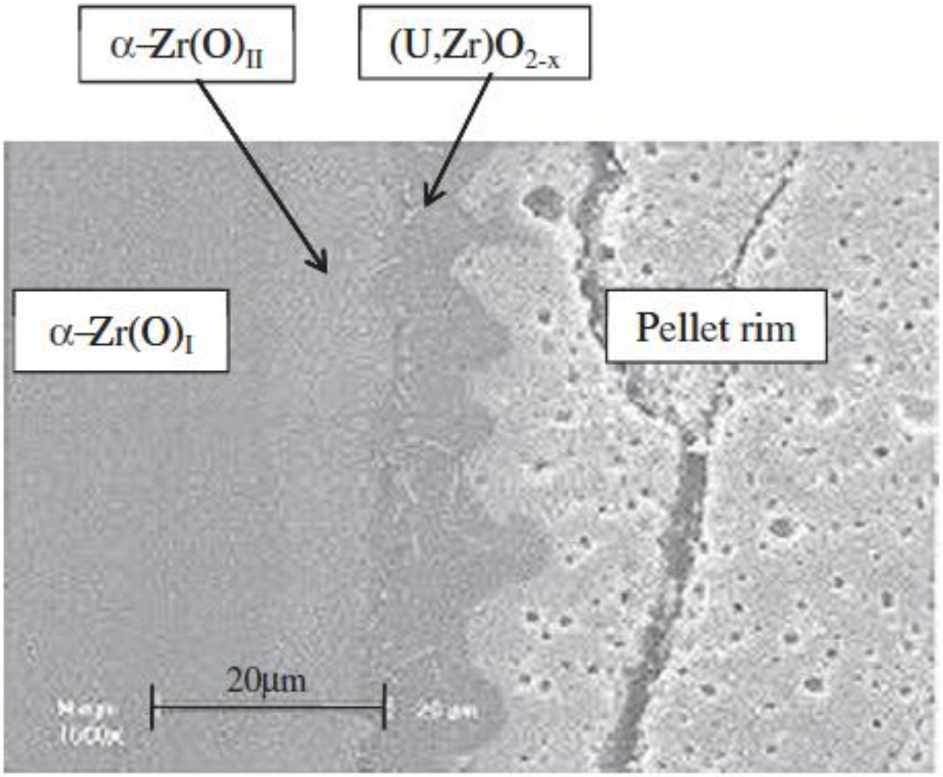

Figure 4.8. Micrograph Taken from Kim 2010 of Fuel-Cladding Bond Region at Mid-axial Position in a PWR Fuel Rod at 53 GWd/MTU Burnup

The bonding layer itself appears to be similar between boiling water reactors (BWRs) and PWRs, but the power and burnup level that fuel cladding bonding starts and that complete circumferential bonding is experienced will most likely be different between BWRs and PWRs.

4.3.1 Boiling Water Reactors

Nokita and Une (1997) have estimated the rod power and burnup combinations from steady-state operation where partial bonding begins and full bonding is experienced for a BWR fuel design in Figure 4.9. These authors reported a bonding layer of 10 to 20 µm that appears to increase with burnup up to the maximum burnup examined of 42 GWd/MTU. The partial bonding is where a bond is present at specific circumferential locations but is not present at all circumferential locations. A similar relationship has not been found for PWRs but there are references that mention when bonding begins in a PWR fuel design. The bonding layer consists of three different phases two phases of ZrO_2 and $(U,Zr)O_2$ that both have cubic structure and an amorphous $(U,Zr)O_{2-x}$ phase. It appears that the ZrO_2 phase develops early in the initial fuel clad contact because it is observed on the inner cladding surface of low burnup fuel rods.

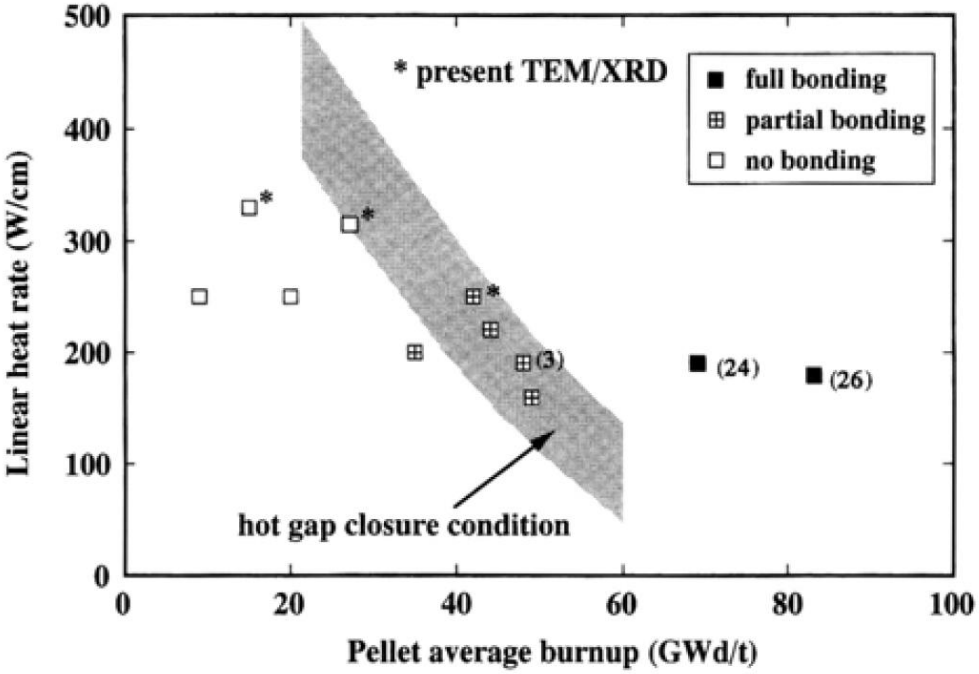

Figure 4.9. Relationship between Extent of Fuel-Cladding Bonding Layer and Rod Power and Burnup for a BWR Fuel Rod (Taken from Nogita and Une 1997)

4.3.2 Pressurized Water Reactors

Berghe et al. (2004) has observed pellet cladding bonding in PWR fuel rods subjected to high linear rod powers between 220 to 320 w/cm with burnups around 23 GWd/MTU. Micrographs revealed that bonding occurred in roughly 50% of the fuel rod surface with circumferential cracking in the rim similar to that observed by both Kim (2010) for a PWR and Nokita and Une (1997) for a BWR fuel rod. The maximum thickness of the bonding layer was approximately 10 µm. There was a difference in the composition of the bonding layer with cesium present that was not seen by Kim for a PWR or by Nogita and Une in a BWR rod. On top of the ZrO_2 layer was a Cs-Zr-O phase followed by a Cs-U-Zr-O phase. The presence of cesium is most likely from the higher linear heating rates of the fuel rod because it is known that cesium is released at similar temperatures as fission gas release is experienced. The Kim (2010) PWR and Nogita and Une (1997) BWR fuel rods did not see the high rod powers as those rods examined by Berghe et al. (2004) and, therefore, much lower release.

The chemical structure of the fuel-cladding bond appears to be the same in PWR and BWR fuel rods even though the burnup at which the bond occurs is most likely different. As noted in Figure 4.8, going from left to right: the $\alpha - Zr(O)_I$ is the metal cladding rich in oxygen (supplied by the pellet), the $\alpha - Zr(O)_{II}$ appears to be ZrO_{2+x}, while the next phase is $(U,Zr)O_{2-x}$, followed by the rim of UO_2 pellet, which is most likely deficient in oxygen (2-X). Kim (2010) has suggested that this rim may be UO_2 + U. The circumferential crack is within the fuel rim region. The maximum width of the $U,Zr)O_{2-x}$ phase while the combined $\alpha - Zr(O)_{II} + U,Zr)O_{2-x}$ phase is approximately 20 µm.

A paper by Sercombe et al. (2012) discussed a burnup-dependent, fuel-pellet-clad friction coefficient based on in-reactor power ramp tests (maximum linear powers range from 400 to 530 w/cm) on PWR fuel rods with burnups between 25 to 60 GWd/MTU. This paper has assumed that increased pellet cracking with burnup is primarily because of the friction coefficient between the fuel and cladding, therefore, the paper concludes that the friction coefficient increases with burnup as shown in Figure 4.10. The issue with this assumption is that fuel cracking has been shown to be also influenced by the increased precipitation of fission gas bubbles at high pressures on the grain boundaries with increasing burnup, this is known to decrease the strength of the grain boundaries resulting in fuel cracking along the grain boundaries. This has also been hypothesized as the reason for the increased fuel cracking with burnup.

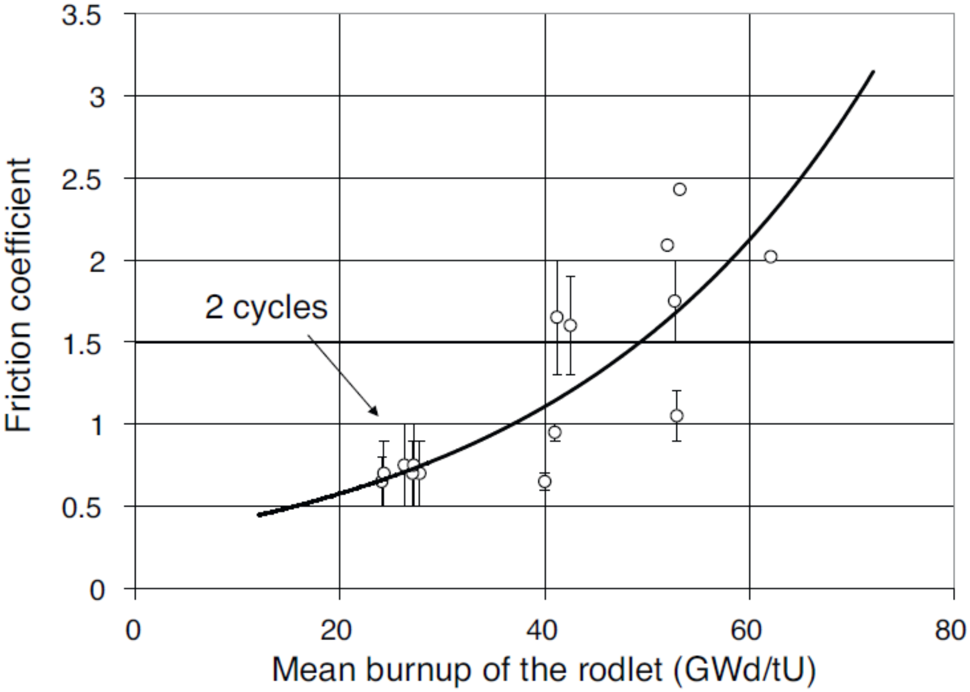

Figure 4.10. Calculated Coulomb Friction Coefficient from Power Ramping Fuel Rods at Various Burnup Levels Assuming That Pellet Cracking is Primarily Because of the Stresses Induced by Fuel Cladding Friction

The coefficient of friction versus burnup form this paper should not be used for used fuel for three reasons; 1) the circumferential cracking of the pellet on cooling in used fuel will change the friction coefficient from that at operating conditions in-reactor during a power ramp, 2) the contact pressure between the fuel-cladding will be significantly less than for power ramped rod, and 3) the increased cracking with burnup may also be due to increased fission gas bubbles on grain boundaries. The cool down difference in fuel-clad diametral gap between in-reactor versus ex-reactor uniform temperature will be on the order of 0.0006 to 0.0011 inches. However, this cracking is irregular in shape such that the fuel will not be sliding between two flat fuel surfaces. This cracking will allow the cladding to be compressed radially by an amount less than the residual crack gap because the fuel cracks will not be completely compressed into a whole non-cracked (solid) pellet, particularly at the low fuel temperatures for transportation.

Ex-reactor experiments of the coulomb friction coefficient between unirradiated cladding and fuel without cracks have shown a friction coefficient between 0.4 to 0.7 at low contact forces with cladding stresses in the elastic region Brouchard et al 2001. It is judged that this data is the most applicable to normal transportation at low burnups because the contact forces between the cladding and fuel will be low with some fuel cracking present, the biggest difference is that these out-of-reactor tests have no fuel-clad bonding and no fuel cracks typical of high burnup fuel. Therefore, it should be assumed that the coulomb friction coefficient is somewhere between 0.5 to 1.5 for used fuel.

From Figure 4.9 and analyses performed with the FRAPCON-3.4 fuel performance code when the fuel-cladding gap is closed, it appears that full bonding will be present in BWR rods at burnups above 55 to 60 GWd/MTU. As noted earlier there is not as much publicly available data on bonding for PWR fuel rods but we can make an estimate based on FRAPCON-3.4 analyses of when the gap is closed. At equivalent power levels, the fuel-cladding gap in a 17x17 PWR fuel rod with a 0.0065-inch gap closes between 7 to 12 GWd/MTU sooner than for a 10x10 BWR fuel rod with a similar gap. Therefore, the curve presented in Figure 4.9 will be shifted to the left by 7 to 12 GWd/MTU for a PWR.

4.3.3 Summary

One of the largest gaps in the fuel properties is the strength of the fuel/clad bonding layer. This parameter is a very difficult quantity to measure directly. However, sensitivity studies may be performed under the modeling task to determine the impact, if any, of the fuel clad bonding layer strength on the response of the fuel to NCT. The coulomb friction coefficient between the fuel-cladding should be assumed to range from 0.5 to 1.5.

5. GRID MATERIAL PROPERTIES

As seen in Table 2.2, the grids may be made of either Zircaloy-4 or Inconel-718. This section will provide a discussion on how the Zircaloy-4 cladding properties may be used for Zircaloy-4 grids. For example, the expected fast neutron fluence, corrosion thickness, and hydrogen content for Zircaloy-4 grids will be given. Figure 5.1 shows a close-up of the fuel assembly grid spacers.

For Inconel-718, the basic mechanical properties as a function of temperature will be provided for unirradiated sheet. The properties of Inconel-718 will likely change with irradiation, but no data is currently available for irradiated Inconel-718.

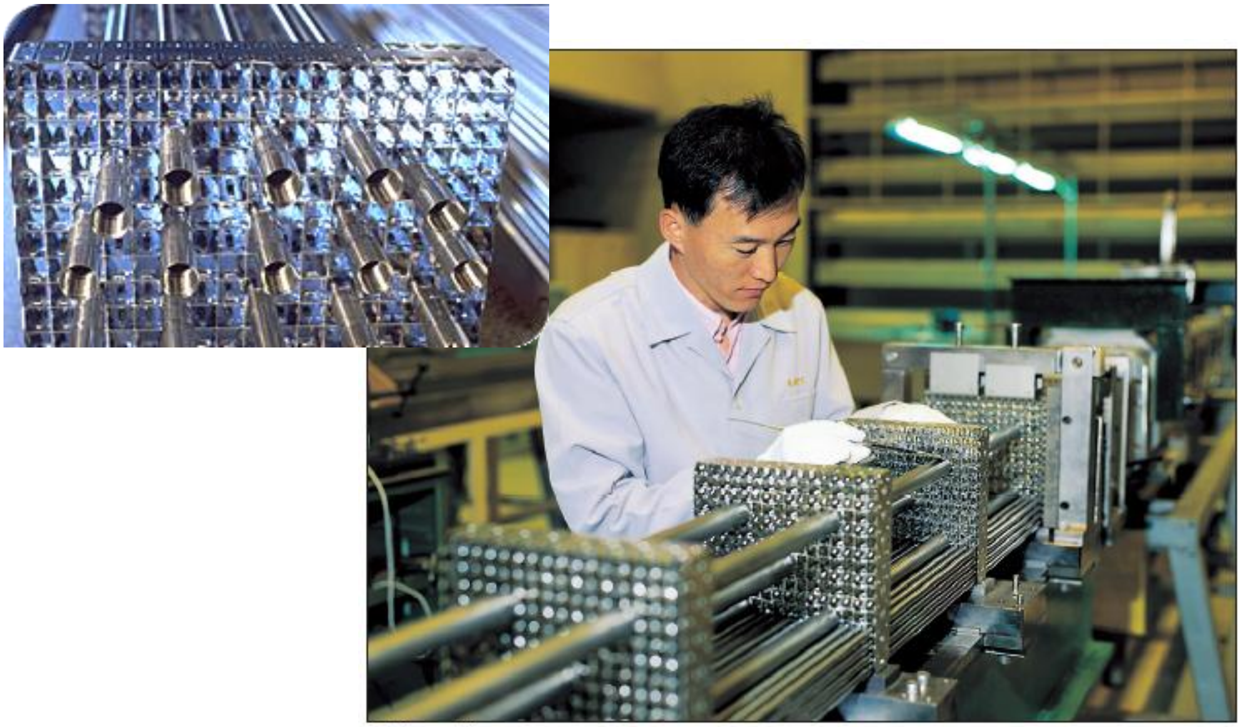

Fuel assembling process

Figure 5.1. Assembly Grid Spacers

The biggest issue with the grids is the force with which the spring in the grid contacts the fuel rod. The geometry of this situation is shown in Figure 5.2. The design of these springs and dimples varies significantly from assembly to assembly between vendors and even for a single vendor from year to year as the design evolves. There is complete relaxation of the Zircaloy spacer springs after the first cycle of operation while Inconel spacer springs retain approximately 10 to 15% of their original force at discharge. In order to assess the importance of these springs on the response of the assembly, each spring will be modeled as a simple spring and sensitivity studies will be performed to evaluate the importance of the properties of these springs. This study will reveal if further testing is required on the irradiated grids in order to better model the response of the assembly to NCT.

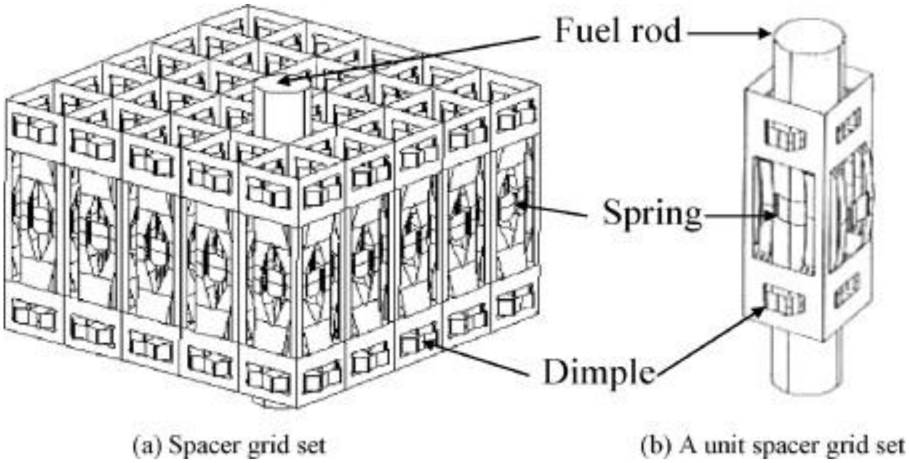

Figure 5.2. Typical Grid with Springs and Dimples to Retain the Fuel Rods

5.1 Zircaloy Grids

The Zircaloy-4 mechanical properties models from Section 3.0 may be used to model Zircaloy-4 grids. The microstructure and texture of drawn tubes is very similar to that of cold rolled sheet. Typically the properties of these are assumed to be the same. The grids are typically made from cold rolled Zircaloy-4 material and a cold work fraction of 0.5 should be assumed. The grids should have been exposed to the same fast neutron fluence the cladding was exposed to at the same elevation. The level of corrosion and hydrogen in the grids are different from that on the fuel rods at similar elevations.

Garcia-Infanta et al. (2010) has measured oxide thickness in PWR ZIRLO spacer grids and guide tubes as a function of axial elevation in a fuel assembly with an average burnup of 54 GWd/MTU in Figure 5.3. This figure demonstrates that oxide thickness increases with axial elevation (due to increase in coolant temperatures with elevation) with the greatest oxidation at grid strap welds.

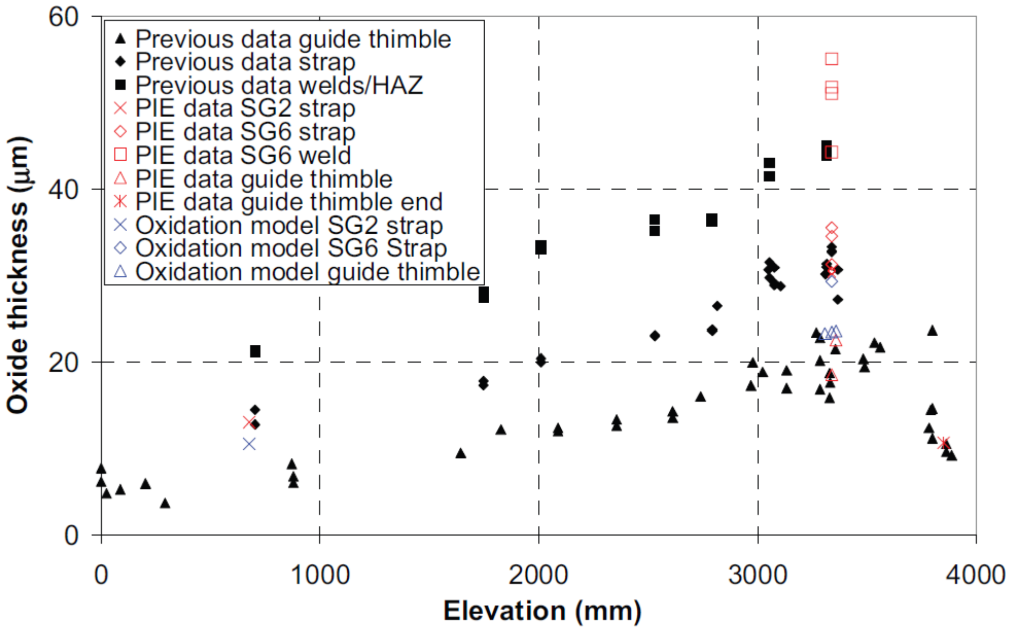

Figure 5.3. Corrosion Thickness in ZIRLO Grid Straps and Guide Tubes at Different Axial Locations in an Assembly with Approximately 54 GWd/MTU Average Burnup

The hydrogen in the PWR spacer grids and guide tubes is also plotted as a function of axial location in Figure 5.4 that demonstrates maximum levels at the same location as for the oxide. This paper has also provided micrographs that demonstrate the hydride has a relatively uniform distribution for these structural components (due to almost no thermal gradients) as opposed to the strong hydride gradients in the fuel cladding wall. The hydrides in the grid straps are primarily in the direction of the cold work while hydrides within the grid strap welds are very random (grains are recrystallized). The guide tubes have a random distribution at the axial location with maximum hydrogen.

These figures may be used to estimate the level of corrosion and hydrogen in Zircaloy-4 grid material at high-burnup at various axial elevations.

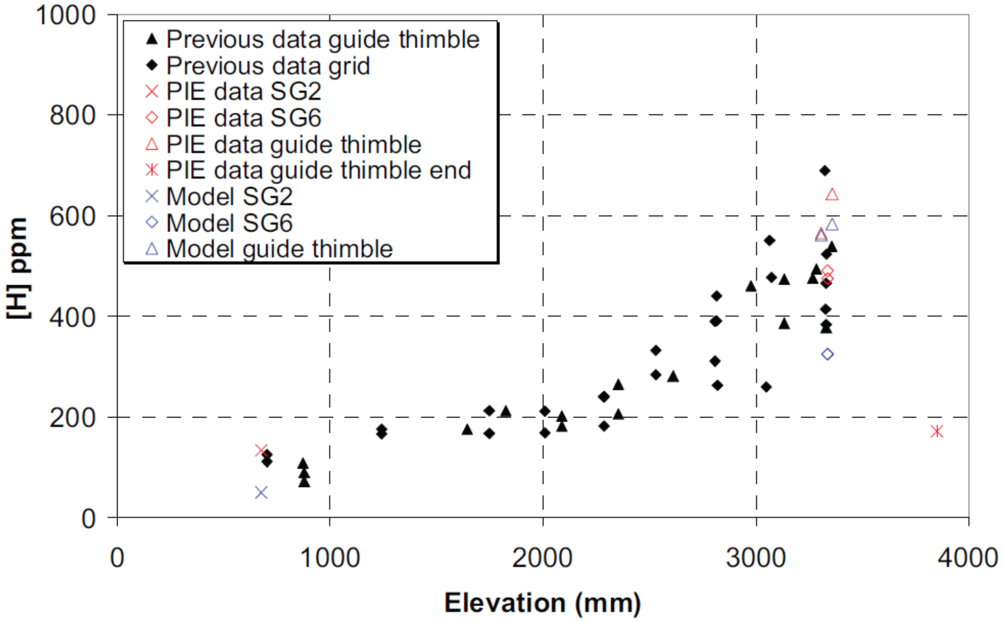

Figure 5.4. Hydrogen Concentrations in ZIRLO Grid Straps and Guide Tubes at Different Axial Locations in an Assembly with Approximately 54 GWd/MTU Average Burnup

5.2 Inconel 718 Grids

Hydrogen is not expected to be picked up in a significant quantity in Inconel 718. Because the properties shown here are for unirradiated sheet material, the uncertainty in these property correlations is low relative to that of the cladding correlations. The uncertainty in how irradiation will impact these properties is a much greater uncertainty (Special Metals Corporation. 2000).

5.2.1 Elastic and Bulk Moduli

The elastic and bulk moduli of Inconel 718 over a temperature range of 295 K to 700 K can be approximated with the linear correlations given below.

$$E = 212.81 - 0.0495\ T$$

$$G = 82.637 - 0.0181\ T$$

where:

E = elastic modulus, GPa

G = bulk modulus, GPa

T = temperature, K

These correlations are shown below in Figure 5.5.

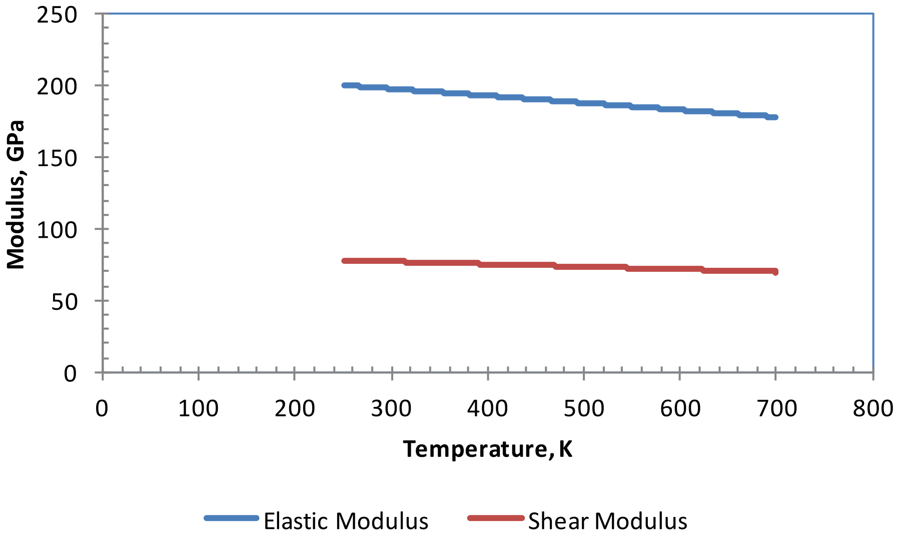

Figure 5.5. Elastic and Bulk Moduli for Inconel 718

5.2.2 Yield Stress

The yield stress (YS) of Inconel 718 Grids is a strong function of the final heat treatment. Cold-rolled sheet that was annealed has a lower yield stress than a sheet that was not annealed following cold rolling.

The yield stress can be modeled for Inconel 718 sheet with and without final anneal using the equations below as a function of temperature.

$$YS_{CR} = 1491.1 - 0.42\ T$$

$$YS_{CR-A} = 1251.7 - 0.4343\ T$$

where:

YSCR = yield stress of cold rolled sheet, MPa

YSCR-A = yield stress of cold rolled and annealed sheet, MPa

T = temperature, K

These correlations are shown below in Figure 5.6.

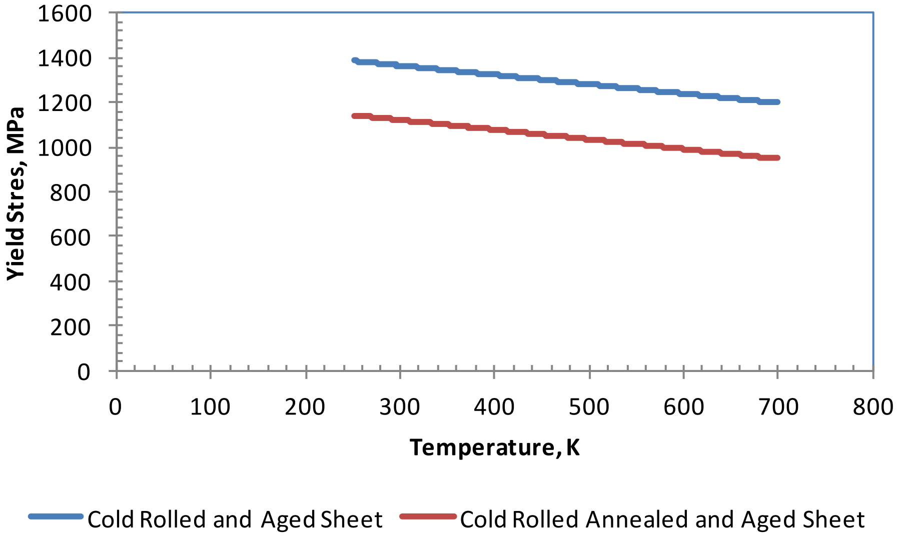

Figure 5.6. Yield Stress for Inconel 718 Sheet That Has Been Cold Rolled and Cold Rolled and Annealed

5.2.3 Ultimate Tensile Strength

The ultimate tensile strength of Inconel 718 Grids is a strong function of the final heat treatment. Cold-rolled sheet that was annealed has a lower yield stress than a sheet that was not annealed following cold rolling.

The ultimate tensile strength can be modeled for Inconel 718 sheet with and without final anneal using the equations below as a function of temperature.

$$UTS_{CR} = 1677.7 - 0.5633\,T$$

$$UTS_{CR-A} = 1483.4 - 0.4036\,T$$

where:

UTSCR = ultimate tensile strength of cold rolled sheet, MPa

UTSCR-A = ultimate tensile strength of cold rolled and annealed sheet, MPa

T = temperature, K

These correlations are shown below in Figure 5.7**Error! Reference source not found.**.

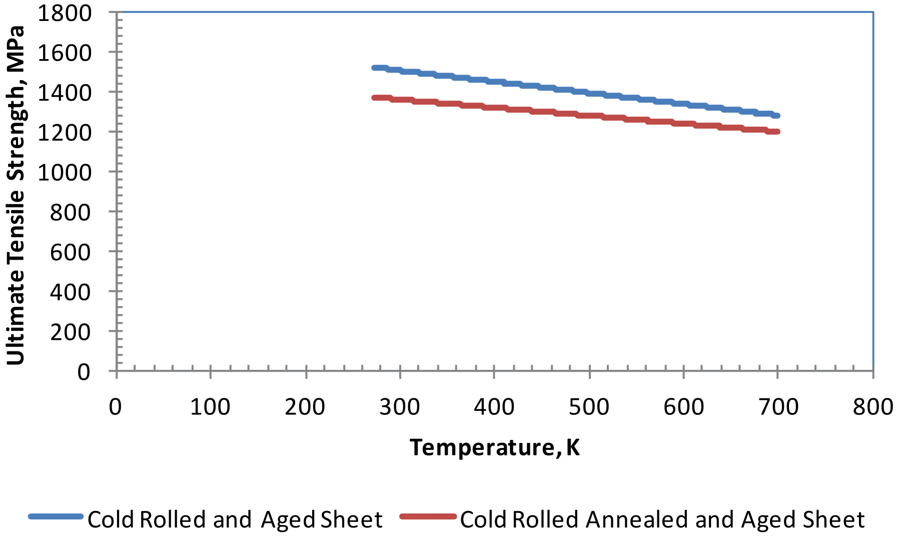

Figure 5.7. Ultimate Tensile Strength for Inconel 718 Sheet That Has Been Cold Rolled and Cold Rolled and Annealed

5.2.4 Total Elongation

The total elongation (TE) of Inconel 718 over a temperature range of 295 K to 700 K is impacted by the final heat treatment. Cold-rolled sheet that was annealed has higher elongation than a sheet that was not annealed following cold rolling. Between 295 K and 700 K, the total elongation for the annealed sheet varies between 20% and 23%. The total elongation for the sheet that was not annealed varies between 10.5% and 14%. For modeling purposes, a lower bound elongation of 10% for the cold worked sheet and 20% for the cold worked and annealed sheet should be assumed. This is stated in the equation below.

$$TE_{CR} = 10\,\%$$

$$TE_{CR-A} = 20\,\%$$

where:

TECR = total plastic elongation of cold rolled sheet, %

TECR-A = total plastic elongation of cold rolled and annealed sheet, %

Figure 5.8 shows these data and the recommended values for total elongation.

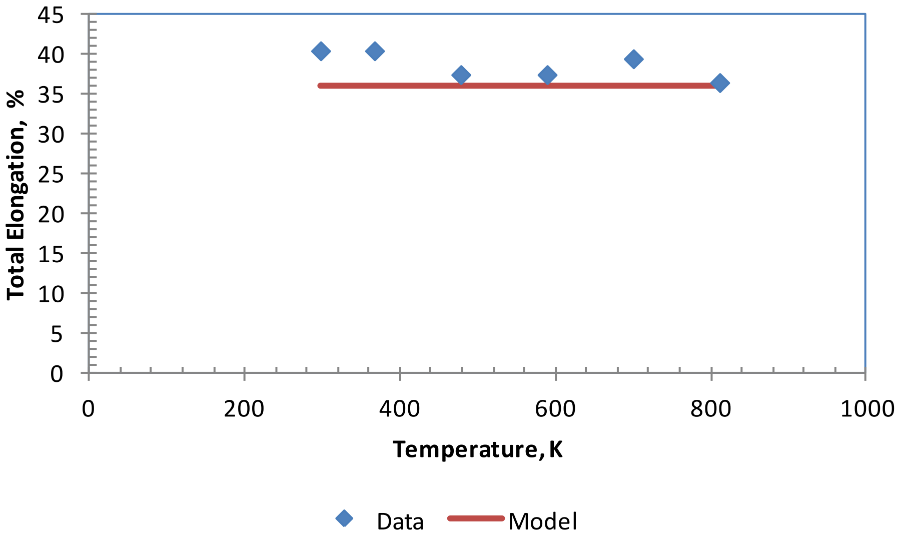

Figure 5.8. Total Elongation for Inconel 718

5.2.5 Density

The density of Inconel 718 at room temperature is 8.23 g/cm^3. There will be some thermal expansion that occurs at elevated temperature, but if this density is to be used to calculate the mass of various components and the room temperature dimensions are used to calculate that mass, this value will provide an accurate estimate of the component mass.

6. STORAGE AND TRANSPORT COMPONENT MATERIAL PROPERTIES

This section describes the storage and transport component material properties for the baseline package, elastic modulus, yield stress, ultimate tensile stress, total elongation, and density.

6.1 Baseline Package

The baseline package that will be used for this analysis is a generic burnup cask (GBC)-32 that is described in NUREG/CR-6747 (Wagner 2001). This section will provide details for the baseline transportation package that will be used in this analysis. A cutaway view of this canister is provided below in Figure 6.1. The basket, basket support structures, and the MPC shell material for the GBV are assumed to be stainless steel; either 304 or 316, or SA-240 Type XM-19 stainless steel. SA-240 Type-19 stainless steel is also known as AISI S20910 and NITRONIC 50. One or two faces of the basket cell openings are lined with neutron poison plates, which can be Boral™ sheathed in aluminum alloy (Type 1100), or metal matrix composites, which are aluminum/boron sheets.

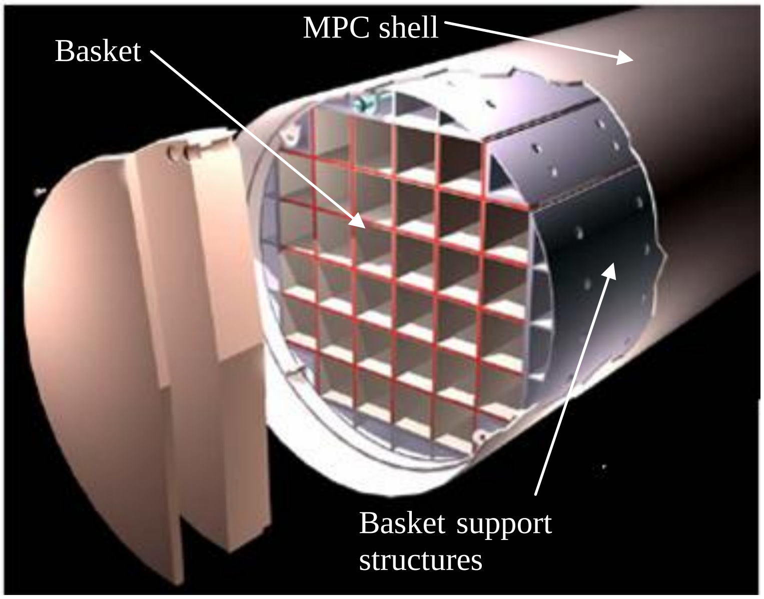

Figure 6.1. Baseline Package for Analysis is the GBC

This section will describe the mechanical properties (elastic modulus, yield strength, ultimate tensile strength, and total elongation for 304, 316, and XM-19 stainless steel as a function of temperature. HPAlloys NITRONIC 50 Stainless Steel can be supplied annealed at 1950°F to 2050°F. For most applications, the 1950°F condition is selected, as it provides a higher level of mechanical properties along with excellent corrosion resistance. The properties described in this section will be for the 1950°F annealing condition for XM-19 and in the annealed condition for 304 and 316 stainless steel.

The aluminum and the Boral will not be structural members, but mechanical properties are provided for the aluminum and the density is provided for the Boral.

6.2 Elastic Modulus

This section describes the elastic modulus for 304 and 316 stainless, XM-19, Boral and aluminum 1100.

6.2.1 304 Stainless Steel

The elastic modulus of 304 stainless steel over a temperature range of 295 K to 673 K can be approximated with the linear correlation given below.

$$E = 224.11 - 0.089\,T$$

where:

E = elastic modulus, GPa

T = temperature, K

The Poisson’s ration of 304 stainless steel over temperature range of 295 K to 673 K can be approximated with the linear correlation given below.

$$\nu = 0.2663 + 7.992 \times 10^{-5}\,T$$

where:

ν = Poisson’s Ratio, unitless

T = temperature, K

The elastic modulus (E) and the shear modulus (G) are related to each other by Poisson’s ratio (ν) according to the equation below.

$$E = 2G(1+\nu)$$

The correlations reported above are based on data that was reported in Lee et al. 1998 and Letbetter 1981. Figure 6.2 and Figure 6.3 show the data used and the correlations for elastic modulus and Poisson’s ratio, respectively. No indication of the expected variation between lots is given. It can be seen from these figures that there is little variation between the data and the models.

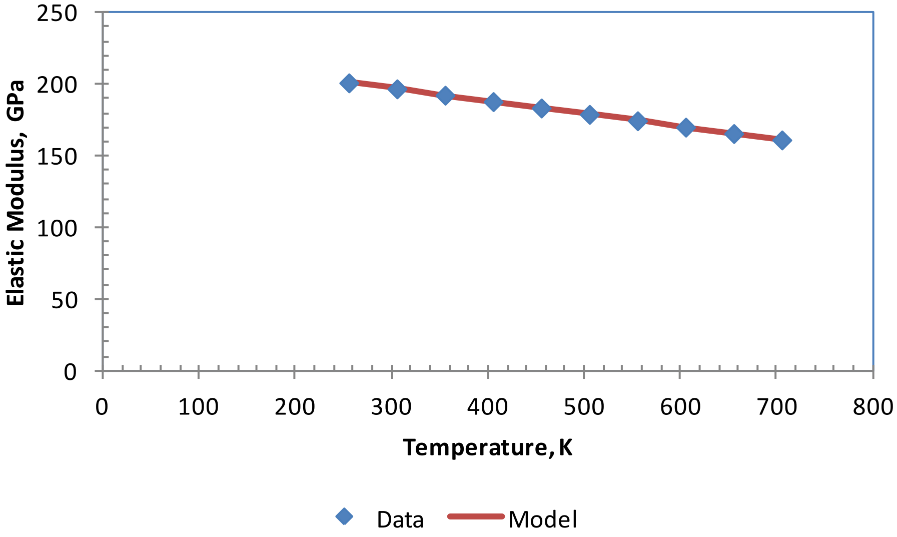

Figure 6.2. Elastic Modulus for 304 Stainless Steel

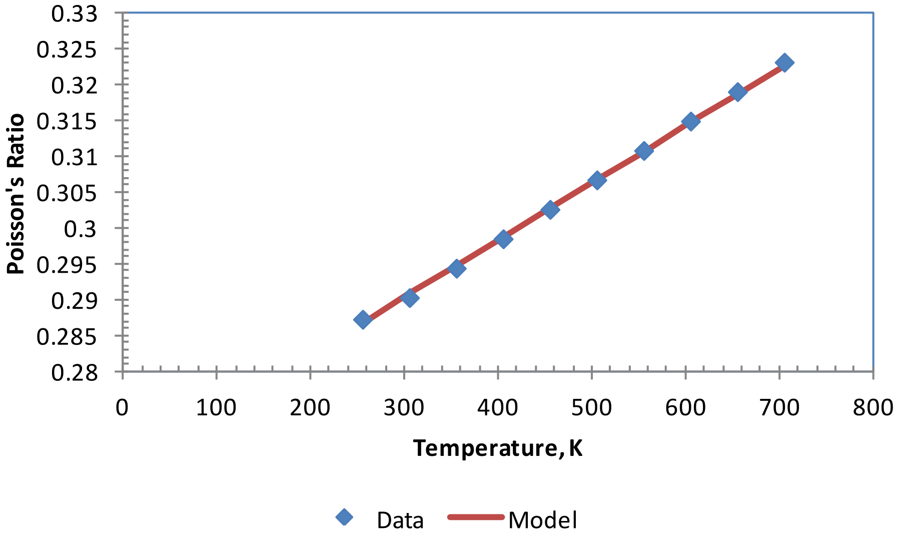

Figure 6.3. Poisson's Ratio for 304 Stainless Steel

6.2.2 316 Stainless Steel

The elastic modulus of 316 stainless steel over a temperature range of 295 K to 673 K can be approximated with the linear correlation given below.

$$E = 218.28 - 0.0836\ T$$

where:

E = elastic modulus, GPa

T = temperature, K

The Poisson's ration of 316 stainless steel over a temperature range of 295 K to 673 K can be approximated with the linear correlation given below.

$$\nu = 0.2712 + 7.864 \times 10^{-5}\ T$$

Where:

ν = Poisson's Ratio, unitless

T = temperature, K

The elastic modulus (E) and the shear modulus (G) are related to each other by Poisson's ratio (ν) according to the equation below.

$$E = 2G(1 + \nu)$$

The correlations reported above are based on data that was reported in Lee et al. (1998) and Letbetter (1981). No indication of the expected variation between lots is given. Figure 6.4 and Figure 6.5 show these data and the correlations for elastic modulus and Poisson's ratio, respectively. It can be seen from these figures that there is little variation between the data and the models.

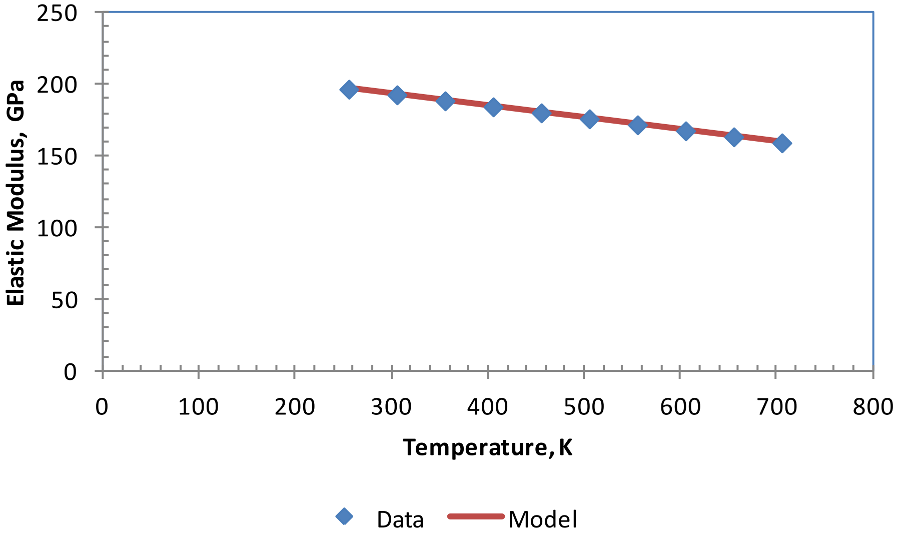

Figure 6.4. Elastic Modulus for 316 Stainless Steel

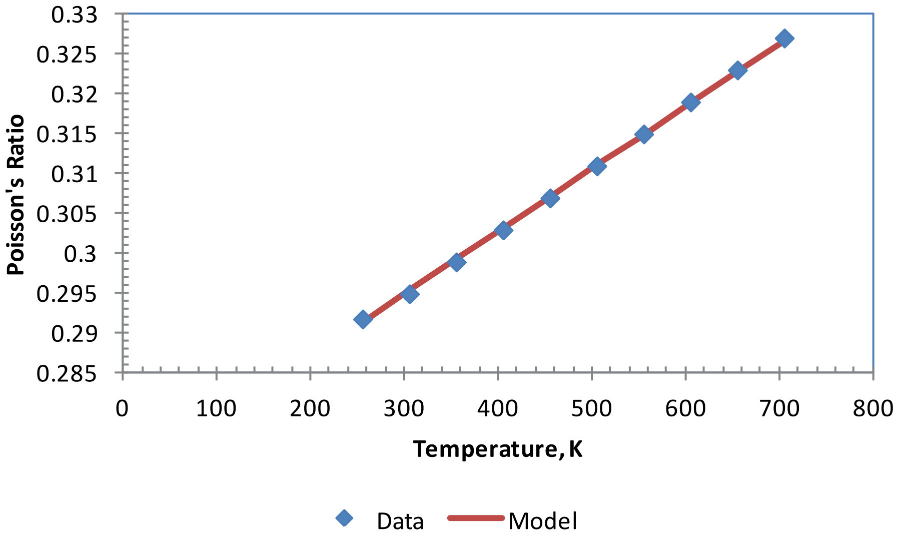

Figure 6.5. Poisson's Ratio for 316 Stainless Steel

6.2.3 XM-19

The elastic modulus of XM-19 over a temperature range of 295 K to 650 K can be approximated with the linear correlation given below.

$$E = 227.77 - 0.0987\,T$$

where:

E = elastic modulus, GPa

T = temperature, K

The Poisson's ratio of XM-19 over a temperature range of 295 K to 650 K can be approximated with the linear correlation given below.

$$\nu = 0.3325 - 7.0 \times 10^{-5}\,T$$

where:

ν = Poisson's Ratio, unitless

T = temperature, K

The elastic modulus (E) and the shear modulus (G) are related to each other by Poisson's ratio (ν) according to the equation below.

$$E = 2G(1+\nu)$$

The correlations reported above are based on data that was reported in the *Nitronic-50 Product Data Bulletin* (Nitronic 2013). The tests were performed on sheet samples in the longitudinal direction using strain gages. No indication of the expected variation between lots is given. Figure 6.6 and Figure 6.7 show these data and the correlations for elastic modulus and Poisson's ratio, respectively. It can be seen from these figures that there is little variation between the data and the models.

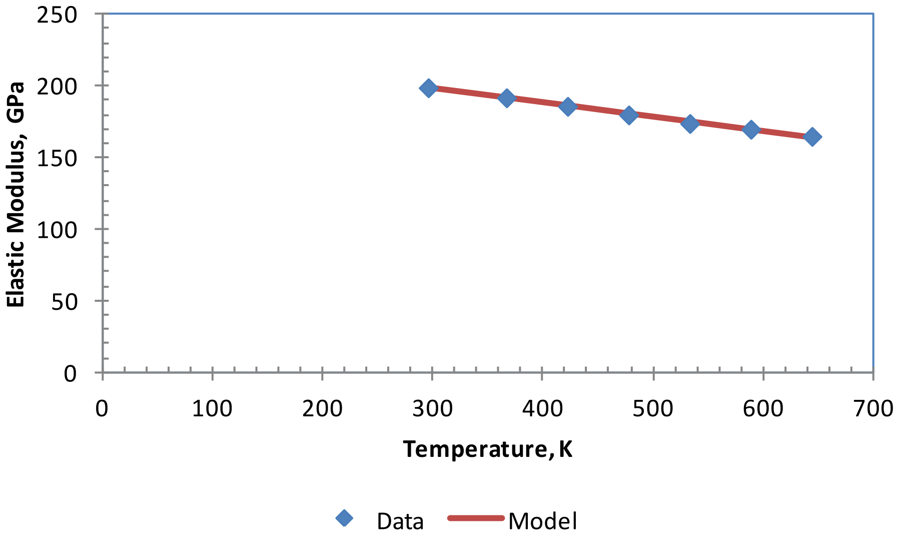

Figure 6.6. Elastic Modulus for XM-19 Stainless Steel

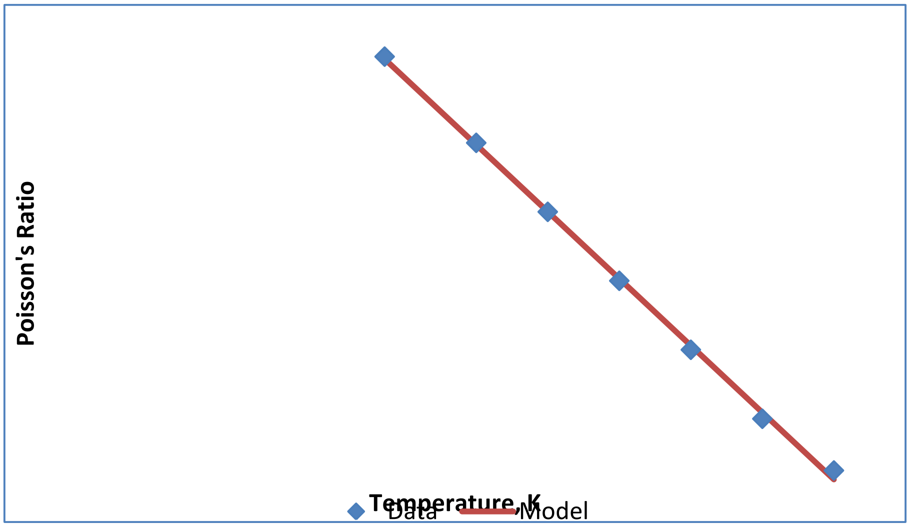

Figure 6.7. Poisson's Ratio for XM-19 Stainless Steel

6.2.4 Boral™ and Aluminum 1100

The elastic modulus of aluminum over a temperature range of 295 K to 775 K can be approximated with the third order polynomial correlation given below.

$$E = -3.306 \times 10^{-7} T^3 + 3.973 \times 10^{-4} T^2 - 1.937 \times 10^{-1} T + 101.4$$

where:

E = elastic modulus, GPa

T = temperature, K

The correlation reported above are based on data that reported in the *Boral Composite Standard Specifications* (Ceradyne 2013). No indication of the expected variation between heats is given. Figure 6.8 shows these data and the correlation for elastic modulus. The elastic modulus of Boral is reported as 62 GPa, which corresponds with the room temperature modulus of Aluminum 1100.

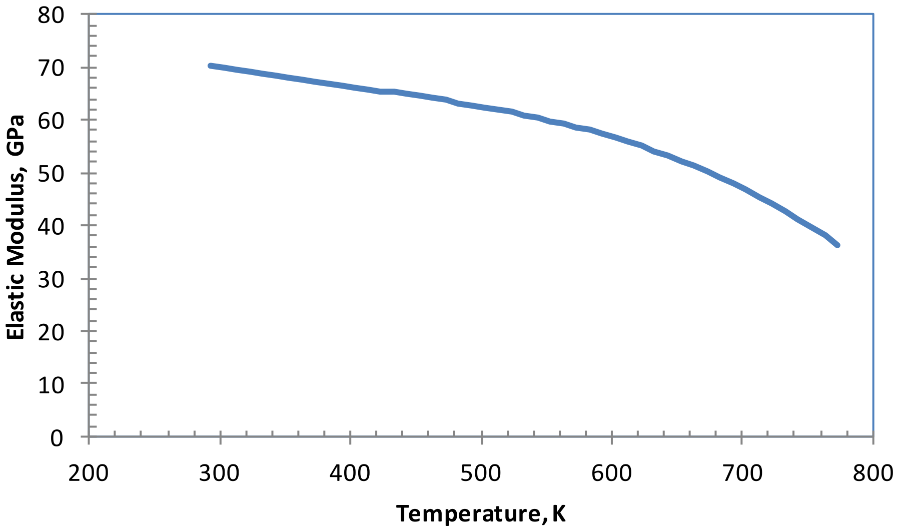

Figure 6.8. Elastic Modulus for Aluminum 1100

6.3 Yield Stress

This section describes the yield stress for 304 and 316 stainless, XM-19, Boral and aluminum 1100.

6.3.1 304 Stainless

The yield stress of 304 stainless steel over a temperature range of 295 K to 673 K can be approximated with the second order polynomial correlation given below.

$$YS = 7.775 \times 10^{-4} T^2 - 1.120\, T + 526.0$$

where:

YS = yield stress, MPa

T = temperature, K

The correlation reported above is based on data reported in ATI Allegheny Ludlum 2013. No indication of the expected variation between heats is given. Figure 6.9 shows these data and the correlation for yield stress. It can be seen from these figures that there is little variation between the data and the model.

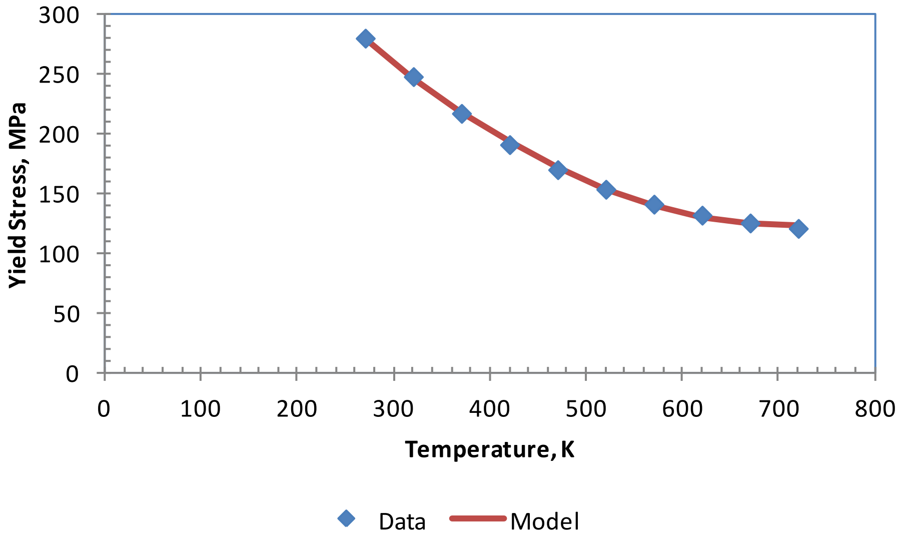

Figure 6.9. Yield Stress for 304 Stainless Steel

6.3.2 316 Stainless

The yield stress of 316 stainless steel over a temperature range of 295 K to 673 K can be approximated with the second order polynomial correlation given below.

$$YS = 1.239 \times 10^{-4} T^2 - 0.4053\ T + 407.0$$

where:

YS = yield stress, MPa

T = temperature, K

The correlation reported above is based on data that was reported in ATI Allegheny Ludlum (2012) and Cartech (2003). No indication of the expected variation between heats is given. Figure 6.10 shows these data and the correlation for yield stress. It can be seen from these figures that there is little variation between the data and the model.

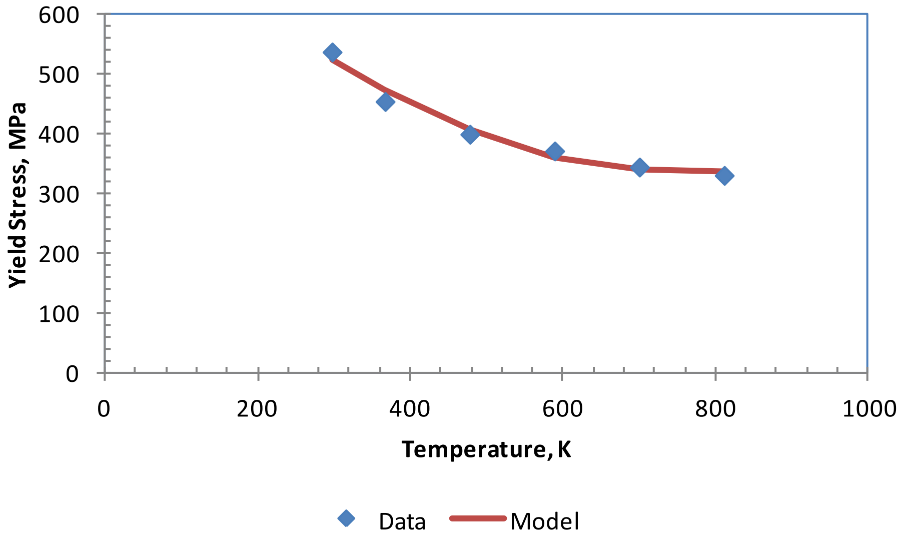

Figure 6.10. Yield Stress for 316 Stainless Steel

6.3.3 XM-19

The yield stress of XM-19 over a temperature range of 295 K to 810 K can be approximated with the second order polynomial correlation given below.

$$YS = 8.6464 \times 10^{-4} T^{2} - 1.323 T + 841.0$$

where:

YS = yield stress, MPa

T = temperature, K

The correlation reported above are based on data that was reported in the *Nitronic-50 Product Data Bulletin* (Nitronic 2013). Tensile tests were performed on bars and the data shown is the average of tests performed on three heats. No indication of the expected variation between heats is given. Figure 6.11 shows these data and the correlation for yield stress. It can be seen from these figures that there is little variation between the data and the model.

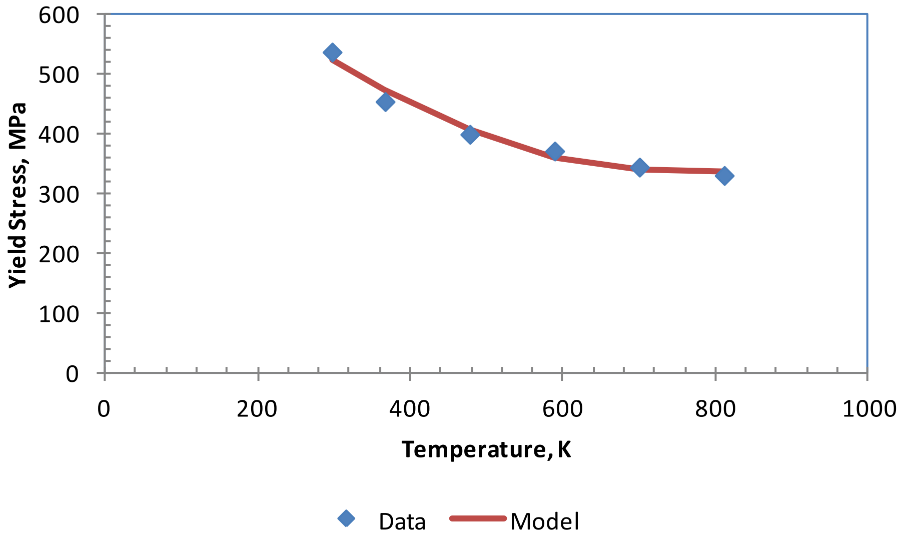

Figure 6.11. Yield Stress for XM-19 Stainless Steel

6.3.4 Boral™ and Aluminum 1100

The yield stress of aluminum over a temperature range of 295 K to 550 K can be approximated with the third order polynomial correlation given below.

$$YS = 1.705 \times 10^{-6} T^{3} - 2.222 \times 10^{-3} T^{2} + 8.984 \times 10^{-1} T + 87.71$$

where:

YS = yield stress, MPa

T = temperature, K

The correlation reported above are based on data that reported in the *Boral Composite Standard Specifications* (Ceradyne 2013). No indication of the expected variation between heats is given. Figure 6.12 shows these data and the correlation for yield stress.

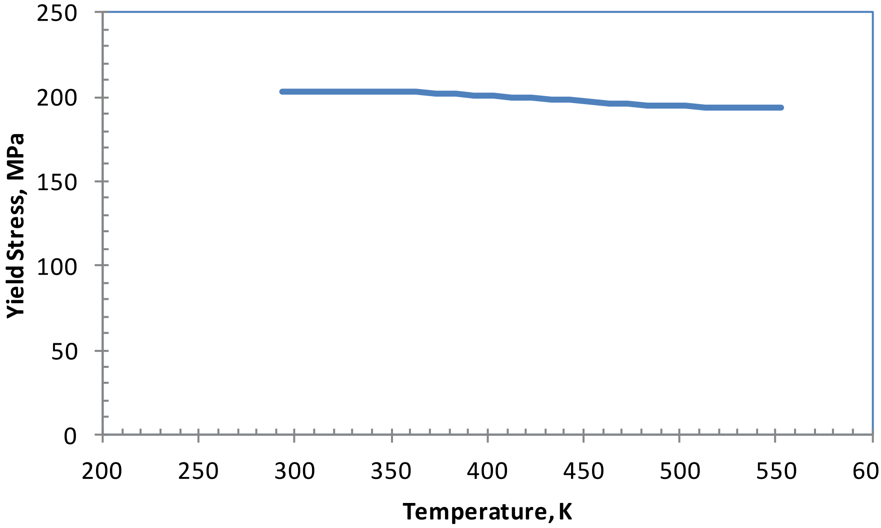

Figure 6.12. Yield Stress for Aluminum 1100

6.4 Ultimate Tensile Stress

This section describes the ultimate tensile stress for 304 and 316 stainless, XM-19, Boral and aluminum 1100.

6.4.1 304 Stainless Steel

The ultimate tensile strength of 304 stainless steel over a temperature range of 295 K to 673 K can be approximated with the second order polynomial correlation given below.

$$UTS = 2.493 \times 10^{-3} T^2 - 3.098 T + 1406$$

where:

UTS = ultimate tensile strength, MPa

T = temperature, K

The correlation reported above is based on data that reported in ATI Allegheny Ludlum 2013. No indication of the expected variation between heats is given. Figure 6.13 shows these data and the correlation for ultimate tensile strength. It can be seen from these figures that there is little variation between the data and the model.

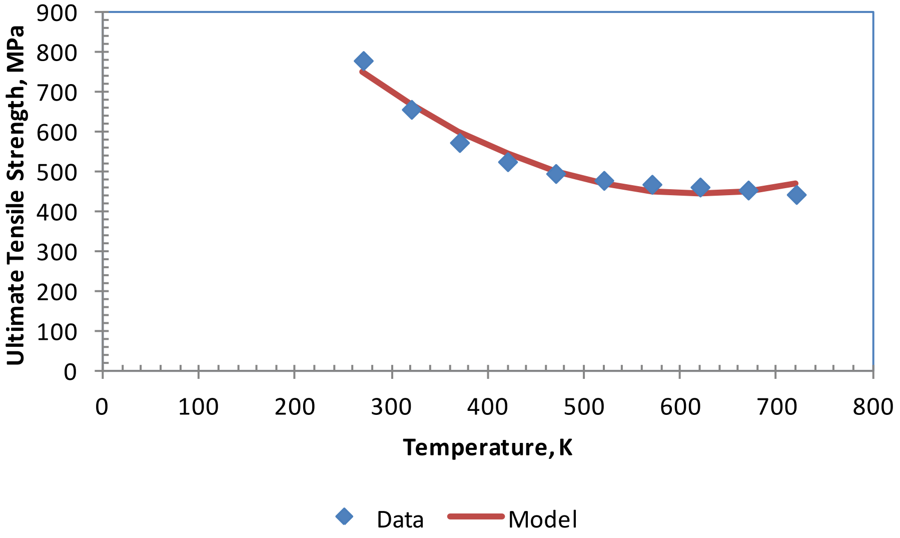

Figure 6.13. Ultimate Tensile Strength for 304 Stainless Steel

6.4.2 316 Stainless Steel

The ultimate tensile strength of 316 stainless steel over a temperature range of 295 K to 673 K can be approximated with the second order polynomial correlation given below.

$$UTS = 1.287 \times 10^{-3} T^2 - 1.482\ T + 905.6$$

where:

UTS = ultimate tensile strength, MPa

T = temperature, K

The correlation reported above are based on data that was reported in ATI Allegheny Ludlum (2012) and Cartech (2003). No indication of the expected variation between heats is given. Figure 6.14 shows these data and the correlation for ultimate tensile strength. It can be seen from these figures that there is little variation between the data and the model.

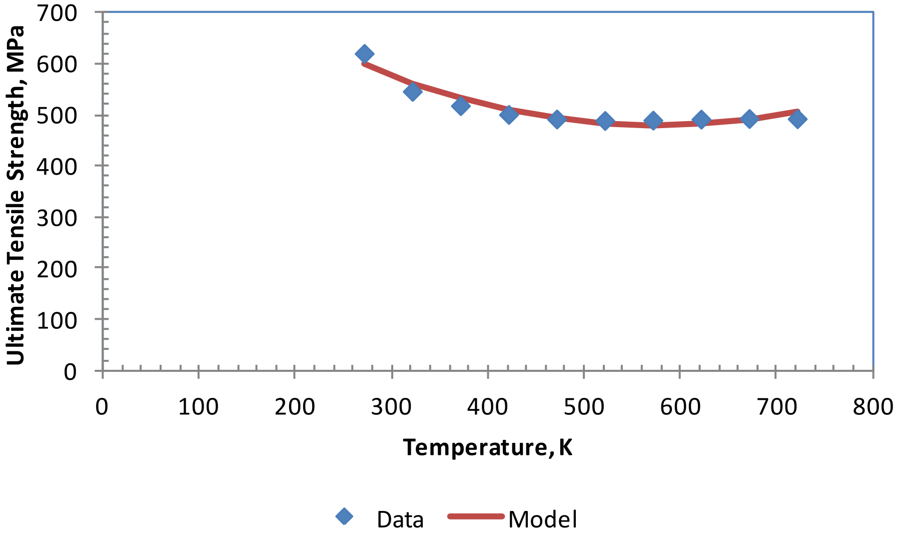

Figure 6.14. Ultimate Tensile Strength for 316 Stainless Steel

6.4.3 XM-19

The ultimate tensile strength of XM-19 over a temperature range of 295 K to 810 K can be approximated with the second order polynomial correlation given below.

$$UTS = 7.996 \times 10^{-4} T^2 - 1.309 T + 1159$$

where:

UTS = ultimate tensile strength, MPa

T = temperature, K

The correlation reported above are based on data that was reported in the *Nitronic-50 Product Data Bulletin* (Nitronic 2013). Tensile tests were performed on bars and the data shown is the average of tests performed on three heats. No indication of the expected variation between heats is given. Figure 6.15 shows these data and the correlation for ultimate tensile strength. It can be seen from these figures that there is little variation between the data and the model.

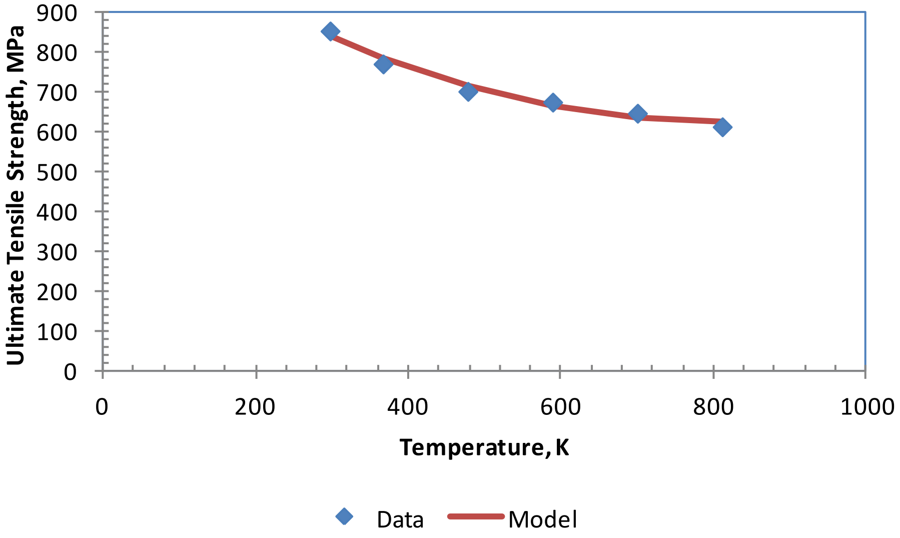

Figure 6.15. Ultimate Tensile Strength for XM-19 Stainless Steel

6.4.4 Boral™ and Aluminum 1100

The ultimate tensile strength of aluminum over a temperature range of 295 K to 550 K can be approximated with the third order polynomial correlation given below.

$$UTS = 3.378 \times 10^{-6} T^3 - 4.412 \times 10^{-3} T^2 + 1.636 T + 109.5$$

where:

UTS = ultimate tensile strength, MPa

T = temperature, K

The correlation reported above is based on data that reported in the *Boral Composite Standard Specifications* (Ceradyne 2013). No indication of the expected variation between heats is given. Figure 6.16 shows these data and the correlation for yield stress.

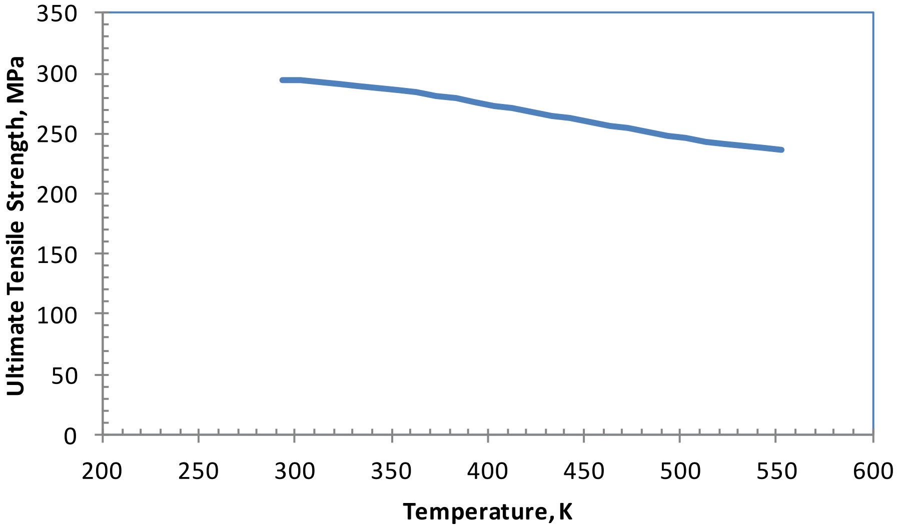

Figure 6.16. Ultimate Tensile Strength for Aluminum 1100

6.5 Total Elongation

This section describes the total elongation for 304 and 316 stainless, XM-19, Boral and aluminum 1100.

6.5.1 304 Stainless Steel

The total elongation of 304 stainless steel over a temperature range of 295 K to 673 K varies between 45% and 60%. It does not appear to be strongly correlated with temperature. For modeling purposes, a lower bound elongation of 45% should be assumed. This is stated in the equation below.

$$TE = 45\,\%$$

where:

TE = total plastic elongation, %

The correlation reported above is based on data that was reported in ATI Allegheny Ludlum 2013. No indication of the expected variation between heats is given. Figure 6.17 shows these data and the recommended value for total elongation.

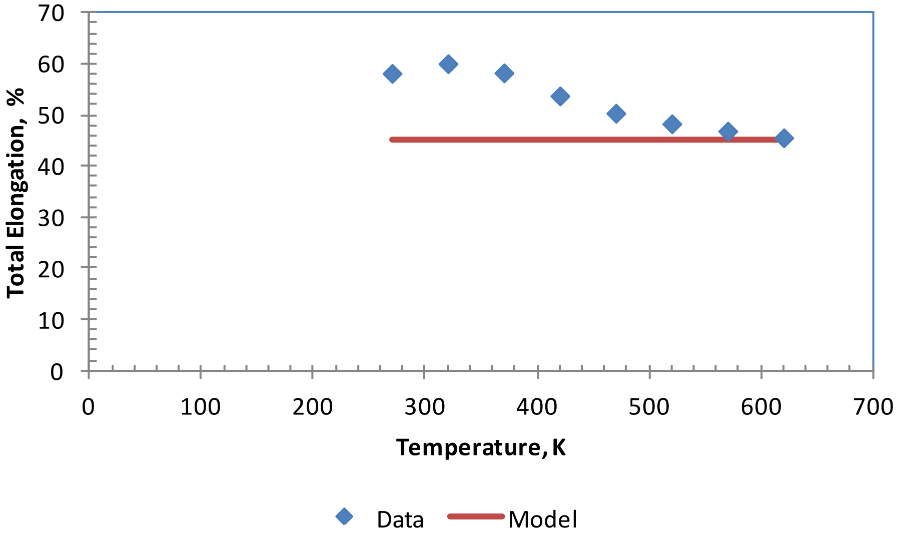

Figure 6.17. Total Elongation for 304 Stainless Steel

6.5.2 316 Stainless Steel

The total elongation of 316 stainless steel over a temperature range of 295 K to 673 K varies between 45% and 56%. It does not appear to be strongly correlated with temperature. For modeling purposes, a lower bound elongation of 45% should be assumed. This is stated in the equation below.

$$TE = 45\,\%$$

where:

TE = total plastic elongation, %

The correlation reported above is based on data that was reported in ATI Allegheny Ludlum (2012) and Cartech (2003). No indication of the expected variation between heats is given. Figure 6.18 shows these data and the recommended value for total elongation.

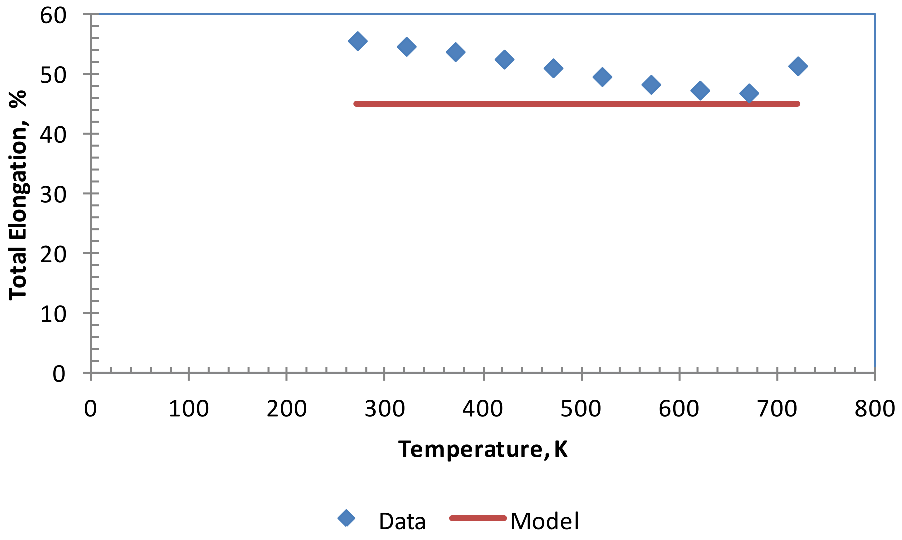

Figure 6.18. Total Elongation for 316 Stainless Steel

6.5.3 XM-19

The total elongation of XM-19 over a temperature range of 295 K to 810 K varies between 36.5% and 40.5%. It does not appear to be correlated with temperature. For modeling purposes, a lower bound elongation of 36% should be assumed. This is stated in the equation below.

$$TE = 36\,\%$$

where:

TE = total plastic elongation, %

The correlation reported above is based on data that was reported in the *Nitronic-50 Product Data Bulletin* (Nitronic 2013). Tensile tests were performed on bars and the data shown is the average of tests performed on three heats. No indication of the expected variation between heats is given. Figure 6.19 shows these data and the recommended value for total elongation.

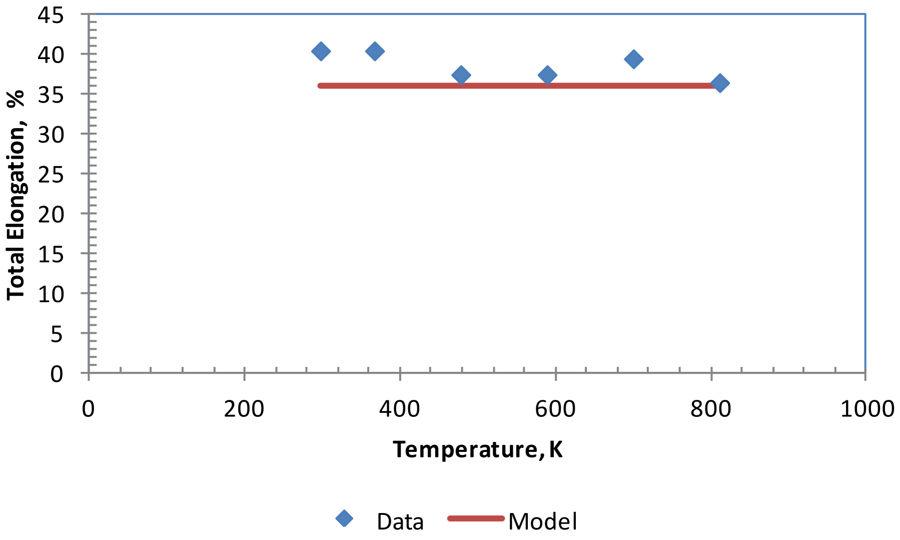

Figure 6.19. Total Elongation for XM-19 Stainless Steel

6.6 Density

This section describes the total density for 304 and 316 stainless, XM-19, Boral and aluminum 1100.

6.6.1 304 Stainless Steel

The density of 304 stainless steel at room temperature is 7.86 g/cm³ as reported in ATI Allegheny Ludlum 2013. There will be some thermal expansion that occurs at elevated temperature, but if this density is to be used to calculate the mass of various components and the room temperature dimensions are used to calculate that mass, this value will provide an accurate estimate of the component mass.

6.6.2 316 Stainless Steel

The density of 316 Stainless Steel at room temperature is 7.97 g/cm³ as reported in ATI Allegheny Ludlum (2012) and Cartech (2003). There will be some thermal expansion that occurs at elevated temperature, but if this density is to be used to calculate the mass of various components and the room temperature dimensions are used to calculate that mass, this value will provide an accurate estimate of the component mass.

6.6.3 XM-19

The density of XM-19 at room temperature is 7.88 g/cm³ as reported in the *Nitronic-50 Product Data Bulletin* (Nitronic 2013). There will be some thermal expansion that occurs at elevated temperature, but if this density is to be used to calculate the mass of various components and the room temperature dimensions are used to calculate that mass, this value will provide an accurate estimate of the component mass.

6.6.4 Boral™ and Aluminum 1100

The density of aluminum 1100 at room temperature is 2.713 g/cm³ as reported in the *Boral Composite Standard Specifications* (Ceradyne 2013). The density of Boral™ at room temperature is 2.481 g/cm³. There will be some thermal expansion that occurs at elevated temperature, but if this density is to be used to calculate the mass of various components and the room temperature dimensions are used to calculate that mass, this value will provide an accurate estimate of the component mass.

7. SURROGATE ASSEMBLY MATERIAL PROPERTIES

Plans are underway to assemble a surrogate fuel assembly, replacing the Zircaloy-4 cladding tubes with copper tubing (Alloy 12200) and replacing the UO_2 fuel with lead bar stock as shown in Figure 7.1. This surrogate assembly will be instrumented with accelerometers and tested on a shaker table to simulate NCT. Modeling will be performed to provide some validation of the modeling approach by comparing the results to the data from the instrumented surrogate assembly. To assist in this modeling activity, properties for all these materials are given at room temperature. Table 7.1 shows the surrogate assembly properties that are provided at room temperature in this section. Material properties for lead and copper are taken from www.matweb.com and from the *Application Data Sheet: Mechanical Properties of Copper and Copper Alloys at Low Temperatures,* (CDA 2013).

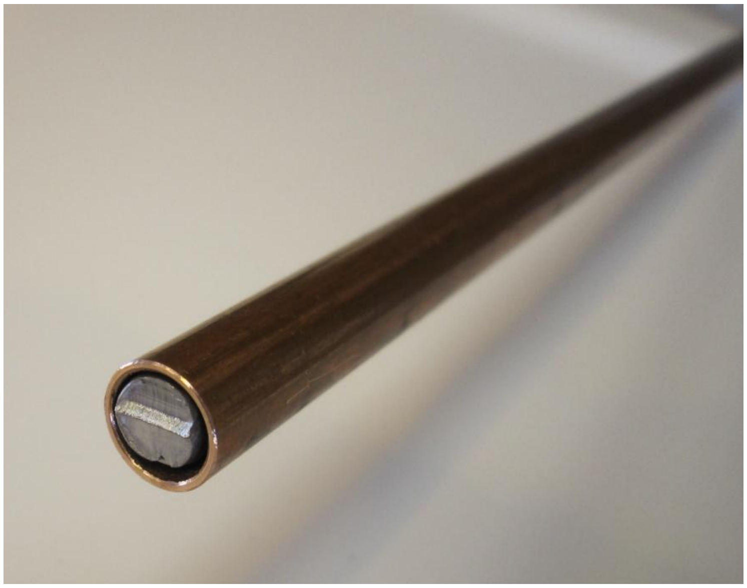

Figure 7.1. Lead Rod within Copper Tube for Surrogate Assembly

Table 7.1. Room Temperature Material Properties for Alloy 12200 Copper Tubing and Lead Bar Stock used for the Surrogate Fuel Assembly

Property	**Alloy 12200 Copper**	**Lead**
Elastic Modulus	130 GPa	14 GPa
Shear Modulus	-	4.9 GPa
Yield Stress	341 MPa	6 MPa

Ultimate Tensile Strength	357 MPa	18 MPa
Total Elongation	45%	45%
Density	8.94 g/cm^3	11.35 g/cm^3

8. CONCLUSIONS

This material properties document was assembled to support the RD&D Plan identified in Adkins (2013) and describes the relevant material properties necessary to model and simulate the transportation of a generic transport package containing 32 PWR 17x17 fuel assemblies under NCT. The largest uncertainty exists on the material properties for the irradiated components, particularly the fuel and the cladding.

Best estimate models for the fuel and the cladding have been provided. These estimates have been successfully used as part of the PNNL/NRC fuel performance codes. This effort has concentrated on using existing models rather than creating new models due to the limited funding and schedule. Areas of particular uncertainty have been identified and these areas will be targeted for sensitivity studies in order to determine if these large uncertainties have significant impact on the response of the GBC under NCT. If any area is found to have significant impact, it will identify a need for further testing. However, in the meantime, these properties are expected to give reasonable value to the modelers for their initial modeling activities.

9. REFERENCES

ASTM E399 – 74. 1974. "Standard Test Method for Plane-Strain Fracture Toughness of Metallic Materials." ASTM International, West Conshohocken, Pennsylvania.

ASTM E813 – 89. 1989. "Standard Test Method for JIC, A Measure of Fracture Toughness." ASTM International, West Conshohocken, Pennsylvania.

Adkins HE. 2013. *Used Nuclear Fuel Loading and Structural Performance Under Normal Conditions of Transport - Draft Modeling, Simulation and Experimental Integration RD&D Plan*, FCRD-UFD-2013-000111, Pacific Northwest National Laboratory, Richland, Washington.

Aluminum Alloys for Cryogenic Applications. 1999. The Aluminum Association, Washington, DC. Available from IHS at http://global.ihs.com/doc_detail.cfm?currency_code=USD&customer_id=2125402B570A&oshid=2125402B5F0A&shopping_cart_id=2125402B5A0A&mid=W097&input_doc_number=AA%20CRYO&country_code=US&lang_code=ENGL&item_s_key=00459681&item_key_date=001231&input_doc_number=AA%20CRYO&input_doc_title. Accessed on March 15, 2013.

ATI Allegheny Ludlum. 2013. Technical Data Blue Sheet: *Stainless Steels Chromium-Nickel Types 302 (S30200), 304 (S30400), 304L (S30403), 305 (S30500)*. Allegheny Technologies Incorporated, Pittsburgh, PA. Accessed March 14, 2013 at http://ncsx.pppl.gov/NCSX_Engineering/Materials/StainlessSteel/302_305data.pdf.

ATI Allegheny Ludlum. 2012. Technical Data Sheet: ATI 316Ti^{TM} Stainless Steel: Austenitic (UNS S31635). Allegheny Technologies Incorporated, Pittsburgh, PA. Accessed March 14, 2013 at http://www.atimetals.com/Documents/ati_316ti_tds_en.pdf.

Adamson R and B Cox. 2005. "Zirat-10 Special Topics Report, Impact of Irradiation on Material Performance." Advanced Nuclear Technology International, Surahammar, Sweden. Accessed March 14, 2013 at http://www.antinternational.com/fileadmin/Products_and_handbooks/Zirat/Zirat10_Str_Impact_Of_Irradiation_Sample.pdf

Adamson RB, SB Wisner, RP Tucker, and RA Rand. 1986. "Failure Strain for Irradiated Zircaloy Based on Subsized Specimen Testing and Analysis," *The Use of Small Scale Specimens for Testing Irradiated Material*, ASTM STP 888, p. 171-185, WR Corwin and GE Lucas, Eds., American Society for Testing and Materials, Philadelphia, Pennsylvania.

Aomi M, T Baba, T Miyashito, K Kaminura, T Yasuda, Y Shinohara, and T Takeda. 2008. "Evaluation of Hydride Reorientation Behavior and Mechanical Properties for High-Burnup

Fuel-Cladding Tubes in Interim Dry Storage." *Journal of ASTM International* DOI: 10.1520/JAI101262.

Armstrong PE and HL Brown. 1964. "Dynamic Young's modulus measurement above 1000°C on some pure polycrystalline metals and commercial graphites." *Transactions of the Metallurgical Society of AIME 230*, 962-966.

Attchison I. 1969. "The effect of Orientation of Hydride Precipitates on the fracture toughness of cold-rolled Zircaloy-2 and 2.5Nb Zirconium Alloy," Applications-Related Phenomena for Zirconium and its alloys, ASTM STP 458, American Society for Testing Materials, pp. 160-178.

Averty X, M Genisson, and JP Pizzanelli. 2003. "PROMETRA-Tensile Tests on Ring Specimens Machined in Zirlo Cladding Irradiated 5 Cycles up to 75 GWd/tU," *Institut De Radioprotection Et De Surete Nucleaire*, DMN/SEMI/LCMI/NT/2003-025/A, September.

Balfour MG. 1982. "High Burnup Fuel Rod Hot Cell Program, Vol. 1: Final Report," DOE/ET 34073-1, WCAP-10238, U.S. Department of Energy and Westinghouse Electric Corporation.

Balfour MG. 1982. "Zorita Research and Development Program Volume 1, Final Report," WCAP-10180, Westinghouse Electric Corporation, Cranberry Township, Pennsylvania.

Berat-Robert L, J Pelcha R Limon, R Maury, J Pele, C Cappelaere, C Prioul, P Bouffioux, J Diz. 2000. "Influence of a Zirconia Layer on the Mechanical Behavior of Zircaloy-4 Cladding and Thimble Tubes," *LWR Fuel Performance Meeting*, Vol. 2, p. 931, Park City, Utah, USA.

Berghe S V, A Leenaers, B Vos, L Sannen, M Verwerft. 2004. "Observation of a Pellet-Cladding Bonding Layer in High Burnup Fuel," OECD International Seminar Proceedings on Pellet-Clad Interaction in Water Reactor Fuels (PCI-2004) , Aix en Provence, France, March 9 – 11, 2004.

Billone MC. 2002. "The Mechanical Properties Expert Group Update on Round Robin Test Results," Argonne National Laboratory.

Billone MC, TA Burtseva, and RE Einziger. 2013. "Ductile-to-brittle transition temperature for high-burnup cladding alloys exposed to simulated drying-storage conditions." *Journal of Nuclear Materials* 433:431-448.

Billone MC, TA Burtseva, and YY Liu. 2012. "Baseline Studies for Ring Compression Testing of High-Burnup Fuel Cladding." FCRD-USED-2013-000040, ANL-12/58, Argonne National Laboratory, Lemont, Illinois.

Bolmaro RE, and F Povolo. 1988. "Anelastic behaviour of materials under multiaxial strains." *Journal of Materials Science* 23:371.

Bourdilliau B, F Onimus, C Cappelaere, V Pivetaud, P Bouffioux, V Chabretou, and A Miquet. 2010. "Impact of the irradiation damage recovery during transportation on the subsequent temperature tensile behavior of irradiated zirconium alloys”. In *16th International Symposium on Zirconium in the Nuclear Industry*, Chengdu, Sichuan Province, China.

Brochard , F Bentejac, N Hourdequin, S Seror, C Verdeau, O Fandeur, S Lansiart, P Verpeaux. 2001. “Modeling of pellet-cladding interaction in PWR fuel.” In *Transactions of the SMIRT-16 Conference*, Washington, DC, USA.

Bunnell LR, JL Bates, and GB Mellinger. 1977. “Some High Temperature Properties of Zircaloy Oxygen Alloys,” EPRI NP-524, Pacific Northwest Laboratory, Richland, Washington.

Busby CC 1966. *Properties of Zircaloy-4 Tubing*, WAPD-TM-585, p. 65, Bettis Atomic Power Laboratory, Pittsburgh, Pennsylvania.

Cartech – Carpenter Technology Corporation. 2003. Technical Data Sheet: *Carpenter Stainless Type 316/316L*. CRS Holdings Inc., a subsidiary of Carpenter Technology Corporation, Wyomissing, PA. Accessed March 14, 2013 at http://cartech.ides.com/datasheet.aspx?I=101&TAB=DV_DS&E=257&SKEY=101.7.3228726%3A590e294c-8a7c-4ebb-b725-1a1bdd03980e&CULTURE=en-US.

CDA – Copper Development Association Inc. 2013. Application Data Sheet: Mechanical Properties of Copper and Copper Alloys at Low Temperatures. Publis#: 104/5. Accessed March 13, 2013 at http://www.copper.org/resources/properties/144_8/144_8.html.

Ceradyne. 2008. *Boral® Composite Standard Specifications*. Ceradyne Canada, ULC, Quebec, Canada. Accessed March 13, 2013 at http://www.ceradyneboron.com/uploads/specSheets/SP-BORA-001enSpecificationBoral.pdf.

Chun R, M Witte, and M Schwartz. 1987. “Dynamic Impact Effects on Spent Fuel Assemblies,” UCID - 21246, Lawrence Livermore National Laboratory, Livermore, California.

Coleman, CE, BA Cheadle, AR Causey, PCK Chow, PH Davies, MD McManus, DK Rodgers, S Sagat, and G van Drunen. 1989. “Evaluation of Zircaloy-2 Pressure Tubes from NPD,” Zirconium in the Nuclear Industry: Eighth International Symposium, ASTM STP 1023, American Society for Testing Materials, pp. 35-49.

Daum RS, S Majumdar, YY Liu, and M Billone. 2005. “Mechanical Testing of High-burnup Zircaloy-4 Fuel Cladding Under Conditions Relevant to Drying Operations and Dry-cask Storage.” In *Proceedings of the 2005 LWR Fuel Performance Meeting*, Kyoto, Japan, October 2-6.

Desquines J, B Cazalis, C Bernaudat, C Poussard, X Averty, and P Yvon. 2005. “Mechanical Properties of Zircaloy-4 PWR Fuel Cladding with Burnup 54-64MWd/kgU and Implications for RIA Behavior.” *Journal of ASTM International* 2(6).

Dideon CG and GM Bain. 1983. "Fuel Performance Under Extended-Burnup Operation B&W 15x15 Design," DOE/ET/34212-38, BAW-1716, U.S. Department of Energy and Babcock and Wilcox.

Dubey JS, SL Wadekar, RN Singh, TK Sinha, and JK Chakravartty. 1999. "Assessment of hydrogen embrittlement of Zircaloy-2 pressure tubes using unloading compliance and load normalization techniques for determining J-R curves." *Journal of Nuclear Materials* 264:20-28.

Edsinger K, JH Davies, and RB Adamson. 2000. "Degraded Fuel Cladding Fractography and Fracture Behavior," Zirconium in the Nuclear Industry: Twelfth International Symposium, ASTM STP 1354, 200, American Society for Testing Materials, pp. 316-339.

Enusa - Enusa Industrias Avanzadas. 2013. PWR. Accessed March 13, 2013 at
http://www.enusa.es/eng/actividad/pwr.html.

Fisher ES and CJ Renken. 1964. "Single – crystal elastic moduli and the CHP-BCC transformation in Ti, Zr, and Hf." *Physical Review*, 135(2A):A482-494.

Garcia-Infanta JM, R Canencia, B Peterson, D Schrire, and B Claesson. 2010. "Post Irradiation Examination of the Skeleton of a 15x15 PWR Fuel Assembly." In *Proceedings of 2010 LWR Fuel Performance/TOPFUEL/WRFPM*, Orlando Florida, September 26-29.

Garde AM. 2009. "Hydrogen Pick Up Fraction for ZIRLO™ Cladding Corrosion and Resulting Impact on the Cladding Integrity". In *Proceedings of TopFuel 2009*, September 6-10, Paris France.

Garde AM. 1986. "Hot Cell Examination of Extended Burnup Fuel From Fort Calhoun," Combustion Engineering Report CEND-427, DOE/ET/34030-11, U.S. Department of Energy and Combustion Engineering.

Garde AM. 1989. "Effects of Irradiation and Hydriding on the Mechanical Properties of Zircaloy-4 at High Fluence," *Zirconium in the Nuclear Industry: 8th International Symposium, ASTM STP 1023*, p. 548, American Society for Testing and Materials, Philadelphia, USA.

Garde AM, GP Smith, and RC Pirek. 1996. "Effects of Hydride Precipitate Localization and Neutron Fluence on the Ductility of Irradiated Zircaloy-4," *Zirconium in the Nuclear Industry: 11th International Symposium, ASTM STP 1295*, p. 407, American Society for Testing and Materials, Garmisch-Partenkirchen, Germany.

Geelhood KJ and CE Beyer. 2011. "Hydrogen Pickup Models for Zircaloy-2, Zircaloy-4, M5™, and ZIRLO." In *Proceedings from 2011 Water Reactor Fuel Performance Meeting*, Chengdu, China, September 11-14.

Geelhood KJ, WG Luscher, and CE Beyer. 2010a. *FRAPCON-3.4: A Computer Code for the Calculation of Steady-State, Thermal-Mechanical Behavior of Oxide Fuel Rods for High*

Burnup, NUREG/CR-7022, Vol. 1, PNNL-19418, Vol. 1, Pacific Northwest National Laboratory, Richland, Washington.

Geelhood KJ, WG Luscher, CE Beyer, and JM Cuta. 2010b. *FRAPTRAN 1.4: A Computer Code for the Transient Analysis of Oxide Fuel Rods*, NUREG/CR-7023, Vol. 1, PNNL-19400, Vol. 1, Pacific Northwest National Laboratory, Richland, Washington.

Hardy DH. 1970. "The Effect of Neutron Irradiation on the Mechanical Properties of Zirconium Alloy Fuel Cladding in Uniaxial and Biaxial Tests," *Irradiation Effects on Structural Alloys for Nuclear Reactor Applications, ASTM STP 484*, p. 215, American Society for Testing and Materials, Toronto, Canada.

Huang FH. 1993. "Brittle-fracture potential of irradiated Zircaloy-2 pressure tubes." *Journal of Nuclear Materials* 207:103-115.

Huang FH. 1993. "Fracture Toughness Evaluation for Zircaloy-2 Pressure Tubes with the Electric-Potential Method," Small Specimen Test Techniques Applied to Nuclear Reactor Vessel Thermal Annealing and Plant Life Extension, ASTM STP 1204, American Society for Testing Materials, pp182-198.

Huang FH and WJ Mills. 1993. "Fracture Properties of irradiated zircaloy-2 pressure tubes." *Nuclear Technology* 102:367.

Ito K, K Kamimura, and Y Tsukuda. 2004. "Evaluation of Irradiation Effect on Spent Fuel Cladding Creep Properties." In *Proceedings of the 2004 International Meeting on LWR Fuel Performance*, Orlando, Florida, paper 1117.

Kearns JJ. 1967. "Terminal Solubility and Partitioning of Hydrogen in the Alpha Phase of Zirconium, Zircaloy-2 and Zircaloy-4." *Journal of Nuclear Materials* 22:292.

Kemper RS and DL Zimmerman. 1957. "Neutron Irradiation Effects on the Tensile Properties of Zircaloy-2," HW-52323, General Electric Company.

Kesterson RL, HK Yueh, HH Shah, JP Foster, and DJ Colburn. 2006. "Cladding Optimization for Enhanced Performance Margins". InTop_Fuel 2006 International Meeting on LWR Fuel Performance "Nuclear Fuel: Addressing the Future". *Transactions* 22-26 October 2006 Salamanca, Spain. Accessed at http://www.euronuclear.org/events/topfuel/transactions/Topfuel-Technical-Session.pdf.

Kesterson R and R Sindelar. 2013. "Used Nuclear Fuel Characteristics at Post Discharge," Report # to be assigned. In press.

Kim KT. 2010. "UO2/Zry-4 chemical interaction layers for intact and leak PWR fuel rods." *Journal of Nuclear Materials* 404:128-137.

Kreyns PH, WF Bourgeois, CJ White, PL Charpentier, BF Kammensind, and DG Franklin. 1996. "Embrittlement of Reactor Core Material." Eleventh International Symposium on Zirconium in the Nuclear Industry, ASTM STP 1298, American Society for Testing Materials, pp.758-782.

Kubo T, K Sakamoto, and T Higuchi. 2010. "Fracture Strength of Zirconium Hydrides Embedded in a Zircaloy-2 Matrix And Its Effects on the Initiation of Delayed Hydride Cracking." In *Proceedings of 2010 LWR Fuel Performance/TopFuel/WRFPM* Orlando, Florida, USA, September 26-29.

Laux D, Baron D, Despaux G, Kellerbauer AI, Kinoshita M. 2012. *Determination of high burn-up nuclear fuel elastic properties with acoustic microscopy*. Journal of Nuclear Materials Volume 420, Issues 1–3, January 2012, Pages 94–100. Elsevier.

Lee SS, U-S. Min, B. Ahn, and S.H. Yoo. 1998. Journal of Materials Science, v33, p687. Springer.

Ledbetter HM. 1981. Journal of Applied Physics, v52 no. 3, March 1981. AIP Publishing, Chicago, Illinois.

Lowry LM. 1981. "Evaluating Strength and Ductility of Irradiated Zircaloy, Task 5," NUREG/CR-1729, BMI-2066 Vol. 1, Nuclear Regulatory Commission and Battelle Columbus Laboratories.

Mahmood ST, DM Farkas, RB Adamson, and Y Etoh. 2000. "Post-Irradiation Characterization of Ultra-High Fluence Zircaloy-2 Plate," *Zirconium in the Nuclear Industry: Twelfth International Symposium*, STM STP 1354, GP Sabol and GD Moan, Eds., ASTM International, West Conshohocken, Pennsylvania, pp. 139-169.

Mahmood ST, KW Edsinger, DM Farkas, RB Adamson. 1997. "Effects of SPP Dissolution on Mechanical Properties of Zircaloy-2," *LWR Fuel Performance Meeting*, p. 440, Portland, Oregon, USA.

MatWeb – Material Property Data. 2013. www.matweb.com Accessed on March 14, 2013 at http://www.matweb.com/search/DataSheet.aspx?MatGUID=ebd6d2cdfdca4fc285885cc4749c36b1&ckck=1.

MatWeb – Material Property Data. 2013. www.matweb.com. Accessed on March 14, 2013 at http://www.matweb.com/search/QuickText.aspx?SearchText=copper.

Mehan RL and FW Wiesinger. 1961. *Mechanical Properties of Zricaloy-2*, KAPL-2110, pp. 11-12, General Electric Company, Knolls Atomic Power Laboratory, Schenectady, New York.

Mehan RL. 1958. *Modulus of Elasticity of Zircaloy-2 Between Room Temperature and 1,000°F*, KAPL-M-RLM-16, General Electric Company, Knolls Atomic Power Laboratory, Schenectady, New York.

Northwood DO, IM London, and LE Bahen. 1975. "Elastic Constants of Zirconium Alloys." *Journal of Nuclear Materials* 55:299-310. Elsevier.

Nagase F. 2011. Hydride behavior in Zircaloy cladding tube during high-temperature transients." *Journal of Nuclear Materials* 415:117-122. Elsevier.

Newman LW. 1986. "The Hot Cell Examination of Oconee 1 Fuel Rods after Five Cycles of Irradiation," DOE/ET/34212-50, BAW-1874, U.S. Department of Energy and Babcock and Wilcox.

Newman LW. 1990. "Development of an Extended Burnup Mark B Design," DOE/ET/34213-16, BAW 1532-13, U.S. Department of Energy and Babcock and Wilcox.

Nitronic – High Performance Alloys, Inc. 2013. *Nitronic 50 Stainless Steel (UNS S 20910) Product Data Bulletin, HPAlloys NITRONIC 50 Stainless Steel Product Description*. Accessed March 13, 2013 at http://www.hpalloy.com/alloys/brochures/Nitronic50book.pdf.

Nokita K and K Une. 1997. "Formation of pellet-cladding bonding layer in high burnup BWR fuels." *Journal of Nuclear Science and Technology* 34(7):679-686.

NUREG/CR-6150, Vol. 4, Rev. 2, INEL-96/0422, Idaho National Engineering and Environmental Laboratory, Idaho Falls, Idaho.

NUREG-0800, 4.2 Fuel System Design. Accessed March 15, 2013 at http://pbadupws.nrc.gov/docs/ML0707/ML070740002.pdf.

O'Donnell WJ and BF Langer. 1964. "Fatigue design basis for Zircaloy Components." *Nuclear Science and Engineering* 20:1-12. American Nuclear Society, Washington, DC.

Padel A and A Groff. 1976. "Variation du Module de Young du Zirconium b en Function de la Temperature." *Journal of Nuclear Materials* 59:325-326. Elsevier.

Pettersson K, G Vesterlund, and T Andersson. 1979. "Effect of Irradiation on the Strength, Ductility, and Defect Sensitivity of Fully Recrystalized Zircaloy Tube," *Zirconium in the Nuclear Industry, 4th conference, ASTM STP 681*, p. 155 Stratford-upon-Avon, England.

Sercombe J, I Auburn, and C Nonon. 2012. "Power ramped cladding stresses and strains in 3D simulations with burnup-dependent pellet-clad friction." *Nuclear Engineering and Design* 242:164-181.

Shober FB, JA Van Echo, LL Marsh, and JR Keeler. 1957. *The Mechanical Properties of Zirconium and Zircaloy-2*, BMI-1168, Battelle Memorial Institute, Columbus, Ohio.

Siefken LJ, EW Coryell, EA Harvego, and JK Hohorst. 2001. *SCDAP/RELAP5/MOD 3.3 Code Manual MATPRO-A Library of Materials Properties for Light-Water-Reactor-Accident Analysis*, NUREG/CR-6150, Vol. 4, Rev. 2, INEL-96/0422, Idaho National Engineering and Environmental Laboratory, Idaho Falls, Idaho.

Simpson LA and CK Chow. 1987. “Effect of Metallurgical Variables and Temperature on the Fracture Toughness of Zirconium Alloy Pressure Tubes,” Zirconium in the Nuclear Industry: Seventh International Symposium, ASTM STP 939, American Society for Testing Materials, pp. 579-596.

Smally WR. 1971. *Saxton Core II Fuel Performance Evaluation Part 1: Materials,* WCAP-3385-56, Westinghouse Electric Corporation, Pittsburgh, Pennsylvania.

Smith GP. 1983. “The Evaluation and Demonstration of Methods for Improved Nuclear Fuel Utilization, End-of-Cycles 6 and 7 Fuel Examinations,” CEND-414, DOE/ET/34010-10, U.S. Department of Energy and C-E Power Systems.

Smith GP. 1994. “Hot Cell Examination of Extended Burnup Fuel from Calvert Cliffs-1,” TR-103302-V2, ABB Combustion Engineering.

Spasic Z, Pavlovic, M., Simic, G. 1968. Conference on the Use of Zirconium Alloys in Nuclear Reactors, Marlanske Lanze, Czechoslovakia, USAEC CONF-681086, pp. 277-284.

Special Metals Corporation. 2000. *Product Reference Guide*. Huntington, West Virginia.

Udagawa Y, T Sugiyama, M Suzuki, and F Nagase. 2011. “PCMI Failure Limit Assessed by Fracture Mechanics Approach Based on NSRR High-Burnup PWR Fuel Tests.” In *Proceedings of the International Atomic Energy Agency Meeting on Fuel Behavior and Modeling Under Severe Transient and Loca Conditions,* Tokai-mura, Ibaraki-ken, Japan, October 18-21.

Van Swan LF, AA Strasser, JD Cook, and JM Burger. 1997. “Behavior of Zircaloy-4 and Zirconium Liner Zircaloy-4 Cladding at High Burnup,” In *Proceedings of the 1997 LWR Fuel Performance,* March 2-6, p. 421, Portland, Oregon, USA.

Wagner JC. 2001. *Computational Benchmark for Estimation of Reactivity Margin from Fission Products and Minor Actinides in PWR Burnup Credit*. NUREG/CR-6747, ORNL/TM-2000/306, Oak Ridge National Laboratory, Oak Ridge, Tennessee.

Walker TJ and JN Kass. 1974. “Variation of Zircaloy Fracture Toughness with Irradiation.” Zirconium in Nuclear Applications, ASTM STP 551, American Society for Testing Materials, pp. 328-354.

Walker TJ. 1972. "Characterization of the fracture toughness of Zircaloy." *Nuclear Technology* 16:509.

Whitmarsh CL. 1962. *Review of Zircaloy-2 and Zircaloy-4 Properties Relevant to N.S. Savannah Reactor Design*, ORNL-3281, Oak Ridge National Laboratory, Oak Ridge, Tennessee.

Williams CD, RB Adamson, and KD Olshausen. 1974. "Effects of Boiling Water Reactor Irradiation on Tensile Properties of Zircaloy", European Conference on Irradiation Behavior of Fuel Cladding and Core Component Materials, Karlsruhe, pp. 189-102.

Wisner SB and RB Adamson. 1998. "Combined effects of radiation damage and hydrides on the *ductility of Zircaloy-2*." *Nuclear Engineering and Design* 185:33.

Yagnik SK, A Hermann, and RC Kuo. 2005. "Ductility of Zircaloy-4 fuel cladding and guide tubes at high fluences." *Journal of ASTM International* 2[5].